Plasma chemistry of fluorocarbon RF discharges used for dry etching

Document Version:

Publisher's PDF, also known as Version of Record (includes final page, issue and volume numbers)

Please check the document version of this publication:

• A submitted manuscript is the version of the article upon submission and before peer-review. There can be important differences between the submitted version and the official published version of record. People interested in the research are advised to contact the author for the final version of the publication, or visit the DOI to the publisher's website.
• The final author version and the galley proof are versions of the publication after peer review.
• The final published version features the final layout of the paper including the volume, issue and page numbers.

[Link to publication](#)

PLASMA CHEMISTRY OF FLUOROCARBON RF DISCHARGES USED FOR DRY ETCHING

MARCO HAVERLAG

PLASMA CHEMISTRY OF FLUOROCARBON RF DISCHARGES USED FOR DRY ETCHING

PROEFSCHRIFT

ter verkrijging van de graad van doctor aan de Technische
Universiteit Eindhoven, op gezag van de Rector Magnificus,
prof.dr. J.H. van Lint, voor een commissie aangewezen door het
College van Dekanen in het openbaar te verdedigen op
dinsdag 10 september 1991 te 16.00 uur

door

MARCO HAVERLAG

geboren te Utrecht

Dit proefschrift is goedgekeurd door
de promotoren
prof.dr. F.J. de Hoog
en
prof.dr. A. Kono
co—promotor
dr.ir. G.M.W. Kroesen

aan Elvira

CONTENTS

Contents

1. GENERAL INTRODUCTION

1.1 Principles of etching

Etching processes are used in situations where a surface layer must be fully or partially removed from a substrate. In a number of applications, e.g. in the semiconductor industry, etching is used to delineate a pattern in the layer[1]. To make such a pattern, part of the surface is covered by a mask prior to the etching process. This mask can be produced by e.g. a photo–lithographic technique and it protects those parts of the surface where the etching should not take place. In many cases the etching of the surface can be realized by using a chemically reactive liquid. In this process, called "wet chemical etching", the surface material reacts with species in the chemically active solution. Subsequently, the reaction products desorb from the surface and are transported into the solution. In this kind of process the removal rate of the material is independent of the direction and an isotropic etching profile is obtained (see figure 1.1a). This means that some undercutting beneath the mask, and henceforth, loss of resolution occurs. As long as the smallest lateral dimensions of the desired structure are much larger than the thickness of the film, this is not a problem. However, if patterns are required with dimensions in the order of or smaller than the film thickness, anisotropic etching should be used (see figure 1.1b). To achieve this, dry etching methods have been developed that are capable of yielding anisotropic profiles.

Dry etching is mostly performed in a gas discharge. In the discharge reactive neutral atoms or molecules are produced that can adsorb at the surface. Subsequently, the adsorbents can react with surface atoms to form volatile reaction products that desorb from the surface into the gas phase and thereby remove substrate material. If the reaction products are not volatile, a surface layer can build up that passivates[2] the surface, thereby inhibiting etching reactions. Furthermore energetic charged particles are formed in the discharge that can remove surface material by a sputtering process. If both neutrals and energetic ions are present, anisotropic etching can be achieved with high etch rates. Ions can increase the etch rate either by enhancement of the etching reaction (due to a synergistic effect[3]) or by removal of inhibiting layers[2]. Several types of discharges at various frequencies are being used to produce both neutral and charged particles, like DC plasmas[4], RF plasmas[5] (frequencies between 50 kHz – 30 MHz), microwave plasmas[6] (frequencies a few GHz) and electron cyclotron resonance plasmas[7] (ECR, frequencies a few GHz).

In 1982 a research project was started at the Physics Department of the Eindhoven University of Technology to study the properties of RF plasmas that are used

for plasma etching. The first results were presented in the Ph.D. thesis of T.H.J. Bisschops[8], who built an etching station and developed a microwave setup for the measurement of electron densities in the plasma and a mass spectrometry setup to determine the ion energy distribution at the grounded electrode.

In 1987 a new reactor was designed to match the requirements of some new diagnostics. The results of the experiments and calculations on this reactor are presented in this work.

1.2 Etching in RF plasmas

Capacitively coupled RF plasmas have become widely applied for plasma assisted etching. In most cases the plasma is produced at 13.56 MHz. This is one of the internationally allowed frequencies for industrial usage. A parallel plate electrode geometry, often used in commercial etching reactors, is schematically depicted in figure 1.2. The plasma is generated by applying an RF voltage over the two electrodes, which produces an oscillating electric field in between. If the field is large enough, electrons gain enough energy from this field to produce positive ions and electrons by ionization of neutrals. The charged particles are lost by diffusion and recombination. Just after ignition of the plasma, the loss of electrons is greater than the loss of positive ions due to the higher mobility of the electrons with respect to the ions. As a result of this, the
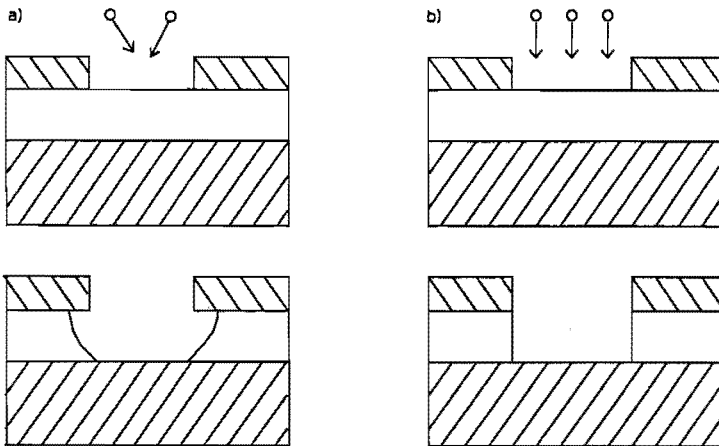
Fig. 1.1   *Reproduction of the mask pattern into the film with a) an isotropic etching process and b) an anisotropic etching process.*
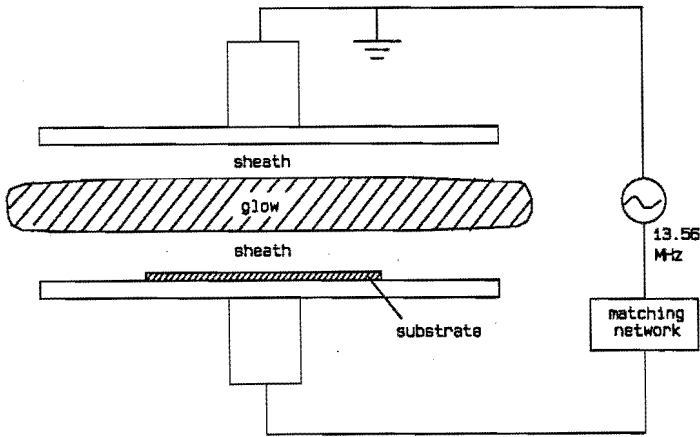
Fig. 1.2   *Parallel–plate electrode geometry that is in many cases used for plasma etching with a capacitively coupled RF plasma. If the substrate that is to be etched is mounted on the RF driven electrode one speaks of reactive ion etching (R.I.E.).*

plasma volume is charged positively. Therefore a DC electric field starts to build up between the center of the plasma and the electrodes. This results in a reduction of the electron loss and an enhancement of the positive ion loss. After some time the loss processes for positive and negative charge balance each other and balance the production processes. The DC electric field then stabilizes to its end value. In this situation the RF plasma can be roughly divided in two parts. Due to the self–generated DC electric field the regions close to the electrodes are depleted of electrons. These regions are usually referred to as 'sheaths'. In the central region of the plasma, usually called the glow, the electron density is much larger than in the sheaths. Most of the light emitted by the plasma is therefore coming from this region. The DC field in the sheath accelerates the positive ions to energies of tens to hundreds of electron volts (eV). As a result of this, the electrodes are continuously bombarded by energetic positive ions. The ion velocity is directed perpendicularly to the surface. Therefore a careful process design, in which the energetic ion bombardment is made essential for etching to take place, allows for highly anisotropic etching profiles[9].

Halogen—containing gases are used in most cases as the feeding gas for plasmas that are used for plasma etching. This due to to the fact that in this kind of plasmas atomic halogen radicals such as F, Cl, and Br, are formed that can react with

semiconductor materials such as Si, Ge, and GaAs. Examples of these gases are XeF_2, F_2, SF_6, Cl_2, C_xF_y and C_xCl_y (with $y=2x+2$)[10-12]. Besides free halogen radicals also halogen—containing molecular radicals are produced that can play either an etching or an inhibiting role. Moreover, due to the electronegative nature of halogens, not only positive ions but also negative ions can be formed easily in these plasmas. The kinetics and densities of all these particles are the subject of investigation in this study.

1.3 Scope of the thesis

Despite the fact that dry etching with RF plasmas is applied more and more in VLSI and ULSI microelectronics manufacturing, from a fundamental point of view many aspects of these plasmas are not understood. Especially the densities of reactive species such as neutral radicals[13] and ions[8,14] (both positive and negative) are not well known. Moreover, knowledge about the electron density and electron energy distribution[15,16] as a function of the various process parameters is scarce. Finally, though much work has been done on the characterization of the surface in beam etching experiments[10,17,18], only a few authors have worked on the effects of a real processing plasma on the state of the surface during etching[2,9,19]. Therefore much of the experimental data, needed to check models of RF etching plasmas that are presently being developed, is missing.

In this study a number of diagnostics have been developed to measure the densities of both neutral and charged species in RF plasmas of fluorocarbon gases that are widely used for etching of Si and of SiO_2 and to determine the etching characteristics of those discharges in various circumstances. The experimental results are compared with numerical models of the kinetics of both charged and neutral particles in the plasma. Furthermore the state of the surface has been analyzed *in situ*, to obtain information on etching mechanisms for Si and SiO_2 substrates in fluorocarbon plasmas.

The study emphasizes on CF_4 plasmas. Results in other fluorine-containing gases are used as a comparison.

In chapter 2 the reactor is described that has been used to produce the investigated RF plasmas and to study the etching process. Two different geometries are discussed in which the experiments have been performed. Furthermore some characteristics of the apparatus are given.

In chapter 3, numerical models are presented for the kinetics of charged particles (i.e. electrons, positive ions and negative ions) in an RF plasma of CF_4. For this gas a lot of data is available on the transport properties of electrons and ions[20-25]. These charged particle models have been used to analyze the behavior of the electron

temperature with the macroscopic plasma parameters and to investigate the densities of electron and ions in the plasma. The results are compared with the experiments (Chapter 5). Furthermore a model is presented for the time dependence of charged particle densities in the afterglow of an RF plasma of CF_4. This afterglow model has been used to extract rate coefficients for the recombination of positive and negative ions from measurements in the plasma (Chapter 5). Moreover, the importance of some reactions between ions and neutrals or electrons is discussed. In addition, a numerical model is presented which simulates the chemistry of the neutral particles in a plasma of CF_4. This neutral particle model is used to extract radical densities from the experimental data (see Chapter 5).

In chapter 4, the principles of the diagnostics that have been developed for the *in situ* measurement of the etch rate and the surface modification, and for the determination of particle densities in the RF plasma, are explained. The experimental setup for each diagnostic is described to some detail.

In chapter 5, the results of the experiments are presented and discussed in terms of the numerical modeling described in Chapter 3.

Finally, in chapter 6, some conclusions will be drawn.

References

1   S.M. Sze, *Semiconductor Devices Physics and Technology*,
        (John Wiley, New York, 1985).

2   G.S. Oehrlein, Y.H. Lee, *J. Vac. Sci. Techn.*, A5, 1585 (1987).

3   J.W. Coburn, H.F. Winters, *J. Appl. Phys.* 51, 2614 (1980).

4   H.O. Blom, C. Nender, S. Berg, H. Norstroem, *Vacuum*, 38, 813 (1988).

5   C.J. Mogab, A.C. Adams, D.L. Flamm, *J. Appl. Phys.* 49, 3796 (1979).

6   K. Suzuki, S. Okudaira, S. Nishimatsu, K. Usami, I. Kanomata,
        J. Electrochem. Soc. 129, 2764 (1982).

7   B. Petit, J. Pelletier, *Jap. J. Appl. Phys.*, 26, 825 (1987).

8   T.H.J. Bisschops, *Investigations on an RF plasma related to plasma etching*,
        (Ph.D. thesis, Eindhoven, 1987).

9   G.S. Oehrlein, H.L. Williams, *J. Appl Phys.* 62(2), 662 (1987).

10   J.W. Coburn, H.F. Winters, *J. Appl. Phys.* 50, 3189 (1979).

11   D.L. Flamm, V.M. Donnelly, J.A. Mucha, *J. Appl. Phys.* 52, 3633 (1981).

12   R. d'Agostino, D.L. Flamm, *J. Appl. Phys.* 52, 162 (1981).

13   I.C. Plumb, K.R. Ryan, Plasma Chem. Plasma Proc. 6, 205 (1986).

14   R.A. Gottscho, C.E. Gaebe, *IEEE trans. on Plasma Sc.* PS–14, 92 (1986).

15   M. Capitelli, M. Dilonardo, R. Winkler, J. Wilhelm,
      Contrib. Plasma Phys. **26**(6), 443 (1986).

16   P.M. Vallinga, *Modeling of RF plasmas in a parallel plate etch reactor*,
      Ph.D. thesis (Eindhoven 1988).

17   C.A.M. de Vries, A.J. van Roosmalen, G.C.C. Puylaert,
      J. Appl. Phys. **57**(9), 4386 (1985).

18   J.L. Buckner, D.J. Vitkavage, E.A. Irene, T.M. Mayer,
      J. Electrochem. Soc. **133**, 1729 (1986).

19   Ch. Cardinaud, G. Turban, S. Quillard, *Proc. ISPC IX*,
      Pugnochiuso, Italy 1989, 1583.

20   J. Dutton, A. Goodings, A.K. Lucas, A.W. Willams, Proc. ICPIG
      Swansea (1987), 20.

21   S.R. Hunter, J.G. Carter, L.G. Christophorou, *Phys. Rev.* **A38**(1), 58 (1988).

22   K. Masek, L. Laska, R. d'Agostino, F. Cramarossa,
      Contrib. Plasma. Phys. **27**, 15 (1987).

23   M.S. Naidu, A.N. Prasad, *J. Phys.* **D5**, 983 (1972).

24   C.S. Lakshminarasimha, J. Lucas, J. Price, *Proc. IEEE* **120**, 1044 (1973).

25   M. Hayashi, in *Swarm Studies and Inelastic Electron—Molecule Collisions*,
      edited by L.C. Pitchford, B.V. McKoy, A. Chutjian and S. Trajmar,
      (Springer—Verlag, New York, 1987).

2. EXPERIMENTAL APPARATUS

2.1 Introduction

In the use of dry etching processes for fabrication of large scale integrated circuits in the industry, there is a tendency to switch from batch processing to single wafer processing[1]. In this way it is easier to obtain a good wafer–to–wafer reproducibility. Single–wafer processing however requires higher etch rates as compared to batch processing to obtain an economic wafer throughput. These higher etch rates can be achieved by using a comparatively high RF power. However, this can result in damaging of the surface due to the high ion energy of the positive ions bombarding the surface at elevated power levels[2]. To optimize the performance of single–wafer reactors a lot of effort is put into the study of etching processes in this kind of reactors. The most common reactor geometry that is nowadays used for dry etching processes is the *parallel–plate* or *planar* geometry. A schematic view of such a reactor is depicted in figure 1.2. The experimental apparatus used for the experiments in this study is based on this geometry.

2.2 Electrode geometry

For the experiments in this study two electrode configurations have been used. Schematic drawings of both geometries are given in figure 2.1. In both cases the configuration has cylindrical symmetry around the vertical axis. In this situation it is easy to mount the wafers to be etched on the lower electrode. All electrodes were made of aluminum.

Part of the experiments have been performed in the standard parallel–plate configuration (figure 2.1a). In this geometry the plasma can easily be studied by optical methods (see sections 4.1 and 4.2). The electrode separation was 20 mm and the electrode radius was 62 mm. The gas was fed into the plasma region through a hole in the center of the upper electrode. In this way a more or less radial gas flow pattern is obtained. The reactor has been designed to operate (at low pressure) in the R.I.E. mode, where the substrate is bombarded by a high flux of positive ions. For this purpose the lower electrode (carrying the substrate) is connected to the RF voltage, whereas the upper electrode is grounded. Since the vacuum vessel is also grounded, the area of the grounded electrode is larger than the area of the driven electrode. As a result of this, the RF power density on the driven electrode is higher than on the grounded electrode. To prevent overheating of the driven electrode it is water–cooled.
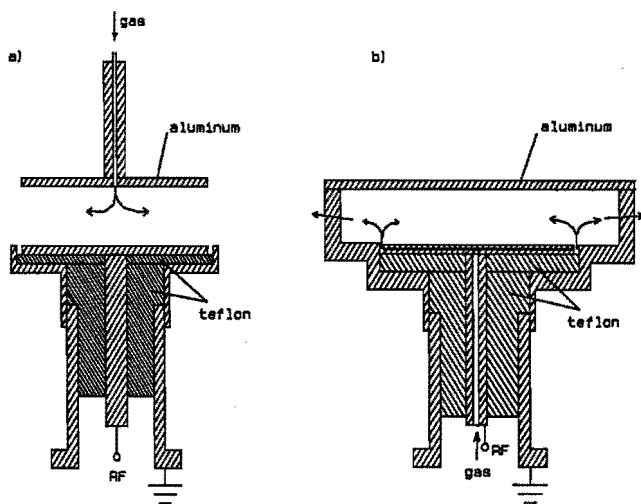
Fig. 2.1.   *Schematic view of the electrode geometries used in the experiments. The*
            diameter of the RF electrode is the same in both configurations
            a) Open configuration for the optical diagnostics
            b) Cavity configuration for the microwave cavity measurements

The other part of the experiments have been performed in a somewhat modified
parallel–plate electrode configuration. In this case the upper electrode is extended along
the side to create a microwave cavity which has been used for the diagnostics described
in section 4.3. This configuration is depicted in figure 2.1b. In this case the gas is fed
into the plasma region through the gap between the smaller, RF driven, electrode and
the larger grounded electrode. Four slits in the side of the cavity are used to allow the
gas to leave the cavity and enter the vacuum vessel. The slits are also used for emission
experiments and to direct a laser beam through the plasma for negative ion density
measurements (see section 4.3). The electrode separation in this case is also 20 mm. The
radius of RF driven electrode is also 62 mm, as in the open geometry, and the inner
radius of the cavity is 87.5 mm.

2.3 Vacuum system and gas handling

The electrodes between which the plasma is produced are positioned in the
middle of the vacuum vessel. The vessel itself has been depicted in figure 2.2. It has
cylindrical symmetry and it is made of stainless steel. It has a total height of 38 cm and
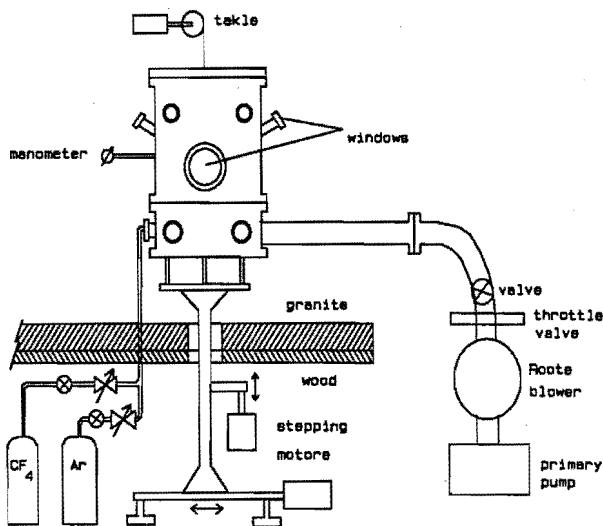
Fig. 2.2.   *Schematic view of the vacuum vessel in which the electrodes are positioned, the pumping system and the gas handling system. The lower and the upper part of the vessel can be separated by a tackle.*

a inner radius of 11 cm, and holds a number of ports and windows to allow the execution of the various diagnostics, such as ellipsometry, microwave resonance spectroscopy, emission spectroscopy, mass spectroscopy, infrared absorption spectroscopy and photodetachment spectroscopy. The upper part of the vessel can be lifted by a tackle to enable the replacement of wafers and for servicing purposes. The whole reactor can be moved horizontally and vertically by two stepper motors that are controlled by an IBM PC/AT to enable optical measurements as a function of the position in the plasma. All optical diagnostics are mounted on a 2500 kg granite table (size 250x160x10 cm) which is mechanically isolated from the floor by a wooden plate and rubber cylinders to avoid vibration in the optical systems. The translatable reactor support is mounted through a 18 cm diameter hole in the granite table. The pumping system consists of a 250 m^3/h Pfeiffer WKP 250 Roots blower combined with a 30 m^3/h Pfeiffer DUO 030 A double stage primary pump. An oil filter in between the Roots blower and the primary pump prevents oil from the primary pump to enter the vacuum vessel. The absolute gas pressure is measured with a MKS 370 HS–10 Baratron capacitance manometer (for normal plasma operation) and a Balzers IKR 020 Penning manometer (for determination of the base pressure). The base pressure is a few times 10^{-5} Torr. The gases (CF_4, C_2F_6, C_3F_8, CHF_3 and Ar) are fed through Tylan FC 260 mass flow
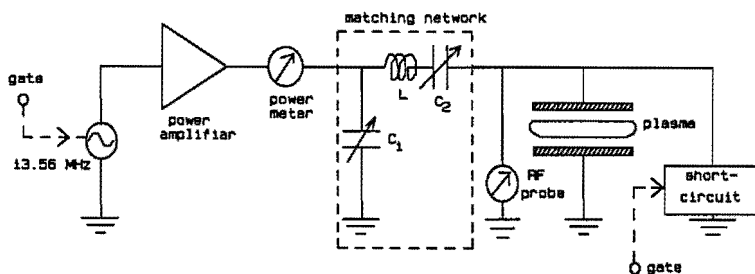
Fig. 2.3.   *The electrical circuit that is used to produce the plasma. The RF power is*
              matched to the plasma impedance by a matching network.

controllers. The gas flow and the pressure can be varied independently by changing the
pumping speed with a Balzers IB 063 throttle valve.

2.4 Electrical circuit

        The electrical circuit that is used to produce the plasma is depicted in figure 2.3.
The RF excitation voltage needed for the generation of the plasma is produced by a
combination of a Hewlett Packard 8116A function generator and a ENI 3100 LA power
amplifier. The amplifier is interlocked by a water flow meter in the cooling system of the
RF electrode to avoid application of the RF power without cooling of the electrode. The
RF power is fed into the reactor through a network that matches the output impedance
of the power amplifier to the impedance of the plasma. The input and reflected RF
power is measured by a Bird Model 4410 power meter, which is situated in between the
power amplifier and the matching network. Reflected power levels were always below
1 %. The RF voltage is connected to the lower electrode. Under the RF electrode a
grounded aluminum shield is positioned, to avoid the formation of a plasma under the
RF electrode. In this way the plasma is only generated between the two electrodes. The
RF function generator can be gated by a standard TTL signal to make it possible to
perform measurements in the afterglow of a plasma and to perform automatically
alternate measurements with and without plasma. For some afterglow experiments an
extra circuit was attached to the two electrodes, to shortcircuit the voltage between the
electrodes synchronously with the switch—off of the function generator. In this way the
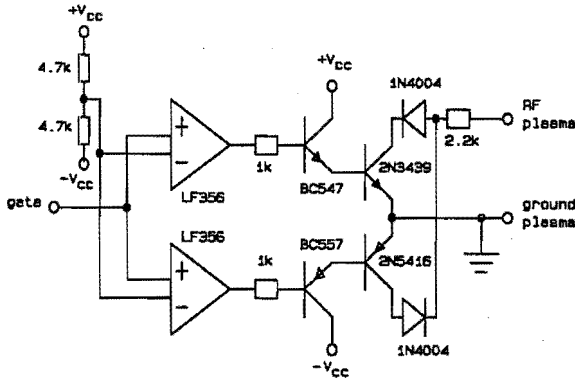
Fig. 2.4.   The circuit that has been used to shortcircuit the voltage over
the electrodes in some afterglow experiments.

plasma can be switched off very fast (within a few microseconds). This circuit is depicted in figure 2.4.

2.5 Characteristics of the reactor

The geometry of, especially, the cavity configuration is somewhat different from common reactor geometries. The two geometries may differ somewhat in electrical response. To be able to compare the results obtained in both geometries with each other and to transfer the findings in this study to other geometries, it is therefore necessary to characterize the configuration with respect to the RF voltages in several plasma circumstances. In figures 2.5 − 2.8 the RF and DC voltages between the electrodes in both configurations are given as a function of pressure and total RF power in plasmas in CF_4 and C_2F_6. It can be seen from these figures that the differences between both configurations are relatively small (± 20 %) in plasmas in CF_4 and CHF_3. Therefore with some prudence we can use results (e.g. electron densities) obtained in the cavity configuration also for the open configuration. For the case of C_2F_6 this was not done.
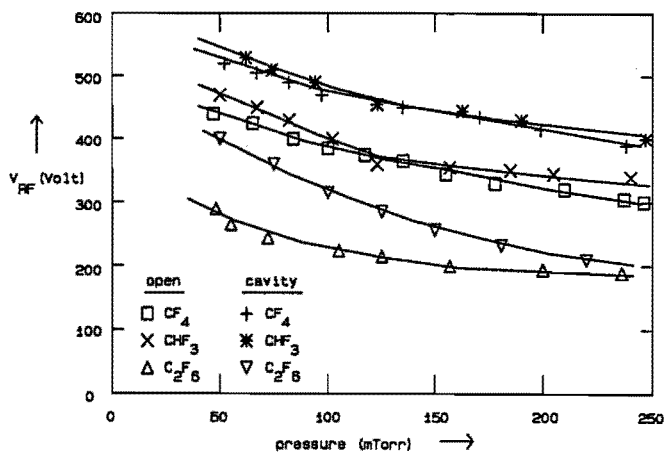
Fig. 2.5.   The RF voltages between the electrodes in both configurations as
             a function of the gas pressure in plasmas of CF_4, CHF_3 and C_2F_6 at 20 W
             RF power.
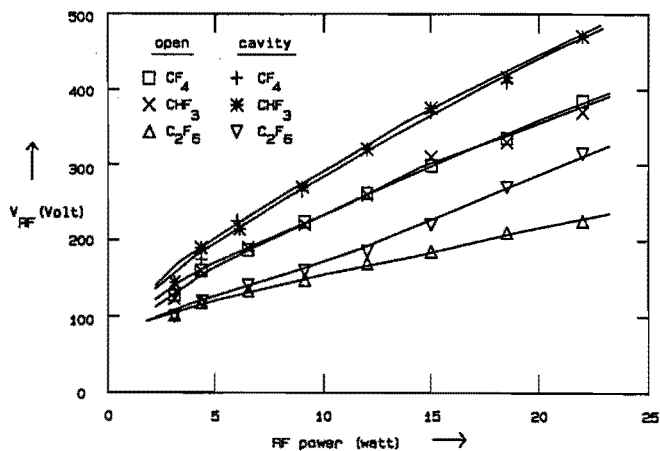
Fig. 2.6.   The RF voltages between the electrodes in both configurations as
             a function of the RF power in plasmas of CF_4, CHF_3 and C_2F_6 at a gas
             pressure of 120 mTorr
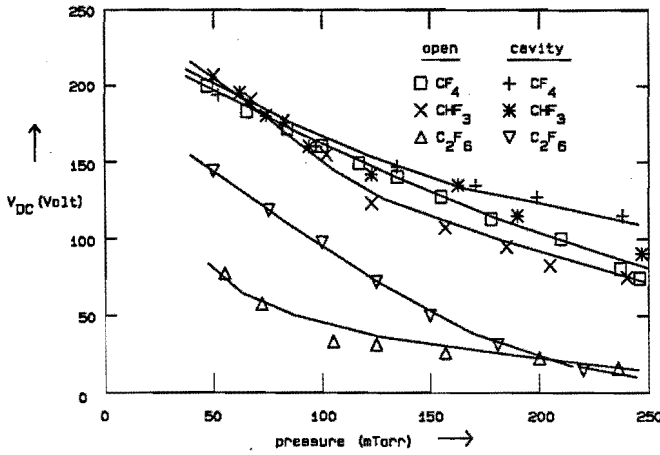
Fig. 2.7. The DC voltages between the electrodes in both configurations as a function of the gas pressure in plasmas of CF_4, CHF_3 and C_2F_6 at 20 W RF power.
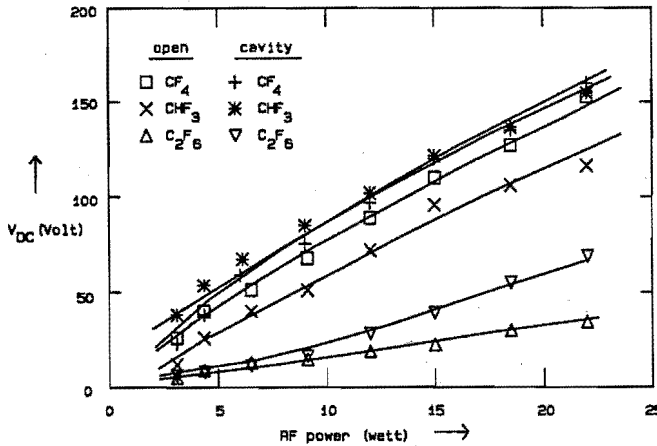
Fig. 2.8. The DC voltages between the electrodes in both configurations as a function of the RF power in plasmas of CF_4, CHF_3 and C_2F_6 at a gas pressure of 120 mTorr.

References

[1]   D.M. Manos, D.L. Flamm, *Plasma etching, an introduction* (Academic Press, London, 1989).

[2]   G.S. Oehrlein, R.M. Tromp, J.C. Tsang, Y.H. Lee, E.J. Petrillo, *J. Electr. Soc. Solid. State. Sc. Techn.* 132, 1441 (1985).

3. MODELLING

3.1 Introduction

In the field of the analysis of RF discharges used for plasma processing progress is slow. The main reason is that the physics and chemistry of halogen—containing plasmas in the volume as well as at the surface is not understood in a quantitative way. Reaction rates and transport coefficients are either not known or at best not very reliable. This means that the construction of a comprehensive model of such a discharge is a formidable task. In order to still provide for the interpretation of our experimental data on particle densities and kinetics the modelling problem is split up into a number of submodels. Here the effort concerns only CF_4 plasmas since for this gas the most data on transport properties and rate coefficients are available.

In the active plasma a distinction has been made between the modelling of the charged particle densities and the modelling of the neutral species formed in the plasma. It is difficult to treat both charged and neutral particles in one model since the time scale in which the reactions take place is very far apart. However, the charged particle balance the plasma can be considered separately since the feedback from the neutral densities to the charged particle densities can be supposed to be limited to reactions between negative ions and neutral radicals (i.e. detachment). If a good estimate can be made for these reaction rates, it is possible to solve the charged particle density problem without solving the neutral particle density problem. On the other hand in the equations for the neutral particle densities values for all charged particle densities and for the electron temperature should be used as input data.

In section 3.2 a two—dimensional simulation of the neutral particle kinetics in the plasma is described. In this simulation the charged particle densities have been taken from the experiment. The electron temperature has been used as a parameter. The neutral densities of CF_2 and C_2F_6 from the model calculations will be compared with *in situ* absolute density measurements of these species obtained by infrared absorption spectroscopy as described in section 5.2. From their comparison it was possible to obtain estimates for the values of the electron temperature and the density of CF_3 in the plasma.

In section 3.3 a simulation based on a fluid model for the kinetics of charged particles (i.e. electrons, positive ions and negative ions) in the plasma is presented. In this simulation the densities of neutral particles that can induce detachment of negative ions have been used as a parameter. The densities of electrons and negative ions will be compared with *in situ* measurements using microwave resonance and photo–detachment.

From this comparison it has been possible to obtain another estimate for the electron temperature.

In section 3.4 a simulation of the kinetics of the charged particles in the afterglow of the CF$_4$ plasma is presented. The plasma decay is calculated as a function of time after switching off the RF—input. The results of this simulation will be compared (in section 5.3) with experimental time—resolved measurements of the negative ion density. In this way it was possible to extract values of the rate for collisional detachment of negative ions with neutral radicals as a function of the macroscopic plasma parameters and of the rate coefficient for dissociative ion—ion recombination.

3.2 Neutrals

3.2.1 Introduction

It has been established that the radical chemistry has a large effect on the results of the etching process such as selectivity, anisotropy and etch rate[1-4]. In the literature a few papers[5-6] can be found on the chemistry of inductively coupled RF CF$_4$ plasmas in plug flow reactors at 500 mTorr. Both geometry and plasma parameters are in that case quite different from the situation in standard plasma etching processes where capacitively coupled parallel—plate reactors operating between 30—100 mTorr are used for most applications. Since the transport properties and reaction rates are a function of both pressure and geometry, the results of the chemistry in these plug flow situations need not be a reflection of the chemistry in real processing plasmas.

Moreover, recent measurements[7] using laser induced fluorescence (LIF) of CF$_2$ and CF suggest that at the pressure mentioned surface losses are much larger than volume losses for these radicals. Therefore, as surface effects may be very important for the neutral radical chemistry, these effects must be taken into account in any model of the kinetics of CF$_4$ etching plasmas.

Finally, in section 5.3 it will be shown that negative ions are present in high densities with respect to the electron density (see section 5.3). This may imply that reactions between positive and negative ions as well as reactions between ions and neutrals can give a significant contribution to the kinetics of the neutral particles in the plasma. The possible implications which that may have were not taken into account in the previously mentioned models[5-6].

3.2.2 Simulation of neutral particle densities in the plasma

In this section a model is presented for the neutral particle densities, in which the experimental data on charged particle densities (see section 5.3) are used to calculate the contribution of reactions involving charged particles. A two–dimensional model is presented, in which the effects of surface loss of radicals, gas flow, diffusion and reactions in the gas phase (including those involving positive and/or negative ions) are calculated as a function of time. The results of the calculation will be compared (in section 5.2) with *in situ* infrared (IR) absorption measurements of the glow–region spatial average of the C_2F_6–density at 30–200 mTorr and flows at 3–50 sccm, and the CF_2 density at 100 mTorr pressure and 50 sccm flow. The simulation was performed at 100 mTorr, 50 sccm flow and 80 watt power ($0.66 \ W/cm^2$). The parameters of the model have been tuned with the rate coefficients of reactions involving electrons, which are a function of the electron temperature, to fit the experimental results at these conditions.

In RF etching plasmas, the reactive particles (ions and radicals) are produced by dissociation induced by energetic electron impact. Since the RF modulation of the electron and ion densities and the electron temperature T_e takes place on a much faster time scale than the neutral particle reaction time constants, the charged particle densities and T_e have been taken as appropriate averages. The radicals can recombine with each other in the gas phase or at the walls of the reactor to form recombination products. Furthermore transport of the radicals and recombination products by diffusion and gas flow takes place and determines the heterogeneous loss processes. The processes taking place in the plasma and at the walls determine the densities in the volume and the fluxes of the radicals to the electrode where etching can take place. For simplicity a situation has been studied in which no semiconductor substrate was present in the reactor. In the model it is assumed that the plasma is produced in a cylindrically symmetrical parallel–plate reactor with a buffer volume (see figure 3.1). This geometry is almost equal to that of the reactor (i.e. the open configuration) that has been used for the infrared absorption measurements. As a result of the cylindrical symmetry the model can be restricted to two dimensions. The reactor volume has been divided in a number of control volume elements. In the radial direction a constant step size (of 10 mm) between the volume elements was taken throughout. In the axial direction a constant step size (of 2 mm) was taken in the plasma region, and a variable step size (up to 10 mm) outside the plasma region. In the model a starting condition was chosen from which a solution develops through application of the continuity equation, combined with Gauss's theorem with a source term. This was applied on each of a series of control volumes V with area A as given by
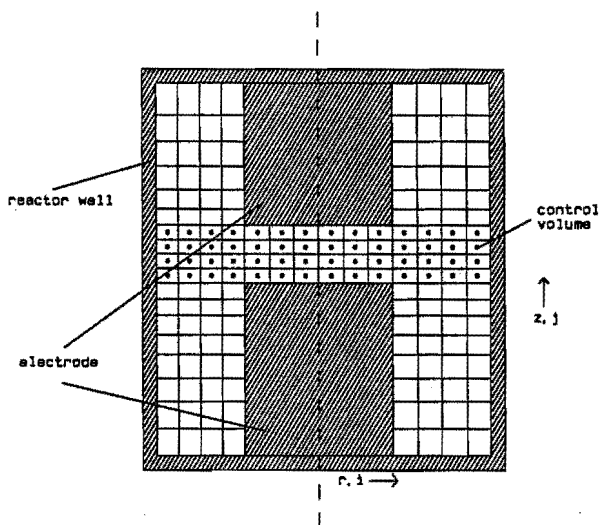
Fig. 3.1   Geometry of the reactor in the neutral particles kinetics simulation. The
dimensions are the same as in the experimental reactor with the open
configuration. Flow has only been considered in the region marked with
dots and is thought to be purely in the radial direction.

$$\iiint\limits_{V} \frac{\partial n}{\partial t}\, dV = -\iint\limits_{A} \vec{j}\, d\vec{A} + \iiint\limits_{V} \frac{dn}{dt}\Big|_{\text{react}}\, dV, \qquad\qquad (3.1)$$

where $\vec{j}$ is the particle current density at a position on the boundary of the control
volume.

The net density gain or loss for particles in each volume element was calculated
until stabilization of all the densities occurred. The details of the numerical model will
be described in three parts, a) reactions in the gas phase, b) particle transport (flow and
diffusion) and c) radical loss and recombination at the surface.

a) Gas phase reactions

For the gas phase a reduced set of reaction rate equations, based on a paper by
Ryan and Plumb[6], and extended with some reactions involving positive and negative
ions, has been used. The species for which the density is calculated in the model are
CF_4, CF_3, CF_2, F, and C_2F_6. The implemented reactions are given in Table 3.1. The
other particles involved in the reactions in this table are either input (such as the

charged particles) or supposed to be present in a small density (C_2F_5). The gain per unit time for a species C by a reaction A + B $\longrightarrow$ C in a control volume (i,j) is given by

$$\dot{n}_{c;reac}^{ij} = k_{ab}^c \cdot n_a^{ij} \cdot n_b^{ij}, \qquad\qquad (3.2)$$

where i and j are the indices for the radial and axial directions respectively, and n^{ij} is the density in the volume element labeled by i and j. The reaction is accounted for by increasing the density of C and decreasing the densities of A and B by the amount given in (3.2). Since within the framework of this model we are only interested in neutral particle densities and furthermore the charged particle densities are known from the microwave resonance experiments (see sections 4.3 and 5.3), the charged particle density profiles were fixed in the simulation. The densities of the negatively charged particles were taken from the experiment and the positive ion densities were obtained using quasi-neutrality in the glow region.

In the reactions involving electrons a key parameter determining the rate is the electron temperature T_e (= average electron energy). In the plug flow paper of Ryan and Plumb[6] the characteristic energy v_e ($=D_e/\mu_e$) was taken to be 4.5 eV, and it was assumed that the shape of the electron energy distribution function (EEDF) is close to Druyvesteyn. For the reasons to be discussed in section 5.3, it is in our situation likely that T_e has a value such that the ionization coefficient is more or less equal to the attachment coefficient (k_3 in Table 3.1). This yields a T_e of around 4 eV. In the thesis of Vallinga[8] it was derived from a Boltzmann analysis that v_e is about 20 % higher than T_e and that in our situation the EEDF is probably closer to a Maxwellian. Therefore v_e is slightly higher than the value reported by Ryan and Plumb[6]. Moreover, since the EEDF is closer to a Maxwellian than was accounted for by these authors, the tale of the distribution will be less depleted than they assumed. Since the threshold for dissociation of CF_4 is 12.5 eV [9], the electrons in the high—energy tail of the distribution are responsible for all dissociative processes involving electrons. If the tale is somewhat less depleted and the average energy is slightly higher we can in our situation expect that the rate coefficients for reactions of electrons with neutrals will be somewhat higher than in the situation described by Ryan and Plumb[6].

Since it is still not well known what the shape of EEDF is like and how this function depends on the spatial position in the plasma it is not possible to accurately predict the values for the rate coefficients of reactions involving electrons. We have therefore taken all these coefficients from ref. 6 and have multiplied them by the same factor f^* (which is a function of T_e) to match the experimentally determined value for the density of CF_2. In table 3.2. some results are shown as a function of this factor. The

Table 3.1   The gas phase reactions in the model. The coefficient for the reactions
involving electrons were corrected to match the experimental value of
$[CF_2]$. The effect of reactions (9) and (11) on the C_2F_6 loss is small if $X =$
C_2F_5 since most of the C_2F_5 will recombine with fluorine (13) to form
C_2F_6.

	Reaction			ref.	
(1)	$CF_4 + e$	$\longrightarrow$	$CF_3 + F + e$	6	$k_1 = 1.5 \cdot 10^{-16}$ m^{3}s^{-1}
(2)	$CF_4 + e$	$\longrightarrow$	$CF_2 + 2F + e$	6	$k_2 = 3.5 \cdot 10^{-16}$ m^{3}s^{-1}
(3)	$CF_4 + e$	$\longrightarrow$	$CF_3 + F^-$	15	$k_3 = 4 \cdot 10^{-17}$ m^{3}s^{-1}
(4)	$CF_3 + e$	$\longrightarrow$	$CF_2 + F + e$	6	$k_4 = 5 \cdot 10^{-16}$ m^{3}s^{-1}
(5)	$2CF_3 + CF_4$	$\longrightarrow$	$C_2F_6 + CF_4$	10	$k_5 = 4 \cdot 10^{-18}$ m^{3}s^{-1}
(6)	$CF_3 + F + CF_4$	$\longrightarrow$	$2\,CF_4$	6	$k_6 = 1.2 \cdot 10^{-17}$ m^{3}s^{-1}
(7)	$CF_3 + F^-$	$\longrightarrow$	$CF_4 + e$	5	$k_7 = 5 \cdot 10^{-15}$ m^{3}s^{-1}
(8)	$CF_2 + F^-$	$\longrightarrow$	$CF_3 + e$	5	$k_8 = 5 \cdot 10^{-16}$ m^{3}s^{-1}
(9)	$C_2F_6 + e$	$\longrightarrow$	$X + F + e$	est.	$k_9 = 2 \cdot 10^{-16}$ m^{3}s^{-1}
(10)	$CF_3^+ + F^-$	$\longrightarrow$	$CF_3 + F$	5	$k_{10} = 5 \cdot 10^{-13}$ m^{3}s^{-1}
(11)	$C_2F_6 + e$	$\longrightarrow$	$X + F^-$	15	$k_{11} = 5 \cdot 10^{-16}$ m^{3}s^{-1}
(12)	$C_2F_6 + e$	$\longrightarrow$	$2\,CF_3 + e$	est.	$k_{12} = 2 \cdot 10^{-16}$ m^{3}s^{-1}
(13)	$C_2F_5 + F + CF_4$	$\longrightarrow$	$C_2F_6 + CF_4$		

Table 3.2   Calculation of the densities of CF_2 and CF_3 as a function of the correction
factor f^* (see text). A correction of only 1.5 with respect to the values given
by Ryan et al.[6] can explain the observed density of CF_2 (see section 5.2).

f^*	$[CF_2]$ (m^{-3})	$[CF_3]$ (m^{-3})
0.75	$4.9 \cdot 10^{18}$	$3.32 \cdot 10^{18}$
1.50	$9.8 \cdot 10^{18}$	$4.88 \cdot 10^{18}$
3.00	$2.0 \cdot 10^{19}$	$7.36 \cdot 10^{18}$

present results indicate a difference of only 50% in the rate coefficients for reactions
involving electrons with respect to the values given by Ryan et al.[6].
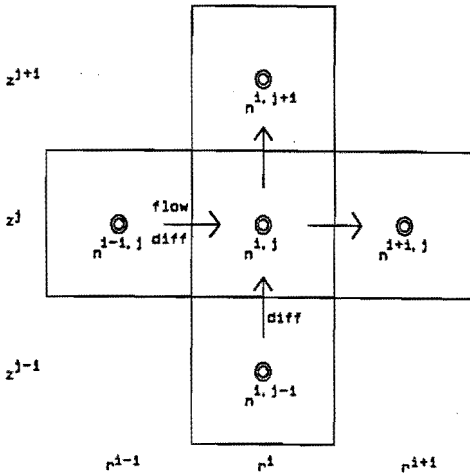
Fig. 3.2.   *Schematic representation of the particle fluxes through the boundary of a volume element in the neutrals kinetics simulation.*

b) Transport by diffusion and flow

The transport in the gas phase is described by an explicit first order scheme. The net gain and loss of particle density in a volume element is calculated directly from the fluxes through the boundaries between volume elements. The advantage of this over a discretization of the diffusion equation is that the mass balance is always correct, which needs not to be in the latter method. The particle fluxes have been depicted schematically in figure 3.2. In the axial direction (z) only diffusion is taken into account (the flow is assumed to affect only the radial direction). In the radial direction (r) both flow and diffusion are taken into account. The particle current density j through a boundary caused by diffusion is given by

$$j = -D \frac{\partial n}{\partial x}\Big|_{x=x_{\text{boundary}}}, \qquad (3.3)$$

where D is the diffusion coefficient of the species concerned. The diffusion coefficients were derived from the measured[11] diffusion coefficient of CF and corrected for the reduced mass[12]. Therefore the net density gain per unit time of control volume (i,j) by axial diffusion $\dot{n}_{\text{dif,z}}^{ij}$ (with contributions from the upper and lower boundaries) can be written as

$$\dot{n}_{\text{dif},z}^{ij} = \frac{2 \cdot D}{z^{j+1}-z^{j-1}} \left[\frac{n^{j+1}-n^j}{z^{j+1}-z^j} - \frac{n^j-n^{j-1}}{z^j-z^{j-1}} \right] \tag{3.4}$$

In a similar way the net density gain per unit time of control volume (i,j) by radial diffusion $\dot{n}_{\text{dif},r}^{ij}$ can be calculated to be

$$\dot{n}_{\text{dif},r}^{ij} = -D \cdot \left[\frac{4(n^i-n^{i+1})(r^i+r^{i+1})}{(r^{i+1}-r^i)\{(r^i+r^{i+1})^2-(r^i+r^{i-1})^2\}} - \right.$$
$$\left. \frac{4(n^{i-1}-n^i)(r^i+r^{i-1})}{(r^i-r^{i-1})\{(r^i+r^{i+1})^2-(r^i+r^{i-1})^2\}} \right]. \tag{3.5}$$

Since it is assumed that there is only radial flow, the number of (neutral) particles N_{flow}^i that are transported by flow from one volume element to the next per unit time can be written as

$$N_{\text{flow}}^i = \tfrac{1}{2}(n^i+n^{i-1}) \cdot \frac{f}{60} \frac{p_0}{p}, \tag{3.6}$$

where f is the mass flow (in sccm), p_0 is the standard atmospheric pressure, and p is the pressure in the plasma. The gas flow contribution in the radial direction $\dot{n}_{\text{flow},r}^{ij}$ can then be calculated to be

$$\dot{n}_{\text{flow},r}^{ij} = -\frac{f\,p_0}{60\,p\,\pi\,d}\,\frac{2\,(\,n^{i+1}-n^{i-1}\,)}{(r^{i+1}+r^i)^2-(r^i+r^{i-1})^2}, \tag{3.7}$$

where d is the distance between the electrodes.

c) Surface reactions

Only surface reactions for particles that can stick to the surface and which are present with significant densities have been taken into account (i.e. F, CF_2, CF_3). Particles that have too small a sticking coefficient or too small a density are not considered. Furthermore only reactions at the electrodes have been taken into account. The reactions at the surface that have been considered are given in Table 3.2. The fluence of particles $\vec{j}_{\text{in}}$ towards the electrode surface is given by

$$\vec{j}_{\text{in}} = \left[\frac{n_{\text{surf}}}{4} \left(\frac{8kT}{\pi\,m} \right)^{0.5} + \tfrac{1}{2} D \frac{\partial n}{\partial z} \Big|_{\text{surf}} \right] \cdot \vec{e}_z, \tag{3.8}$$

Table 3.3   *The surface reactions in the model. The sticking coefficient for CF_2 was taken from ref. 7. The sticking coefficients for F was taken from ref. 5. The sticking coefficient of CF_3 has been used to fit the simulation to the experimental value of the C_2F_6 density.*

(14)	F	$\longrightarrow$	$F_{(s)}$	$s(F) = 0.002$
(15)	CF_3	$\longrightarrow$	$CF_{3(s)}$	$s(CF_3) = ?$
(16)	CF_2	$\longrightarrow$	$CF_{2(s)}$	$s(CF_2) = 0.06$
(17)	$F_{(s)} + CF_3$	$\longrightarrow$	$CF_4\uparrow$	fast
(18)	$CF_{3(s)} + F$	$\longrightarrow$	$CF_4\uparrow$	fast
(19)	$CF_{2(s)} + F$	$\longrightarrow$	$CF_{3(s)}$	fast

where m is the mass of the particle, n_{surf} is the particle density just above the surface, T is the gas temperature and $\vec{e}_z$ is the unit vector in the z–direction. The flux consists of a thermal contribution (the first term in (3.8)) and a diffusion–driven contribution (the second term in (3.8)). The total radical density gain per unit time in the axial direction in the last volume element (i,j) above the bottom electrode surface $\overset{.10}{n}_{surf,z}$ caused by surface loss can hence be written as

$$\overset{.10}{n}_{surf,z} = - \left[\frac{n^0}{4} \left(\frac{8kT}{\pi m} \right)^{0.5} + \tfrac{1}{2} D \frac{n^1-n^0}{z^1-z^0} \right] \frac{s}{z^1-z^0} , \qquad (3.9)$$

where s is the sticking probability (i.e. the fraction of the incoming flux that sticks to the surface). The expression for the upper electrode surface is similar.

The surface densities of F, CF_2 and CF_3 are assumed to be constant and are therefore not calculated explicitly. Reactions on the surface are accounted for by decreasing the F density in the last volume element above the surface by the amount corresponding to the CF_3 surface loss and twice the CF_2 surface loss (It is assumed that the end product is only CF_4). This means that only reactions of CF_2 and CF_3 radicals at the surface with incoming fluorine radicals are considered. If polymerization occurs on the electrodes, this assumption leads to some over-estimation of the total surface loss for fluorine. For the CF_2 radical a value of $s(CF_2) = 0.06$ on aluminum was established from LIF decay measurements[7]. For CF_3 however no accurate experimental data are available. The value of $s(CF_3) = 0.002$ as taken by Edelson et al.[5] (wall material not specified) has been used as a starting value and $s(CF_3)$ has been tuned to fit the experimentally observed C_2F_6 densities in the plasma.

The calculation was started with only CF_4 and all charged particles (at fixed densities) present. Time steps of 1 μs were calculated until all densities in the model became constant. This occurred after about $5 \cdot 10^6$ steps. By varying f^* (and therefore T_e) the CF_2 density was fit and by varying $s(CF_3)$ the C_2F_6 density was fit to the experimental values.

3.3 Charged particles

3.3.1 Introduction

As was already stated in section 3.2.1, neutral radicals play an important role in the etching process. The production of these neutral particles is determined largely by the electron density, ion densities (both positive and negative) and the electron temperature. Moreover, positive ions bombarding the substrate can have a large influence on the etching profile and the selectivity[2,4]. Also damaging of the surface during the process will take place. The positive ion energy distribution at the surface is directly related to the sheath potential between the glow and the electrodes. The presence in the plasma of negative ions in large quantities can have an influence on both the sheath potential and on the positive ion densities in the plasma.

Therefore, any attempt to model a halogen—containing RF plasma should include the negative ion density as a parameter. In section 3.3.2 a model is presented for the kinetics of the charged particles in the plasma for pressures between 200 — 500 mTorr. Furthermore, in section 3.3.3 a model is given that can be used to predict the behavior of the charged particle densities in the afterglow of a CF_4 plasma.

3.3.2 Simulation of the kinetics in the plasma

In order to analyze the impact of the presence of negative ions on the kinetics of the charged particles and, especially, on the electron temperature in the plasma, a numerical simulation program is currently being developed at the FOM Institute for Plasma Physics "Rijnhuizen" in Nieuwegein (NL). This program has been used to simulate the basic kinetics of charged particles in an RF CF_4 plasma at 13.56 MHz. The method is based on an article by Boeuf[13] and uses a fluid model of the plasma in which the continuity equations for all charged particles, together with Poisson's equation are solved numerically and self—consistently in one dimension. For CF_4 sufficient data is available on the transport coefficients and reaction rate coefficients[14-19]. These data were not yet used in the model by Boeuf[13], where some *ad hoc* assumptions were made for the

transport coefficients and the reaction rate coefficients. Furthermore detachment of negative ions by neutral radicals was not taken into account in that model. Since from the afterglow experiments and simulation it will be deduced (see section 5.3) that collisional detachment rates can be of the same order of magnitude as ion–ion recombination rates, we have added the detachment process and inserted the existing experimental data on transport coefficients and reaction rate coefficients into the model. The continuity equations for the charged particles are given by

$$\frac{\partial n_e}{\partial t} + \frac{\partial(n_e v_e)}{\partial x} = (k_i - k_a)\, n_e\, [CF_4] + k_d\, [CF_x]\, n^- \tag{3.10}$$

$$\frac{\partial n^+}{\partial t} + \frac{\partial(n^+ v^+)}{\partial x} = k_i\, n_e\, [CF_4] - k_r\, n^-\, n^+ \tag{3.11}$$

$$\frac{\partial n^-}{\partial t} + \frac{\partial(n^- v^-)}{\partial x} = k_a\, n_e\, [CF_4] - k_r\, n^-\, n^+ - k_d\, [CF_x]\, n^- \ . \tag{3.12}$$

where k_i, k_a, k_d and k_r are the rate coefficients for ionization, attachment, detachment with neutral radicals and ion–ion recombination, respectively. Recombination of electrons and ions was not taken into account since this process is not expected to be very important at the electron temperatures concerned. The total particle velocities v_e, v^+ and v^- are given by

$$n_i\, v_i = n_i\, \mu_i\, E - \frac{\partial(n_i D_i)}{\partial x}\ , \quad i = e, +, - \ . \tag{3.13}$$

The ionization and attachment rate coefficients are calculated from their corresponding coefficients α and η (which are known as a function of E/N) by taking $k_i = \alpha\, |\mu_e E|$ and $k_a = \eta\, |\mu_e E|$. The rate coefficient for collisional detachment was obtained from the analysis of the time dependence of n_e and n^- in the afterglow (see sections 3.3.3 and 5.3). The mobilities and diffusion coefficients for the positive and negative ions (D^+, D^-, μ^+ and μ^-) were taken from ref. 14, the electron mobility μ_e as a function of the reduced electric field E/N from ref. 15 and the diffusion/mobility ratio for the electrons D_e/μ_e as a function of E/N from ref. 16–18. The major positive ion was assumed to be CF_3^+ and the mobility for this ion was taken equal to the mobility of CF_3^- (from ref. 14). The major negative ion was taken to be F^-. The rate coefficients for dissociative attachment and ionization k_a and k_i as a function of E/N were taken from ref. 15 and 19. In contrast to Boeuf[13] we calculated the drift velocity v_e of the electrons directly from the value of E/N. The dissipated RF power density was tuned by varying the RF–voltage over the

electrodes. Assuming that the RF power is dissipated by the electrons the power density $P_{\rm rf}$ (in W/cm^2) can be calculated by

$$P_{\rm rf} = \int\limits_0^d \vec{j}_e(x).\vec{E}(x)\ \mathrm{d}x = -\ e\int\limits_0^d n_e(x)\vec{v}_e(x).\vec{E}\ \mathrm{d}x\ . \tag{3.14}$$

where x is the one–dimensional position in the plasma and $\vec{j}_e$ is the electron current density. The reference position ($x=0$) is situated at the grounded electrode. The RF driven electrode is situated at $x=d$. The contribution of the positive ions to the power dissipation is calculated in a similar way. In all cases it was found that more than 80% of the RF power is dissipated by the electrons. The simulation of the charged particle kinetics is performed until all densities and the electric fields are almost periodic functions of time. In the end situation the model yields both the charged particle densities and the electric field strength and potential as a function of the position. From E/N a value of T_e can be deduced.

The model assumes local equilibrium[13], in which it is implicitly assumed that the reaction coefficients and transport coefficients depend only on the local electric field. For the reaction coefficients this is only valid when the energy dissipation frequency is larger than the electric field frequency. For the frequency used in this study (13.56 MHz) this means that the model is strictly only valid at high pressure. In a paper by Winkler et al.[20] a Boltzmann analysis of the isotropic and anisotropic part of the EEDF is given for the case of H$_2$ and Ne plasmas. They found that for $\omega_{\rm rf}/p < 10^9$ s^{-1}Torr^{-1} the anisotropic part of the EEDF (which determines the impulse dissipation) is highly modulated in both Ne and H$_2$. In our case this would mean that the described transport model is correct for pressures down to 100 mTorr. However, Winkler et al.[20] found that in H$_2$ the isotropic part of the EEDF (which determines the energy dissipation) is only modulated for $\omega_{\rm rf}/p < 10^8$ s^{-1}Torr^{-1}. In our case this means that the reaction coefficients would only be modulated at pressures down to 1 Torr. Even then the validity of the model may be questionable in the sheath region since the electric field is strongly dependent on the position in that region[13]. We have nevertheless used the model at lower pressures (200–500 mTorr) to obtain qualitative insight on the behavior of the charged particles in the plasma with macroscopic parameters and to get an estimate of the electron energy (T_e) to compare with the value found using the neutral particle model.

3.3.3 Simulation of the kinetics in the afterglow

For the model presented in the previous section it is necessary to have some information on the rate coefficients of reactions of charged particles with each other and with neutrals. However, not all coefficients are known in the literature. For instance, the rate coefficient for ion–ion recombination and the rate coefficient for collisional detachment of negative ions with neutral radicals are not known. These data have been obtained by fitting the experimental values of n^- as a function of time (see section 5.3) to the calculated values with the rate coefficients mentioned in the afterglow of an RF CF_4 plasma. These measurements will be interpreted using a kinetic model for the densities of electrons and negative ions as a function of time in the afterglow.

Since after sufficient time in the afterglow (a few tens of microseconds) the relative spatial profiles of the charged particle densities become almost constant[21], the transport losses can be simplified to only the first mode of diffusion. Production processes can be neglected since the electron temperature decreases fast after plasma switch–off. Therefore after only a few microseconds ionization and attachment processes with fluorocarbon species can not take place anymore. However, since the electron temperature in the afterglow will be much lower than in the active plasma, electron–ion recombination has to be (in contrast to the modelling in the plasma) taken into account. Taking ion–ion recombination, electron–ion recombination, collisional detachment with neutrals, and diffusion into account, and using quasineutrality (this is valid for $n_e \gtrsim 10^{12}$ m^{-3}) we can write :

$$\frac{dn^-}{dt} = -\frac{D_{eff}^n}{\Lambda^2} n^- - k_r n^- (n^- + n_e) - k_d' \exp(-t/\tau) n^- \tag{3.15}$$

$$\frac{dn_e}{dt} = -\frac{D_{eff}}{\Lambda^2} n_e + k_d' \exp(t/\tau) n^- - k_{re} n_e (n^- + n_e)$$

$$- k_a n^- [F_2] \tag{3.16}$$

In these expressions k_r is the rate coefficient for ion–ion recombination, k_{re} is the rate coefficient for electron–ion recombination, D_{eff} the effective electron diffusion coefficient and D_{eff}^n the effective negative ion diffusion coefficient. From a more elaborate analysis of the diffusion process for negative ions in afterglow[21] it can be shown that diffusion of negative ions can be neglected as compared to detachment and recombination. Since the electron temperature decreases rapidly after plasma switch–off, dissociative attachment to C_xF_y species is not possible in the afterglow. However, if a significant amount of F_2

exists, dissociative attachment to that species is possible, since the threshold energy for this process is small[22]. Since $[F_2]$ is not known, only the time–dependence of the negative ion density (using (3.15)) was fit to the experimental time–dependency. The effective rate for collisional detachment with neutrals

$$F^- + CF_x \longrightarrow CF_{x+1} + e^-$$

k_d' is given by $k_d' = k_d \cdot [CF_x]$, where k_d is the rate coefficient for collisional detachment with neutral radicals. The density of the detaching species (CF_2 and CF_3 radicals) is assumed to decrease as a function of time with time constant τ. Λ is the characteristic diffusion length. The positive and negative ions were taken to be CF_3^+ and F^- respectively. The effective electron ambipolar diffusion coefficient D_{eff} is given by[23]

$$D_{eff} = \frac{\frac{T_e}{T_i}\{D^+(\beta+1) + D^-\beta\} + D^+ + \beta(D^+ - D^-)}{1 + \frac{\mu^- + \mu^+}{\mu_e}\beta} \tag{3.17}$$

where $\beta = \frac{n^-}{n_e}$, T_i is the ion temperature (assumed equal for positive and negative ions), T_e is the electron temperature, μ^- and μ^+ the ion mobilities and D^- and D^+ the ion diffusion coefficients. The calculation of the n^- decay is started using densities from the experiment. The values of k_d' and k_r have been determined by fitting the calculated decay curve of the negative ion density to the experimentally obtained curves.

References

1   C.J. Mogab, A.C. Adams, D.L. Flamm, *J. Appl. Phys.* **49**, 3796 (1979).

2   G.S. Oehrlein, H.L. Williams, *J. Appl Phys.* **62**(2), 662 (1987).

3   M. Haverlag, G.M.W. Kroesen, C.J.W. de Zeeuw, T.H.J. Bisschops,
       Y. Creyghton, F.J. de Hoog, *J. Vac. Sci. Techn.* B7, 529, (1989).

4   D.M. Manos, D.L. Flamm, *Plasma etching, an introduction*, (Academic Press,
       New York, 1989).

5   D. Edelson, D.L. Flamm, *J. Appl. Phys.* **56**(5), 1522 (1984).

6   K.R. Ryan, I.C. Plumb, *Plasma Chem. Plasma Proc.* **6**(3), 231 (1986).

7   J.P. Booth, G. Hancock, N.D. Perry, M.J. Toogood, *J. Appl. Phys.* **66**(11), 5251
       (1989).

8   P.M. Vallinga, *Modelling of RF plasmas in a parallel plate etch reactor*,
       Ph.D. thesis (Eindhoven 1988).

9   H.F. Winters, M. Inokuti, *Phys. Rev.* **A25**(3), 1420 (1982).

10   N. Selamoglu, M.J. Rossi, D.M. Golden, *Chem. Phys. Lett.* **124**, 68 (1986).

11   M. Magane, N. Itabashi, N. Nishiwaki, T. Goto, C. Yamada, E. Hirota,
     Proc. 7th Symp. Plasma Processing, Tokyo, Japan, Jan. 25–26 1990.

12   J.O. Hirschfelder, C.F. Curtis, R.B. Bird, *Molecular theory of gases and liquids*,
     (John Wiley, New York, 1954), 539.

13   J.P. Boeuf, *Phys. Rev.* **A36**(6), 2782 (1987).

14   J. Dutton, A. Goodings, A.K. Lucas, A.W. Willams, *Proc. ICPIG*
     Swansea (1987), pp 20.

15   S.R. Hunter, J.G. Carter, L.G. Christophorou, *Phys. Rev.* **A38**(1), 58 (1988).

16   K. Masek, L. Laska, R. d'Agostino, F. Cramarossa, *Contrib. Plasma. Phys.* **27**,
     15 (1987).

17   M.S. Naidu, A.N. Prasad, *J. Phys.* **D5**, 983 (1972).

18   C.S. Lakshminarasimha, J. Lucas, J. Price, *Proc. IEEE* **120**, 1044 (1973).

19   M. Hayashi, in *Swarm studies and Inelastic Electron–Molecule Collisions*,
     edited by L.C. Pitchford, B.V. McKoy, A. Chutjian and S. Trajmar
     (Springer–Verlag, New York, 1987), pp. 167.

20   R. Winkler, J. Wilhelm, A. Hess, *Ann. Physik Leipzig* **42** (1985), 537

21   A. Kono, M. Haverlag, G.M.W. Kroesen, F.J. de Hoog,
     submitted to J. Appl. Phys.

22   B.M. Smirnov, *Negative ions*, (McGraw–Hill, New York, 1982), ch. 4–6.

23   E.J.R. Hollahan, A.T. Bell, *Techniques and Applications of Plasma Chemistry*,
     (John Wiley, New York, 1974).

4. DIAGNOSTICS

To *in situ* monitor the plasma and the etching process a number of diagnostics have been developed and used. To measure the etch rate and to study the surface conditions during etching time–resolved single–wavelength ellipsometry has been applied. To determine the absolute densities of neutral species in the plasma a Fourier Transform infrared spectrometer has been constructed to perform measurements of the IR absorption of the plasma. To determine the absolute densities of negatively charged particles (electrons and negative ions) in the plasma a microwave resonance method combined with laser induced photodetachment has been applied. In this chapter these methods and their experimental setup will be shown.

4.1. Ellipsometry

4.1.1 Introduction

Various methods are being used to determine the etch rate of plasma–etching processes. They can be classified roughly into two groups: real time *in situ* methods which continuously monitor the effect of the plasma on the etching process and stylus methods where the effect of the plasma on the wafer is only observed after completion of the etching process. Within the first group, in addition to the use of an oscillating quartz crystal [1,2], several optical methods have been developed: determination of the change in reflected intensity of a laser beam that is diffracted at a lithographic grating on the wafer [3,4], reflectometry [5,6] and ellipsometry [6-10].

Each method has its own advantages and disadvantages, but only the *in situ* methods are capable of end point detection. The quartz crystal microbalance is very accurate, but is difficult to implement. The diffraction method is specifically suited for end point detection. Reflectometry is easy to implement but the refractive index of the material to be etched must be known to be able to use this method. Ellipsometry requires a computer system and special adaptations of the vacuum system to avoid unwanted contributions to the polarization of the light beam. Ellipsometry however is the only of the mentioned methods that yields accurate information on the layer thickness as well as on the refractive index of the material. Therefore it can also be used to get *in situ* information on surface processes during the etching process. The method is non–intrusive and keeps its surface–sensitive features in the hostile plasma environment, in contrast to other surface–sensitive methods like XPS and AES that necessitate an ultra high vacuum [11] (UHV). The method has been used for the

monitoring of the etching process of SiO_2 and Si films in fluorocarbon plasmas. Not only the etch rate was measured, but also the formation of reconstructed layers on top of the layers being etched were investigated. This result was obtained using a simulation model of the ellipsometric effects of a number of layers on a substrate.

4.1.2 Method

The purpose of an ellipsometer is to determine the complex ratio $\bar{\rho}$ of the intensity reflection coefficients $\bar{R}_p$ and $\bar{R}_s$ of light respectively polarized parallel (p) and perpendicularly (s) to the plane of incidence on the sample (see figure 4.1). This ratio is commonly expressed in the two real angles Ψ and Δ defined by

$$\bar{\rho} = \bar{R}_p / \bar{R}_s = \tan \Psi \exp(i\Delta). \tag{4.1}$$

The values of the ellipsometric parameters Δ and Ψ depend on the optical parameters of the surface, i.e. complex the refractive index of the substrate and the thickness and complex refractive indices of layers on the substrate. The reflection coefficients in the two directions of polarization at an interface are given by the Fresnel equations[12]. In a righthanded coordinate system these equations are given by
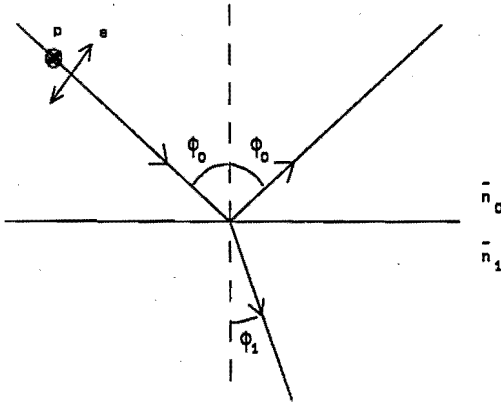

Fig. 4.1. Reflection of polarized light at a flat interface without a layer.

$$\bar{r}_p = \frac{\bar{n}_1 \cos\bar{\phi}_0 - \bar{n}_0 \cos\bar{\phi}_1}{\bar{n}_1 \cos\bar{\phi}_0 + \bar{n}_0 \cos\bar{\phi}_1},$$

$$\bar{r}_s = \frac{\bar{n}_0 \cos\bar{\phi}_0 - \bar{n}_1 \cos\bar{\phi}_1}{\bar{n}_0 \cos\bar{\phi}_0 + \bar{n}_1 \cos\bar{\phi}_1}, \tag{4.2}$$

where $\bar{n}_1$ and $\bar{n}_0$ are the complex refractive indices of the solid and the gas respectively, and $\bar{\phi}_0$ is the angle of incidence. The refracted complex angle $\bar{\phi}_1$ can be calculated from $\bar{\phi}_0$, $\bar{n}_0$ and $\bar{n}_1$ by applying Snel's law to the 01 interface[12]. If the solid is covered by a thin film (see figure 4.2) with a complex refractive index $\bar{n}_2$ and thickness d_2 the reflection coefficient ratio is given by the Drude equation[13]

$$\bar{\rho} = \left[\frac{\bar{r}_{02p} + \bar{r}_{21p} e^{-i\bar{\beta}}}{1 + \bar{r}_{02p}\bar{r}_{21p} e^{-i\bar{\beta}}} \right] / \left[\frac{\bar{r}_{02s} + \bar{r}_{21s} e^{-i\bar{\beta}}}{1 + \bar{r}_{02s}\bar{r}_{21s} e^{-i\bar{\beta}}} \right],$$

where $\bar{\beta} = \dfrac{4\pi \, d_2 \bar{n}_2 \, \cos\bar{\phi}_2}{\lambda}$, $\tag{4.3}$

and λ represents the wavelength in vacuum of the incident light and $\bar{r}_{02}$ and $\bar{r}_{21}$ the reflection coefficients at the 02 and 21 interfaces, respectively. This equation can easily
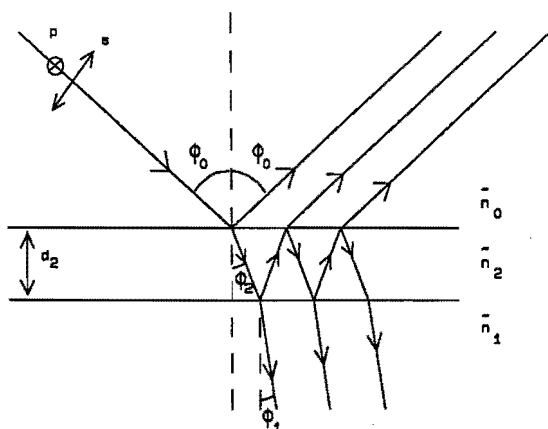

Fig. 4.2.   *Reflection and interference of light in a system with a single layer on top of a substrate.*
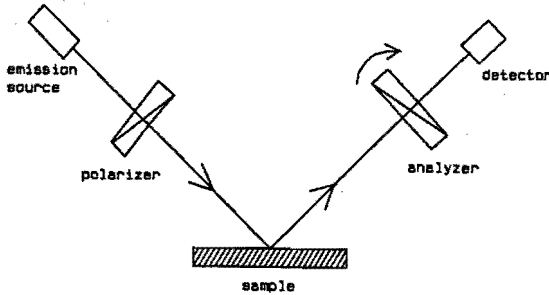
Fig. 4.3.   *Standard polarizer–sample–analyzer (PSA) configuration of a rotating*
             analyzer ellipsometer. The polarizer is set to a fixed position, whereas the
             analyzer rotates with a constant speed.

be extended to systems with many layers on top of a substrate[14]. An ellipsometer setup that is often used for the measurement of Δ and Ψ is the rotating–analyzer ellipsometer (RAE). This type of ellipsometer has been discussed extensively by Aspnes and Studna[15]. An outline of the optical setup of the ellipsometer in the standard polarizer–sample–analyzer configuration is given in figure 4.3. The light from an emission source is linearly polarized by a polarizer which is set to a fixed position. After reflection at the surface the state of polarization of the light is analyzed by a second polarizer, which rotates with a constant speed. Subsequently, the light impinges on a detector which measures the (time–dependent) intensity. In general, the intensity $I(t)$ that is measured by the detector can be described by

$$I(t) = g\,(\, a \cos 2A(t) + b \sin 2A(t) + 1 \,), \tag{4.4}$$

where

$$a = \frac{\cos 2P - \cos 2\Psi}{1 - \cos 2P \cos 2\Psi},$$

$$b = \frac{\sin 2\Psi \cos \Delta \sin 2P}{1 - \cos 2P \cos 2\Psi},$$

$$g = I_0 \, F \, (\, R_s{}^2 + R_p{}^2 \,) \, (\, 1 - \cos 2P \cos 2\Psi \,).$$

Here I_0 is the intensity of the source, F represents the transmission of the system which does not depend on the sample, P is the polarizer angle and $A(t)$ the time—dependent analyzer angle. In our case the polarizer angle P is chosen to be 45 degrees with respect to the plane of incidence and the analyzer angle A is a linear function of time, so the coefficients a and b and the angles Δ an Ψ can be obtained from Fourier analysis of the detector signal.

Before the measurement can be performed, the polarizer and analyzer angles must be calibrated. If the value of Δ for the sample is not close to $0°$ or $180°$ this can be done using the residu method[15]. For most situations where a layer is present on top of a substrate this method can be used. However, for a semiconductor surface without a layer on top of it Δ has a value around 180^0. For instance, in the case of a silicon surface and a wavelength of 632.8 nm Δ is around 177^0. In that case another calibration method, the phase calibration method[11] should be used. In addition, if Δ is around 0^0 or 180^0 the propagation of errors in the Fourier coefficients a and b into errors in Δ and Ψ is large. It is then advantageous to shift the total Δ by 90^0 with a compensator in order to get a total Δ of 90^0 or 270^0, in which case the error propagation is less[11]. In that case the ellipsometer is operated in a polarizer-compensator-sample-analyzer configuration (see
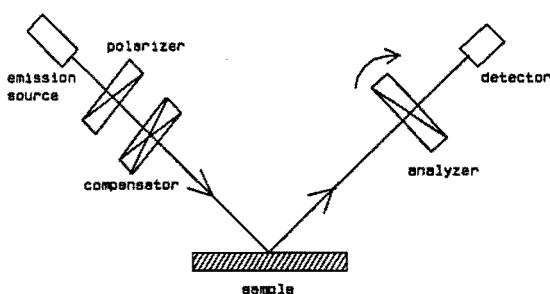

Fig. 4.4.   *Polarizer−compensator−sample−analyzer (PCSA) configuration in a*
             rotating−analyzer ellipsometer. This setup offers a smaller error-
             propagation as compared to the PSA setup if Δ is around 0^0 or 180^0.

figure 4.4). In this situation a separate calibration must be performed for the position of the optical axis of the compensator[11].

The common way to represent ellipsometric data of an evolving system is to plot the measured points in the $\Delta-\Psi$ plane. In the case of a homogeneous layer that is being etched, the shape of this curve in the $\Delta-\Psi$ plane gives information on the refractive index of that layer. The value of this parameter can be estimated using a fitting procedure. Once the refractive index is known, the etch rate can be accurately deduced from the time dependence of Δ and Ψ.

4.1.3. Experimental setup

The rotating–analyzer ellipsometer used for the experiments described in section 5.1 has only been used at only one wavelength (632.8 nm). A schematic view of the experimental setup is given in figure 4.5. The light source is a linearly polarized He–Ne laser. The light beam is circularly polarized by a quarter wave plate (to have enough light intensity at all settings of the polarizer angle). Subsequently the beam passes through the fixed polarizer. If the PCSA configuration is used the beam passes a compensator. The beam is incident on the sample at an angle of incidence of around 70⁰. This angle was measured using a geometrical method. The reflected beam passes an
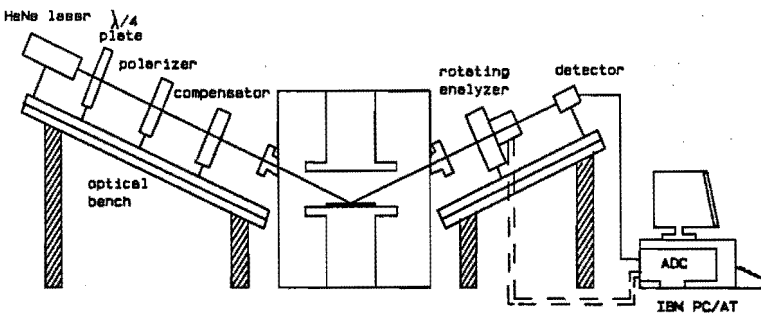

Fig. 4.5.   *Schematic view of the experimental setup of the ellipsometer. The measurement is controlled by a personal computer.*

analyzer which rotates with a frequency of 50 Hz, and then impinges on the detector, an EG&G SGD 100A pin diode. The detector signal is sampled by an Analog Devices RTI–850 16 bits A/D converter board mounted in an IBM PC/AT computer which is triggered 128 times every analyzer revolution by pulses produced by an optical encoder mounted on the analyzer. The data thus produced are processed by the computer. With this setup it is possible to measure up to 50 values of Δ and Ψ each second. The relative accuracy of Δ and Ψ is then within 0.05 degree in the region where Δ is around 90 degrees. This accuracy can be enhanced by averaging over several revolutions of the analyzer.

4.2 Infrared absorption spectroscopy

4.2.1 Introduction

A large number of diagnostics for the *in situ* measurement of neutral particle densities in RF plasmas have been developed and applied in the past. Classic passive diagnostics like optical emission spectroscopy[16] (OES), actinometry[17-20] and mass spectrometry of effusing neutrals[21,22] have been used intensively to study the neutral particle composition of etching discharges qualitatively. Recently, more quantitative particle density measurements have been developed that use active spectroscopic techniques as laser induced fluorescence (LIF)[23,24] and infrared absorption spectroscopy[25-28] for the determination of the absolute densities of radicals and process products in an active discharge. Of the two quantitative methods mentioned, LIF offers the best spatial resolution since the probe beam and the optical axis of the detector system are generally in a different direction. However, the density calibration may be difficult in the case of short living species since the LIF signal must be compared with results from an alternative technique[29]. The calibration in infrared absorption spectroscopy is easier, since for many species the absorption coefficient is either known or can be calculated from known species with a similar structure[25,30].

Several techniques are being used for infrared absorption experiments. Besides dispersive methods, interferometric methods such as Fourier Transform Spectroscopy[31] (FTS) have been developed that offer higher resolution and sensitivity. In high resolution applications the latter technique encounters a growing competition from tunable infrared diode lasers. For applications where the absorption of the species occurs over a large spectral region, FTS is advantageous since it yields the total spectrum in a single measurement. We have used FTS for the *in situ* measurement of neutral particle densities.

4.2.2 Infrared absorption spectra

The motion of molecules can be described as a combination of translation, vibration and rotation (see figure 4.6). In the case of a diatomic molecule in the harmonic oscillator approximation the solution of the Schrodinger equation for a vibrating molecule has eigenvalues E_v for the vibrational energy as given by[32]

$$E_v = \frac{h}{2\pi} \left[\frac{f}{\mu} \right]^{0.5} (v + \tfrac{1}{2}) = h\nu_0(v + \tfrac{1}{2}) , \qquad (4.5)$$

where v is the quantum number for vibration, μ is the reduced mass, h is Planck's constant and f is the force constant of the bond. If the rotation of the molecule is approximated by that of a rigid rotor, the eigenvalues E_r for the solution of the Schrodinger equation for the rotation of the molecule are given by.[32]

$$E_r = \frac{h^2}{8\pi^2 I} \, J \, (J+1) \qquad (4.6)$$

where I is the moment of inertia of the molecule perpendicular to the main symmetry axis, and J is the rotational quantum number. Absorption of infrared radiation can
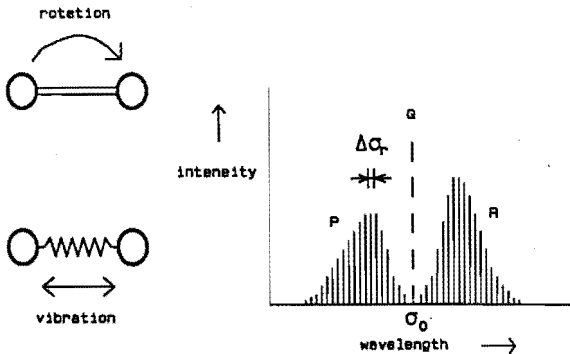

Fig. 4.6   Vibration and rotation of molecules. Changes in the vibrational and rotational energy of a molecule can be induced by the absorption of infrared radiation.

induce transitions between the energy levels given in (4.5) and (4.6). The energy of the photons that are absorbed is equal to the energy difference ΔE of the levels between which the transition occurs (not considering electronical transitions),

$$\Delta E = h\nu_0 + \frac{h^2}{4\pi^2 I}\,\Delta J \cdot (J+1)\ , \qquad\qquad (4.7)$$

where $\Delta J = 0, \pm 1$. The possible transitions are dictated by selection rules[33]. In the case of a diatomic molecule with a Σ ground state only transitions with $\Delta J = \pm 1$ are allowed. In molecules containing more than two atoms the expressions for the levels are more complicated and depend on the symmetry of the molecule[33]. In these cases also transitions can occur with $\Delta J = 0$. The total of transitions with $\Delta J = -1, 0, +1$ are generally referred to as P, Q and R branches, respectively (see figure 4.6). An infrared band is therefore a combination of a vibrational transition with a superimposed fine structure of rotational transitions. The width of the individual absorption lines is determined by several broadening mechanisms, Doppler broadening being the most important in the pressures range concerned. The line width is for all particles concerned around $5 \cdot 10^{-3}$ cm^{-1}. This is well below the experimental resolution, and therefore the absorption is only proportional to the density of the species for small absorptions[34]. Since the transition normally starts from the ground state level, the method can directly yield ground state densities and can therefore be used quantitatively. The intensity after absorption can be described by Beer's law

$$I(\sigma) = I_0(\sigma)\exp(-k(\sigma)\cdot n \cdot l)\ . \qquad\qquad (4.8)$$

Here $\sigma\ (=1/\lambda)$ is the wave number, $I_0(\sigma)$ the intensity of the emission source, $k(\sigma)$ the molar absorption coefficient, n the molar density of the absorbing species and l the length of the absorption path. The absorbance is defined as

$$\text{Abs}(\sigma) = \ln\left[\frac{I_0(\sigma)}{I(\sigma)}\right] = k(\sigma)\cdot n \cdot l\ . \qquad\qquad (4.9)$$

Since the shape of the spectrum depends on the distribution of the species over the rotational levels, only a measurement of the integrated absorbance yields the absolute density. The relation between the integrated absorbance and the density of the species n is given by

$$n = \frac{1}{A\cdot l}\int_{\text{band}} \text{Abs}(\sigma)\,\mathrm{d}\sigma\ , \qquad\qquad (4.10)$$

where A ($= \int k(\sigma)\, d\sigma$) is the integrated molar absorption coefficient. The value of A for most stable species is known in the literature or can easily be determined by a measurement of the integrated absorbance at a known partial pressure of the species. For radicals one has to rely on calculations which are based on molecules with a similar symmetry[25,30] and which are accurate within 10–20 %.

4.2.3 Principles of Fourier Transform Spectroscopy

In dispersive spectroscopy the separation of the individual wavelengths is achieved by a spatial separation and consecutive measurement at each wavelength. In Fourier Transform Spectroscopy the spectral separation is performed by modulating each wavelength by a different frequency and Fourier transforming the result. In practice this is achieved by an interferometer setup, and in many cases the Michelson interferometer has been used for this purpose[31]. The basic setup of this interferometer is depicted in figure 4.7. Radiation from a broadband emission source is divided into two beams by a beamsplitter. One of these beams is reflected at a flat mirror that is present at a fixed position from the beamsplitter. The other beam is reflected at a mirror that is continuously moving. The two beams interfere with each other at the detector. For an absorption experiment the two beams are directed through an absorption cell between the beamsplitter and the detector. For a Michelson interferometer, the interference of monochromatic radiation of wave number σ with a spectral intensity $I_0(\sigma)$ at an optical
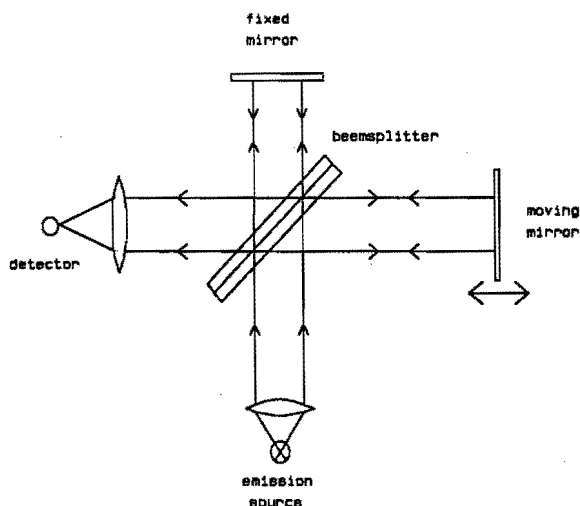

Fig. 4.7   *Principle of operation of a Michelson interferometer.*

pathlength difference x is described by

$$I(x,\sigma) = \tfrac{1}{2} I_0(\sigma) \left[1 + \cos(2\pi\sigma x) \right] . \tag{4.11}$$

The varying part of the total intensity of the interference pattern of the broadband source is therefore given by

$$I(x) = \tfrac{1}{2} \int\limits_{0}^{\infty} I_0(\sigma)\cos(2\pi\sigma x)\mathrm{d}\sigma = \int\limits_{-\infty}^{\infty} B(\sigma)\exp(2\pi i \sigma x)\mathrm{d}\sigma , \tag{4.12}$$

where $B(\sigma) = \tfrac{1}{4} I_0(\sigma)$. From (4.12) it can be clearly seen that the maximum intensity will occur at $x{=}0$. The varying part of the intensity pattern is thus the Fourier transform of the power spectrum, and therefore the power spectrum $B(\sigma)$ is given by the inverse Fourier transform of the interferogram $I(x)$,

$$B(\sigma) = \frac{1}{2\pi} \int\limits_{-\infty}^{\infty} I(x)\exp(-2\pi i \sigma x)\mathrm{d}x . \tag{4.13}$$

In practice, we can of course only measure $I(x)$ over a limited interval. The length L of this interval determines the resolution $\Delta\sigma$ of the measurement[31] by $\Delta\sigma \approx 1/L$. Since $B(\sigma)$ is a real number, $I(x) = I(-x)$. This means that in the ideal case we do not need to measure $I(x)$ on both sides of $x{=}0$. However, in a realistic interferometer $I(x)$ is in most cases asymmetric, due to zero–path errors and dispersion, mainly in the beamsplitter. (see figure 4.8). This asymmetry can be corrected by a phase correction procedure[35]. For this procedure a small double–sided interval around $x{=}0$ is sampled. From this double–sided interval the broadband features of the dispersion and zero–path errors are calculated and this information is used to correct the one–sided interferogram, restoring the symmetry almost completely (see figure 4.9). Subsequently only one side of $I(x)$ needs to be measured, thus saving measurement time or increasing the resolution.

4.2.4 Experimental setup

The Fourier Transform Spectrometer that has been developed for the measurement of the densities of neutral species in the plasma has been schematically depicted in figure 4.10. It consists of three Michelson interferometers that have one
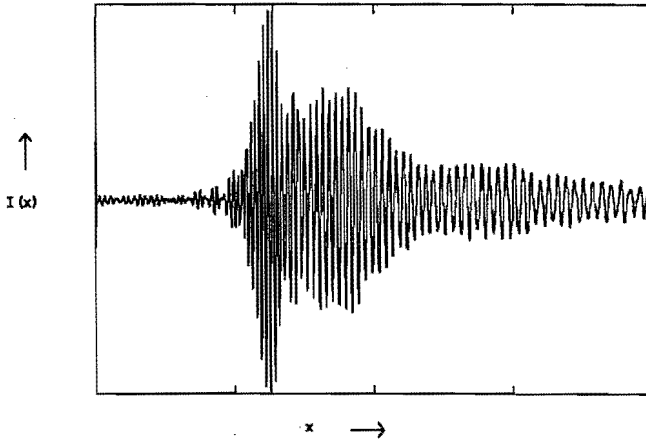
Fig. 4.8   *Example of the centerburst of a measured interferogram before phase correction. The asymmetry is mainly caused by dispersion in the beamsplitter.*
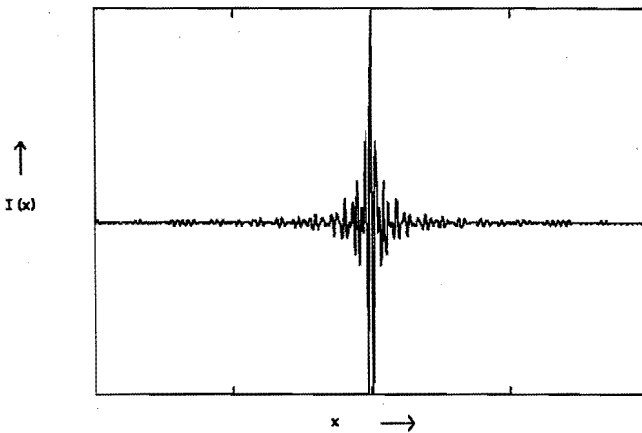
Fig. 4.9   *Example of the centerburst of a measured interferogram after phase correction. The asymmetry is almost completely removed.*
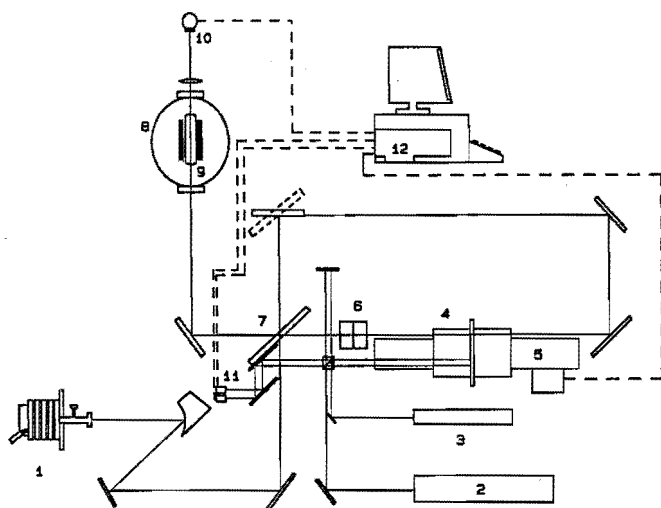
Fig. 4.10   *Experimental setup of the Fourier Transform Spectrometer that has been*
used for the measurement of infrared absorption spectra. For high
resolution applications both arms of the infrared interferometer can be
varied.

1   – Cascaded Ar arc (light source)

2   – He–Ne laser

3   – White light halogen lamp

4   – Moving mirror (driven by a stepper motor)

5   – Air bearing

6   – Periscope system (to enlarge the optical path length)

7   – Beamsplitter

8   – Vacuum vessel

9   – 13.56 MHz RF plasma

10 – MCT–detector

11 – detectors for the laser– and white light interferometers

12 – PC/AT with a 16–bit AD–converter board

common part – the moving mirror. The position of the moving mirror is varied by
pulling the mirror over an air bearing using a computer–controlled stepping motor. One
of the interferometers produces the interferogram of the infrared light, whereas the two
others produce start– and trigger–pulses for the synchronization of the measurement.

The start of the measurement is determined by a white light interferometer. Due to the broadband spectrum of its white light emission source (a halogen lamp) this interferometer produces a narrow intensity spike at the position of the moving mirror where the optical pathlength difference of the white light interferometer is zero. The position of the fixed mirror is set such that the white light intensity spike is generated just ahead of the centerburst of the infrared interferometer, to be able to sample a small double—sided part of the interferogram, needed to correct the interferogram asymmetry. Trigger pulses at equidistant positions are generated by a laser interferometer based on a frequency stabilized He—Ne laser[36]. Since the laser light is monochromatic, the laser interferometer signal can be described by (4.11). Hence, the a.c. part of the laser interferometer signal crosses zero at positions of the moving mirror that are $\frac{1}{4}\lambda$ apart. The zero—crossing of this signal has therefore been used to trigger the measurement.

For the emission source of the infrared interferometer a cascaded arc[37] is used. In the wavelength region of interest for this study (5—10 μm) this source acts as an almost ideal Planck radiator with a temperature of 13000 K. The brightness of this source is high as compared to conventional emission sources such as Globars that are normally operated at $\approx$ 1500 K. A parallel beam of the radiation of the cascaded arc is produced by an off—axis paraboloid mirror. The other mirrors of the infrared interferometer including the moving mirror are made of gold—coated glass, whereas in the two other interferometers aluminum—coated mirrors have been applied. In the infrared interferometer a wedged ZnSe beamsplitter is used to minimize parasitic reflections inside the beamsplitter that can give rise to a disturbing modulation of the spectrum[32]. In some high—resolution measurements a somewhat modified setup has been used, in which both arms of the infrared interferometer are varied (see figure 4.10). This method also offers a passive compensation for tilting of the moving mirror[38]. The infrared beam is let in and out of the vacuum system through two wedged BaF_2 windows. The interferogram of the infrared light is measured with a photovoltaic HgCdTe detector cooled at 77 K by liquid nitrogen. The signal of the detector is a.c. amplified and filtered (to reduce 'aliasing' [39]) and sampled by an Analog Devices RTI—850 16—bits A/D—converter board mounted in an IBM PC/AT. The maximum resolution of the measurement is limited by the length of the air bearing ($\approx$ 40 cm) and the number of measurement points that can be stored in the A/D board memory (256k). The maximum resolution possible with this setup is at present 0.015 cm⁻¹. The measurement and data handling are controlled by a program in Borland Turbo Pascal 4.0. The complete optical setup is mounted on a vibrationally isolated granite plate to ensure the stability of the optical setup. The 4 m² granite plate surrounds the plasma reactor. In figure 2.2 the situation is outlined. Furthermore the whole setup is flushed by dry air

provided by a Balston air drying system to reduce dust formation and water absorption in the spectrometer.

To enhance the absorption signal of the plasma in some experiments a multi–pass mirror system has been applied. A schematic view of this system is given in figure 4.11. The mirrors in this system are also made of gold coated glass.

4.2.5 Data handling

In order to improve the signal–to–noise ratio in most cases several interferograms were block averaged. To prevent jitter in the white light spike from propagating in the resulting interferogram, a correlation procedure was used to check that the centerburst of the interferogram was at a constant position in the data–array. To reduce the effects of possible instabilities of the spectrometer, the plasma was gated by the computer program and alternate measurements with and without plasma were averaged separately. After the measurement, the spectra were calculated using an FFT procedure[39,40]. For single–sided high–resolution spectra an $N/4$ algorithm[41] was used to reduce the calculation time. In most cases prior to the transformation the interferogram was multiplied by an apodization function $F(x)$

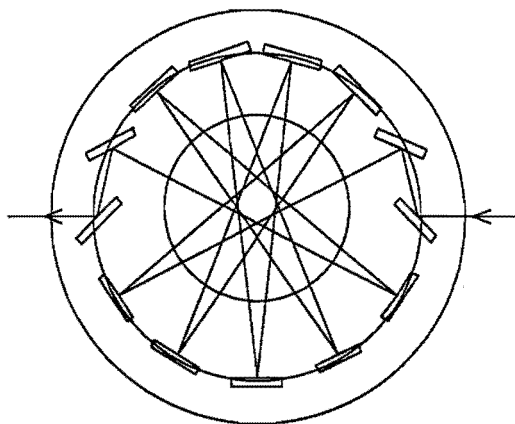$$F(x) = \left[1 - \left[\frac{2x}{L} \right]^2 \right]^2 \tag{4.14}$$

Fig. 4.11   *Schematic view of the multi–pass optical system that has been used to increase the absorption signal from the plasma.*

to improve the spectral profile of the apparatus. All these calculation were performed on an IBM 6150 RT PC. For low–resolution double–sided spectra a standard complex FFT was applied and this calculation was performed on the measurement computer itself.

4.3 Microwave resonance

4.3.1 Introduction

The chemically active plasmas studied in this work are generated by energetic electrons which create reactive particles by ionization, dissociation and excitation. Therefore knowledge of the density and energy distribution of these electrons is needed for a fundamental understanding of the processes taking place in the plasma. To measure these parameters, several methods have been developed in the past. Electrostatic (Langmuir) probes[42] have been widely used to measure both the electron density n_e, the electron temperature[43] T_e, and the space potential[44]. This technique has many advantages, since it offers a relatively simple measurement and can be performed as a function of the probe position in the plasma. However, in RF plasmas the potential difference between plasma and probe contains an RF component, which makes the interpretation of the DC probe characteristic questionable if complicated compensation techniques[45] are not applied. Furthermore the modification of the probe surface itself in a chemically active plasma can cause some problems[46]. Finally in electronegative plasmas the influence of negative ions on the probe characteristic should be taken into account[47-48], which further complicates the interpretation.

Alternative methods for the measurement of n_e are microwave methods[49-53]. The main advantages of these methods are that they are non–intrusive, sensitive, and they can be used with a temporal resolution of less than a microsecond. A disadvantage is that their spatial resolution usually is poor. To evaluate the electron density in our system, the plasma was produced in the cavity geometry. The shift of the resonance frequency of the cavity caused by the RF plasma is a measure of the electron density in the cavity.

For the observation of positive ions in an RF discharge both probe methods[54] and mass spectrometry[55] of effusing ions have been used. With the first technique the compensation of the RF component in the probe current and effects due to the presence of negative ions again make the analysis difficult, whereas with the latter it is difficult to translate measured ion currents to ion densities in the plasma. To obtain results for negative ions is an even more difficult task. The reason for this is that negative ions are trapped in the glow region of the plasma as a result of the potential difference between

the glow and the electrodes. This makes it difficult to measure negative ion densities *in situ* without disturbing the plasma severely. As an example, measurements using mass spectrometry can only be done in the afterglow of the plasma[56]. At the time the ions are detected, the composition of the plasma is totally different from the undisturbed situation. Hence, it is difficult to obtain quantitative results.

Gottscho and Gaebe[57] introduced an alternate method to detect negative ions by applying photons to transform the negative ions into electrons and neutrals by photodetachment and subsequently detect the increase of the electron density by an opto–galvanic method. Although this is an indirect method, it is well possible to detect negative ions this way. In our setup we use the microwave cavity method to detect the released electrons. In this way quantitative measurements can be performed relatively easily.

4.3.2 Microwave cavity method

The electromagnetic field of the standing waves inside a cavity can be described as a linear combination of the various resonant modes of the cavity, each with its own characteristic frequency. Since the resonant microwave wavelength is dictated by the cavity dimensions, and the dielectric constant decreases with the electron density, the presence of a plasma in the cavity will increase the frequency of each mode. An example
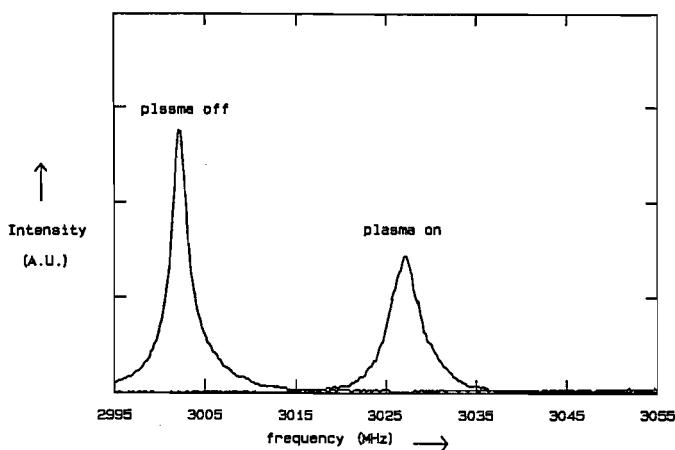

Fig. 4.12   *Example of the shift of the resonance curve when a plasma is created in the cavity volume.*

of this is given in figure 4.12 where the shift of the resonance curve can be seen clearly. We can calculate the change of the resonance frequency and the change of the quality factor[58] Q of the cavity as a function of the spatial electron density profile $n_e(\vec{r})$ to be respectively[59]

$$\frac{f'}{f_0} = \frac{1}{2} \frac{\iiint\limits_{\vec{r}} \frac{n_e(\vec{r})\ e^2}{m_e \epsilon_0 \omega^2} \frac{1}{1+(\nu_m/\omega^2)} \ E^2 \ d^3\vec{r}}{\iiint\limits_{\vec{r}} E^2 \ d^3\vec{r}} , \qquad (4.15)$$

and

$$\frac{1}{Q} - \frac{1}{Q_0} = \frac{\iiint\limits_{\vec{r}} \frac{\nu_m}{\omega} \frac{n_e(\vec{r})e^2}{m_e\epsilon_0\omega^2} \frac{1}{1+(\nu_m/\omega)^2} \ E^2 \ d^3\vec{r}}{\iiint\limits_{\vec{r}} E^2 \ d^3\vec{r}} , \qquad (4.16)$$

where f and f_0 are the resonance frequency of the cavity respectively with and without plasma, $f' = f - f_0$ and Q_0 the quality factor of the cavity without plasma. The integrations run over the entire cavity volume. We can see from (4.15) and (4.16) that in order to use this method effectively we need information about the spatial electron density profile. If we assume that the electron density profile has cylindrical symmetry and the r and z dependencies can be separated, n_e can be written as $n_e = n_{e0} \ f(r) \ g(z)$ where r and z are the radial and axial coordinates and n_{e0} is the electron density in the center ($r=0$, $z=0$) of the discharge. In that case f(0) = g(0) = 1. If this is combined with (4.15) and (4.16), using that $\nu_m^2 << \omega^2$ (this can be calculated from $1/Q-1/Q_0$ and is true for all experimental conditions in this study), we can derive that

$$n_{e0} = \frac{2f' \ m_e \ \epsilon_0 \ \omega^2}{f_0 \ e^2} \cdot A , \qquad (4.17)$$

where A is

$$A = \left[\frac{\iint\limits_{rz} E^2 \ f(r) \ g(z) \ 2\pi r \ dr \ dz}{\iint\limits_{rz} E^2 \ 2\pi r \ dr \ dz} \right]^{-1} .$$

This linear dependence between n_{e0} and f is only valid for small f/f_0. Using a somewhat different approach Persson[60] has derived that this dependence is valid for $n_e < 5 \cdot 10^{16}$ m^{-3} at $f_0 = 3$ GHz. This is valid for all measurements in this study. The factor A in (4.17) contains the integrated spatial dependence of the electron density and of the electric field strength. This term may be interpreted as a correction factor[61,62] and can be calculated by a numerical integration if f(r) and g(z) are known.

Estimates for f(r) and g(z) were obtained using spatially resolved emission spectroscopy. We have determined the spatial distribution of the electrons by adding a small amount (≤ 5 %) of Ar to the plasma and measuring the 4s[3/2]^0 $-$ 5p[1/2] line of Ar at 419.8 nm. For this emission intensity to be proportional to the electron density this transition must be in corona equilibrium and T_e must be constant over the volume. This means that the total rate for collisional deexcitation from the 4s level

$$dn^i_{cd}/dt = -n^0 \cdot n^i \cdot k_{dn} + n_e \cdot n^i \cdot k_{de} , \qquad (4.18)$$

(where k_{dn} is the coefficient for collisional de–excitation by neutrals, k_{de} the coefficient for collisional de–excitation by electrons, n^0 the bulk gas density and n^i the density of Ar atoms in the 4s level) must be much smaller than the rate for radiative de–excitation

$$dn^i_{rd}/dt = -n^i \sum_j A_{ij} , \qquad (4.19)$$

where A_{ij} are the transition probabilities of possible emission lines from the 4s level. If this is so, the emission intensity I is given by

$$I = n_e \cdot n^0 \cdot k_{exc} \cdot h\nu \cdot A_{ij} / \sum_j A_{ij}, \qquad (4.20)$$

where k_{exc} is the excitation coefficient. For the 419.8 nm Ar line $A_{ij} = 2.8 \cdot 10^6$ s^{-1}. The major process for collisional de–excitation is collision with neutrals, since the electron density is 5–6 orders of magnitude lower than the neutral gas density. The value for k_{dn} is given by $k_{dn} = \sigma_{dn} \cdot v_{th}$ where v_{th} is the thermal speed of the neutrals and σ_{dn} is the cross–section for collisional deexcitation by neutrals. This cross–section has been estimated from the van der Waals radius of Ar. The result of this is that collisional deexcitation is about two orders of magnitude slower than radiative deexcitation. The emission intensity is therefore directly proportional to the electron density and can be used to determine f(r) and g(z). Since k_{exc} is a function of T_e, it is implicitly assumed that the electron temperature is not strongly dependent on the position in the plasma. The latter is more or less true in the glow region of the plasma, but may not be true in

the sheath region. However, since no accurate data are available on the spatial dependence of T_e, this has not been accounted for. This may lead to some overestimation of n_e in the sheath region.

In this work for the microwave field only the TM_{020} mode has been used and the cavity was optimized for this mode[16]. The electric field distribution of the TM_{020} mode is given by

$$E_z = E_0 \, J_0(j_{02}r/R)$$

$$E_x = E_y = 0 \tag{4.21}$$

where J_0 is the zero order Bessel function, j_{02} its second zero and R the radius of the cavity. The electric field depends therefore only on the radial position and the integration in (4.15) can be easily separated.

Integration of practical emission profiles weighed over the microwave field yield that the value of the factor A in (4.17) varies between unity and 1.8, depending mostly on the gas pressure applied. Since the radial contribution to A is small, this is roughly equal to the ratio of the average— and maximum value of n_e in the volume.

4.3.3. Detection of negative ions

Microwave cavity resonance spectroscopy is a very sensitive method (the detection limit is $\approx 2 \cdot 10^{11}$ m^{-3}) to determine electron densities *in situ* and non–intrusive. However, this method only detects charged particles that have a mobility high enough to follow the microwave field. Therefore, for practical frequencies around a few GHz, only electrons are detected by this method. In order to use it for the determination of negative ion densities, the negative ions are to be transformed into electrons and neutrals using a laser induced photodetachment process

$$X^- + h\nu \longrightarrow X + e^- , \tag{4.22}$$

where X^- is an arbitrary negative ion. In practice this means that a short laser pulse is fired through the plasma. A number of electrons is then released by the photodetachment effect. After this, both the electron density and the negative ion density decay to the original equilibrium values. If the electron density is monitored as a function of time, a jump in the electron density is observed shortly after the laser is fired. This density jump depends on the fraction of the negative ions which is eliminated

by photodetachment. If all negative ions in the irradiated volume are detached, the effect saturates. This saturation was checked by performing the experiment as a function of the laser pulse energy[63]. In saturation the height of the jump can be easily related to the average number of negative ions within the volume of the laser beam. In a preliminary paper[63], two ways to operate the experiment have been discussed. In the first method the laser pulse travels only once through the plasma. This method offers an easy interpretation of the results. In the second method the laser beam reflects several times inside the cavity, and therefore this method offers a higher signal level. However, in the latter case the interpretation is more difficult. For the experiments described in this work the single pass method has been applied.

The extra electrons produced by the photodetachment process also induce a change in the resonance frequency, which can be described by (4.15). However, since the extra electrons are only produced in the irradiated volume, in the numerator of (4.15) the integration only runs over that volume. If we assume that the extra electron density Δn_e is constant over the volume of the laser beam, the expression for the frequency shift $\Delta f'$, just after the laser pulse, caused by the extra electrons reduces to

$$\frac{\Delta f'}{f_0} = \frac{1}{2} \frac{\dfrac{\Delta n_e \ e^2}{m_e \epsilon_0 \omega^2} \cdot \dfrac{O}{1+(\nu_m^2/\omega^2)} \displaystyle\int_{-R}^{R} E^2 \ dr}{\displaystyle\iiint_{cavity} E^2 \ d^3\vec{r}}, \qquad (4.22)$$

where R is the radius of the cavity and O is the area of the laser beam. The diameter of the laser beam is small as compared to the radius of the cavity. From this expression Δn_e can be calculated if the frequency shift f' is already known. This can be achieved by measuring some data points before the laser is fired. Provided that the photodetachment effect is completely in saturation, Δn_e is directly the negative ion density in the volume of the laser beam. If the negative ion density is not constant over the volume of the laser beam, a small correction of about 10–20 % must be performed, similar to the measurement of the electron density. Because we have no information on the spatial dependence of the negative ion density in the radial direction of the cavity, no such correction was performed. Since the method only releases electrons in the irradiated volume, it is possible to get spatially resolved negative ion densities in the axial direction of the cavity by varying the position of the laser beam.
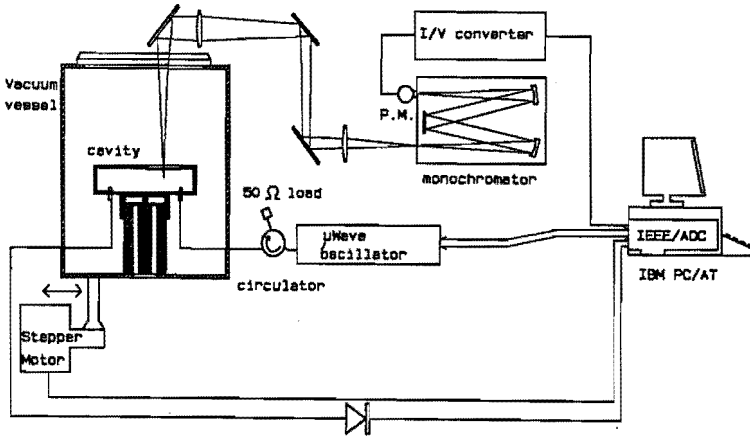
Fig. 4.13   *Experimental setup for the measurement of electron densities in the*
               cavity.

4.3.4 Experimental setup for the n_e measurement

The experimental setup used for the electron density measurement is depicted in figure 4.13. To make sure that the microwave field is not distorted too much at the gap between the RF and grounded part of the cavity, the radius of the RF electrode coincides with the maximum between the first and second zero of the TM_{020} mode where no surface currents are present, and $\lambda/4$ slots are present in the space beneath the gap[16]. The microwave power, supplied by a Gigatronics Model 605 generator, is coupled in and out the cavity by two small loops which are situated close to the edge of the cavity. The microwave power used (typ. ≤ 1 mW) was in all cases negligible as compared to the RF power. Since we used a cavity with a diameter of 175 mm and a height of 20 mm, the TM_{020} mode that has been used has its resonance frequency at about 3.002 GHz without plasma. The position of the resonance frequency is determined by stepping the microwave frequency and measuring the transmitted signal using an Analog Devices RTI–850 A/D converter, controlled by a computer program in Borland Turbo Pascal 4.0, which also calculates the electron densities from the measured frequency shifts and optical emission data.

The optical emission profiles used for the correction of the electron densities were determined by scanning the whole vacuum vessel in both axial and radial directions. The

optical system for the radial scans has been depicted in figure 4.13. To minimize the microwave loss through the emission ports in radial and axial directions, the ports were covered with a mesh. To avoid flow through the upper part of the cavity, directly above the mesh in the port for the radial emission scans a quartz window was mounted. The spatial resolution was about 2 mm in the radial direction, and about 1 mm in the axial direction. The emission intensity is measured by a Jobin–Yvon HRS 2 monochromator and a photomultiplier. The signal voltage is again measured by the A/D converter. Typical emission profiles for a CF_4 plasma in the radial and axial directions are depicted in figures 4.14 and 4.15. Since the spatial profiles are in (4.15) and (4.16) weighed by the electric field distribution of the TM_{020} mode, the spatial distribution of this mode in the radial direction has also been given in figure 4.14. The electric field is constant over the axial direction. The correction factor A in (4.17) for all conditions investigated was calculated from the optical emission profiles by a numerical integration (using Simpson's rule) of the profiles with the TM_{020} field distribution in the cavity.

4.3.5. Experimental setup for the n^- measurement

Large parts of this experimental setup have already been described in the previous section. Therefore only a brief description will be given of the features which are specific for this experiment. A schematic view of the experimental setup is given in
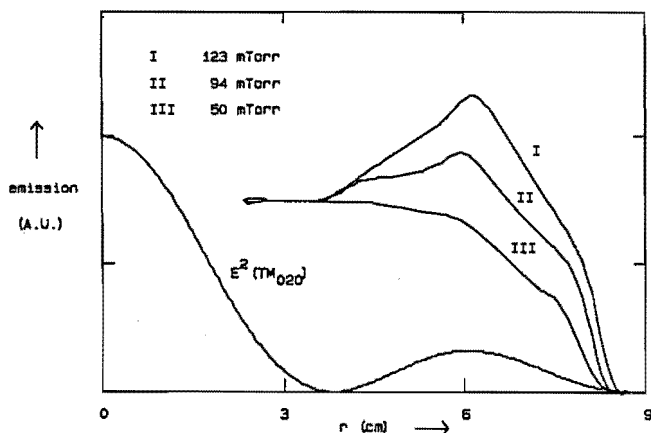

Fig. 4.14   *Relative radial emission profiles of the 419.8 4s–5p Ar line in plasmas produced in CF_4 (with a small amount of Ar) and the square of the electric field strength of the TM_{020} mode. Parameter is the gas pressure. The radial profile is weighed with the square of the electric field strength.*
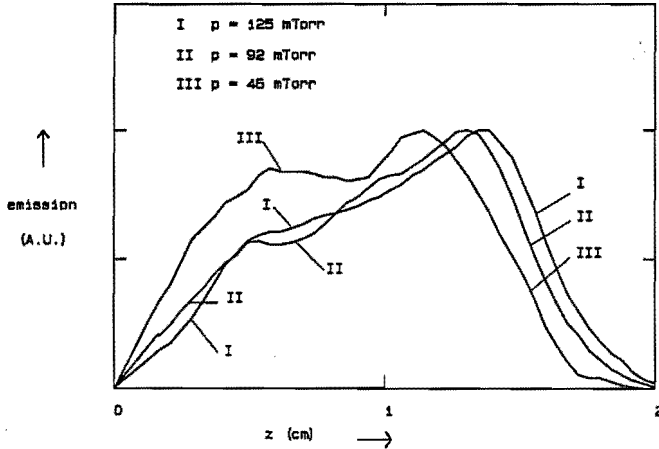
Fig. 4.15   *Relative axial emission profiles in plasmas produced in* CF_4. *Parameter is the gas pressure. The microwave electric field is constant in the axial direction. The grounded electrode is located at z=0.*

figure 4.16.

A frequency quadrupled Spectra Physics DCR–11 Nd–YAG laser at 266 nm with a 2 ns pulse length and 10 Hz repetition frequency is used for the absolute negative ion density measurements. The laser beam enters the vacuum system through quartz windows. The microwave cavity has two slits to allow the laser beam to pass through the plasma. After exiting the vacuum system, the beam is dumped. All wavelengths of the laser (1ω, 2ω and 4ω) are directed coaxially, but only the 4ω beam produces any photodetachment effect in the gases investigated. After passing the vacuum system the 4ω beam is separated from the 1ω and 2ω beams by a Pellin–Broca prism. The intensity is calibrated with a laser power meter. To avoid scattering of the laser beam at the walls of the cavity, the beam diameter was kept smaller than the width of the slits of the cavity using a diaphragm. This diaphragm furthermore ensures that the effect saturates in the entire laser beam volume. For wavelength–dependent measurements the 2ω beam of the Nd–YAG laser was used to pump a Spectra Physics PDL–3 dye laser. For the latter an LDS 750 dye was used around 720 nm. The output of the dye laser was again frequency doubled to obtain wavelengths around 360 nm.

Preliminary results of time–dependent measurements of the transmitted microwave signal at a fixed microwave frequency[52,63] showed that a considerable
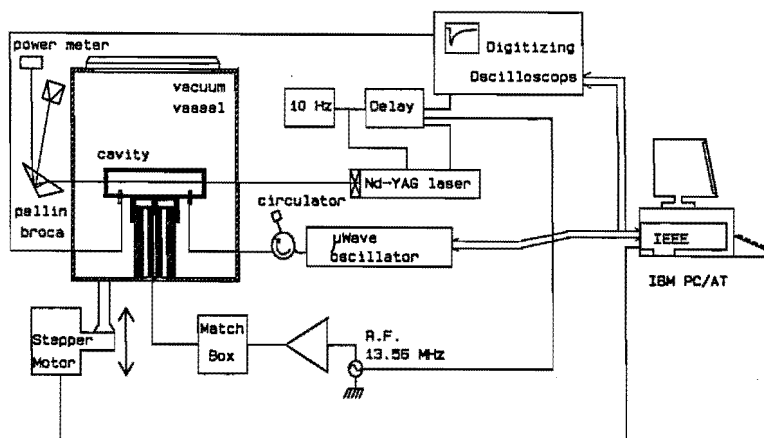
Fig. 4.16   *Schematic view of the experimental setup that has been used for the measurement of negative ion densities. For wavelength−dependent measurements of the amount of photo−electrons released by the photodetachment process a frequency doubled dye laser was used instead of the frequency quadrupled Nd−YAG laser.*

increase of the electron density is observed after firing the laser beam through the plasma. However, for a correct interpretation of the data as described in the previous chapter it is necessary to know the resonance curve as a function of time to be able to calculate the extra shift caused by the photodetachment process. This is done by measuring the microwave signal as a function of time using a HP 54111D digitizing oscilloscope. The oscilloscope is controlled by a IBM PC/AT using an IEEE−488 connection. The microwave generator frequency is also controlled in this way. The time−dependent signal was measured for a large number of microwave frequencies. Several shots (typ. 20) were averaged. In this way a matrix is obtained of the transmitted microwave signal as a function of time and of microwave frequency. Although the measurements are taken in the time direction, the analysis is performed in the microwave frequency direction, searching the maximum in the resonance curve at a given time. In a 3D−plot of this matrix the shift in the resonance curve can be easily recognized (see figure 4.17). The resonance frequency at each temporal point was calculated from the measurement data by fitting a second−order polynomial to the top of the curve using a least−squares procedure. As a result of the automation and of the fitting procedure, it is now possible to detect negative ion densities of less than 10^{14} m^{-3},
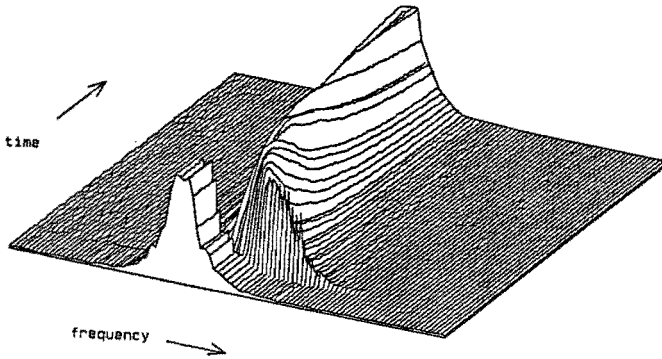
Fig. 4.17   *3D-plot of the transmitted microwave signal as a function of time and microwave frequency just after a laser beam is fired through the plasma. The resonance frequency is shifted due to the photo-induced production of extra electrons.*

an improvement of about a factor of ten as compared to preliminary measurements at a single microwave frequency[52,63]. The response time τ of the measurement is determined by the quality factor Q of the cavity : $\tau = \frac{Q}{\pi f}$. For a quantitative evaluation of Δn_e it is necessary that this response time is smaller than the time constant of the decay of Δn_e after the laser pulse. In most cases the standard quality factor Q (2300) corresponding to a time constant of about 240 ns, sufficed. In C_2F_6 and C_3F_8 plasmas the quality factor of the cavity had to be decreased, by re-positioning the microwave antennas, to $Q \approx 500$ and a response time of about 53 ns.

Experiments on the time dependence of negative ion densities in the afterglow of the plasma have been done by using a time delay circuit and by gating the RF generator. Since in the late afterglow the electron density is almost zero, the extra electron density can in that situation be inferred from a measurement at a fixed frequency, thus saving measurement time. The relation between the intensity jump and the electron density jump at a fixed frequency can be calibrated by performing one of the measurements in the usual way (at several frequencies).

References

1   A.R. Nyaiesh and M.A. Baker, *Vacuum* **32**, 305 (1982).

2   J.W. Coburn, H.F. Winters and T.J. Chuang, *J. Appl. Phys.* **48**, 3532 (1977).

3   E.S. Braga, G.F. Mendes, J. Frejlich and A.P. Mammana,
     Thin Solid Films **109**, 363 (1983).

4   H.P. Kleinknecht and H. Meier, *J. Electrochem. Soc.* **125**, 61 (1978).

5   H.H. Busta, R.E. Lajos and D.A. Kiewit, *Sol. State Techn.* **22**, 61 (1979).

6   S. Gourrier, *Acta Electronica* 24, 229 (1981/1982).

7   C.M. Horwitz, *J. Vac. Sci. Techn.* B1, 840 (1983).

8   J.L. Buckner, D.J. Vitkavage, E.A. Irene and T.M. Mayer,
     J. Electrochem. Soc. **133**, 1729 (1986).

9   R.W. Collins, *Appl. Phys. Lett.* **52**, 2025 (1988).

10   G.S. Oehrlein, I. Reimanis and Y.H. Lee, *Thin Solid Films*, **143**, 269 (1986).

11   J.M.M. de Nijs, *Ellipsometry and the Ti/c−Si solid state reaction*,
     Ph.D. thesis, (Enschede 1989).

12   M. Born and E. Wolf, *Principles of optics*, (Pergamon Press, Oxford, 1980).

13   R.M.A. Azzam and N.M. Bashara, *Ellipsometry and Polarized light*,
     (North Holland, Amsterdam 1977).

14   G.M.W. Kroesen, *Plasma deposition, investigations on a new approach*,
     Ph.D. thesis (Eindhoven 1988).

15   D.E. Aspnes and A.A. Studna, *Applied Optics* **14**, 220 (1975).

16   T.H.J. Bisschops, *Investigations on an RF−plasma related to plasma etching*,
     Ph.D. thesis (Eindhoven 1987)

17   J.W. Coburn, M. Chen, *J. Vac. Sci. Techn.* **18**(2), 353 (1981).

18   J.W. Coburn, M. Chen, *J. Appl. Phys.* **51**, 3134 (1980).

19   R. d'Agostino, F. Cramarossa, S. De Benedictis, G. Ferraro,
     J. Appl. Phys. **52**, 1259 (1981).

20   R. d'Agostino, V. Colaprico, F. Cramarossa,
     Plasma Chem. Plasma Proc. 1, 365 (1981).

21   G. Smolinsky, D.L. Flamm, *J. Appl. Phys.* **50**, 4982 (1979).

22   K.R. Ryan, I.C. Plumb, *Plasma Chem. Plasma Proc.* **4**, 271 (1984).

23   J.P. Booth, G. Hancock, N.D. Perry, *Appl. Phys. Lett.* **50**, 318 (1987).

24   J.P. Booth, G. Hancock, N.D. Perry, M.J. Toogood,
     J. Appl. Phys. **66**(11), 5251 (1989).

25   E.M. van Veldhuizen, T.H.J. Bisschops, E.J.W. van Vliembergen,
     J.H.M.C. van Wolput, *J. Vac. Sci. Techn.* A3(6), 2205 (1985).

26   H.U. Poll, D. Hinze, H. Schlemm, *Appl. Spectr.* 36(4), 445 (1982).

27   J. Nishizawa, N. Hayasaka, *Thin Solid Films* 92, 189 (1982).

28   M. Magane, N. Itabashi, N. Nishiwaki, T. Goto, *Proc. 7ᵗʰ Symp. on Plasma Proc.*, Tokyo, 25–26 Jan. 1990, pp. 181.

29   D. Manos, A. Fontijn, *J. Chem. Phys.* 72, 416 (1980).

30   W.B. Person, J.H. Newton, *J. Molec. Struct.* 46, 105 (1978).

31   R.J. Bell, *Introductory Fourier Transform Spectroscopy*, (Academic Press, New York, 1972).

32   J.T. Houghton, S.D. Smith, *Infra–red Physics*, (Oxford Press, 1966).

33   G. Herzberg, *Molecular Spectra and Molecular Structure*, Vol. II, (Van Nostrand, Princeton, 1956)

34   A.C.G. Mitchell, M.W. Zemansky, *Resonance Radiation and Excited Atoms*, (Cambridge University Press, Cambridge, 1961).

35   M. Forman, W.H. Steel, G.A. Vanasse, *J. Opt. Soc. Am.* 56, 59 (1966).

36   G.M.W. Kroesen, P.H.J. Schellekens, to be published.

37   A.T.M. Wilbers, G.M.W. Kroesen, C.J. Timmermans, D.C. Schram, *Meas. Sc. Techn.* 1, 1326 (1990).

38   D.E. Jennings, *Appl. Opt.* 27(22), 4605 (1988).

39   E.O. Brigham, *The Fast Fourier Transform*, (Prentice–Hall, New Jersey, 1974).

40   J.W. Cooley, J.W. Tukey, *Math. Computation* 19, 297 (1965).

41   J. Connes, *Aspen Int. Conf. on Fourier Spectroscopy*, AFCRL–71–0019 (1970), pp. 83–115.

42   I. Langmuir, H.M. Mott–Smith, *Gen. Elec. Rev.* 26, 731 (1923).

43   G. Dilecce, M. Capitelli, S. De Benedictis, *J. Appl. Phys.* 69(1), 121 (1991).

44   V.A. Godyak, R.B. Piejak, *J. Appl. Phys.* 68(7), 3157 (1990).

45   L. Lindberg, *J. Phys.* E18, 214 (1985).

46   J. Brcka, R. Harman, *Vacuum* 36, 535 (1986).

47   N. St. J. Braithwaite, J.E. Allen, *J. Phys.* D21, 1733 (1988).

48   H. Anemiya, *Jap. J. Appl. Phys.* 27(12), 2423 (1988).

49   B. Agdur, B. Enander, *J. Appl. Phys.* 33(2), 575 (1962).

50   C.A.M. de Vries, A.J. van Roosmalen, G.C.C. Puylaert, *J. Appl. Phys.* 57(9), 4386 (1985).

51   F.J. Mehr, M.A. Biondi, *Phys. Rev.* 176(1), 322 (1968).

52   J.L. Jauberteau, G.J. Meeusen, M. Haverlag, G.M.W. Kroesen, F.J. de Hoog, *Appl. Phys. Lett.* 55(25), 2597 (1989).

53   T.H.J. Bisschops, F.J. de Hoog, *Proc. ISPC–7* (1985), 599 edited by C.J Timmermans, Eindhoven, Netherlands.

[54]   L.M. Buchmann, F. Heinrich, P. Hoffmann, J.H.Janes,
        J. Appl. Phys. **67**(8), 3635 (1990).

[55]   K. Kohler, D.E. Horne, J.W. Coburn, *J. Appl. Phys.* **58**(9), 3350 (1985).

[56]   L.J. Overzet, J.H. Beberman, J.T. Verdeyen, *J. Appl. Phys.* **66**, 1622 (1989).

[57]   R.A. Gottscho, C.E. Gaebe, *IEEE Trans. on Plasma Sc.* **PS**–14, 92 (1986).

[58]   J.C. Slater, *Rev. Modern Phys.* **18**, 441 (1946).

[59]   M. Haverlag, G.M.W. Kroesen, T.H.J. Bisschops, F.J. de Hoog,
        accepted for publication in Plasma Chem. Plasma Proc. 1991.

[60]   K.B. Persson, *Phys. Rev.* **106**(2), 191 (1957).

[61]   M. Sicha et al., *Brit. J. Appl. Phys.* **17**, 1511 (1966).

[62]   G. Janzen, *Z.f. Naturf.* **279**, 491 (1972).

[63]   J.L. Jauberteau, G.J. Meeusen, M. Haverlag, G.M.W. Kroesen,
        F.J. de Hoog, *J. Phys.* **D24**, 261 (1991).

5. RESULTS AND DISCUSSION

In this chapter the results of the calculations and the experiments, which were described in the chapters 3 and 4, respectively, are presented. In section 5.1 the results obtained with *in situ* ellipsometry on the surface of the etched wafer are given. In section 5.2 the results on the densities of neutral particles obtained using the infrared absorption setup are presented and discussed. Finally, in section 5.3 measurements of the electron and negative ion densities using microwave resonance and the photodetachment effect are shown, both in the plasma and in the afterglow and initiation phase of the plasma.

5.1 Surface phenomena

5.1.1 Introduction

In this section a study is made of the etching characteristics of the reactor. For this purpose, Si wafers covered with layers of SiO_2 and in some cases topped with Si have been placed on the (powered) lower electrode of the reactor and have been etched in RF plasmas of CF_4 and CHF_3. These systems have been chosen since they have been studied extensively by numerous authors. The etch rate has been measured with *in situ* ellipsometry. The results are compared with results from the literature and results from other diagnostics in this study. Moreover, experimental results concerning the contamination and damaging of the top layer of a Si substrate are presented and discussed for various feed gases and macroscopic plasma parameters.

A large number of authors have worked on the etching mechanisms of Si and SiO_2 in fluorocarbon RF plasmas. D'Agostino et al.[1] have argued that the etch rate of both Si and SiO_2 in fluorocarbon plasmas depends only on the F density in the plasma, since a directly proportional relation exists between the F density (measured by actinometry) and the etch rate for both materials. This proportionality of the etch rate with respect to [F] was also reported by Flamm et al.[2] who investigated the etching of Si and SiO_2 using an atomic fluorine radical source. They found that in this situation Si etches selectively over SiO_2, the $Si:SiO_2$ selectivity ranging from 42:1 at room temperature to 26:1 at 100 ^0C. This selectivity can be ascribed to the fact that the Si–O bond requires more energy to break[3] than the Si–Si bond, as is demonstrated in the temperature dependence of the etch rate[1,2]. The chemisorption of F is therefore easier in the case of Si. Due to the chemical origin of these processes, the etching is isotropic in these cases and the etch rate depends on the surface temperature. However, in the

presence of ion bombardment the etch rate can be increased significantly. For Si etching in gases containing only halogens and noble gases, this has been demonstrated by Coburn and Winters[4] who found a synergistic effect between the spontaneous etching by XeF_2 and ion bombardment. It is believed[5] that in this case the ions break bonds close to the surface, which are subsequently halogenated faster than in the case of the normal, purely chemical process. In this case the etching process is anisotropic since the ion bombarded parts of the surface are etched faster than the parts that are not bombarded. For Si etching in fluorocarbon—containing gases the anisotropy due to the ion bombardment is in most cases believed to be caused by the removal of inhibitor layers[5,6] that are deposited by $[CF_x]$ radicals. Since the removal of the fluorocarbon film is less at the side wall of the etched hole, the lateral etch rate is suppressed by an inhibiting film, whereas on the bombarded parts the inhibitor is constantly removed by the ion bombardment. Oehrlein et al.[6] have shown that in this case the etch rate is limited by the diffusion of fluorine and/or reaction products through the inhibitor layer.

In anisotropic etching of SiO_2 in fluorocarbon plasmas, the process is thought to be ion—enhanced through the formation of a thin fluorocarbon film that is activated by the ion bombardment[6], due to the production of dangling bonds in the oxide which can react with CF_x radicals.
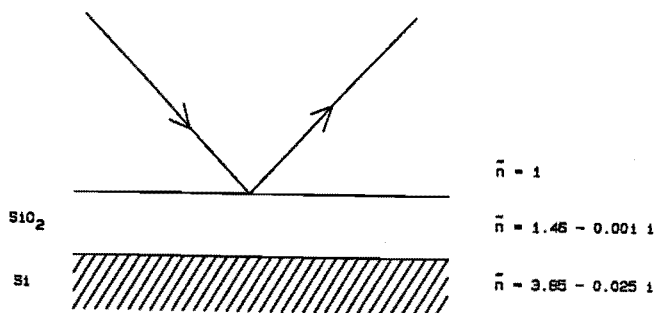

$\tilde{n} = 1$

SiO_2 $\tilde{n} = 1.46 - 0.001\,i$

Si $\tilde{n} = 3.85 - 0.025\,i$

Fig. 5.1   *Schematic view of the wafer structure that has been used for the measurement of the etch rate of SiO_2.*

5.1.2 Etch rates of Si and SiO₂

In order to obtain the etch rates of SiO_2, Si(100) wafers with a 1 μm thick layer of thermally grown oxide (see figure 5.1) were etched in a fluorocarbon plasma. During the etching process, the thickness of the oxide layer decreases linearly with time. Each thickness corresponds to a specific Δ, Ψ combination, and thus the ellipsometer produces a contour in the $\Delta-\Psi$ plane as the time elapses. The shape of the contour depends on the (complex) refractive index $\bar{n}(SiO_2)$ of the layer, the refractive index $\bar{n}(Si)$ of the Si substrate and the angle of incidence. Although the refractive index of monocrystalline Si at the applied wavelength is known[7,8], the system is still not completely defined by one single measurement. One single measurement produces two parameters (Δ and Ψ) whereas three values are unknown ($\bar{n}(SiO_2)$ and d). However, since the thickness is a (linear) function of time, it can be eliminated as an unknown parameter by simulating the $\Delta-\Psi$ curves corresponding to a decreasing film thickness. $\bar{n}(SiO_2)$ can then be determined by fitting the simulation curve to the measured curve. In figure 5.2 some examples of simulated contours for different refractive indices of SiO_2 and a measured contour are given. After fitting the simulation to the measured contour by tuning $\bar{n}(SiO_2)$ and the angle of incidence, the thickness at each time can be inferred from the
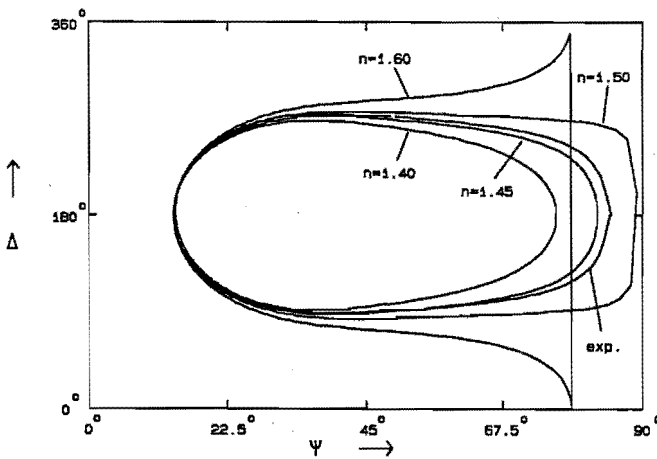

Fig. 5.2 *Simulated $\Delta-\Psi$ contours and one measured $\Delta-\Psi$ contour for the structure depicted in figure 5.1. Parameter is the refractive index of the SiO_2 layer. The thickness of the layer can be inferred from the position on the curve. Each full revolution of the egg–shaped curve corresponds to an etched thickness of $\approx$ 274 nm.*

position on the measured curve.

For the measurement of the etch rate of Si another structure has been used in which a Si substrate is covered with a thin ($\approx$ 90 nm) layer of thermally grown oxide, topped with a 300 nm layer of (poly)crystalline Si (see figure 5.3). In this case six parameters are to be determined in the system (i.e. the complex refractive indices and the thickness of both the oxide and poly–Si layer). Therefore simulation of the $\Delta-\Psi$ contours is difficult. The simulation can be simplified much by describing the ellipsometric effects using the impedance factor approach[9,10]. In this method the substrate and the oxide layer can be described by an 'effective' substrate with an effective impedance factor that contains the properties of the substrate, the oxide layer and the part of the poly–Si layer that is present at the starting point of the simulation. An example of a measured contour is given in figure 5.4. It was derived from a comparison between experimental and simulated curves that the refractive index of the oxide layers is about $1.46 - 0.001$ i, in good agreement with the literature values of 1.46 (ref. 11) and 1.45 (ref. 12). For the poly–Si layers a value of $3.9 - 0.04$ i was found to be adequate to fit the experimental curves, in reasonable agreement with literature values[7,8] (i.e. $3.85 - 0.025$ i) of the refractive index of single crystalline Si.

At an angle of incidence of 68^0, the thickness that is etched away in a full revolution of the $\Delta-\Psi$ contour is about 274 nm for SiO_2 and about 84 nm for Si. Therefore in both situations 3 to 4 revolutions of the contour occur before the entire layer is etched off. The same wafer can therefore be used for several etch rate measurements at different conditions.

Since a rotating–analyzer ellipsometer in principle only yields cos Δ, it is not possible to distinguish between Δ and $360^0-\Delta$ in a single measurement. However, since a simulation of the ellipsometric effect of a thin (< 100 nm) layer of SiO_2 on Si yields that in that case Δ is always smaller than 180^0, the end point for both wafer structures used is at a value for Δ for which $\Delta < 180^0$. Therefore, when the entire layer is etched off, for each measurement point we can easily determine whether it lies above or below the line $\Delta = 180^0$.

In figure 5.2 and 5.4 it can be seen that the $\Delta-\Psi$ contours are in both cases slightly asymmetric with respect to the line $\Delta = 180^0$. For the first case (SiO_2 on top of Si) for a small part this can be explained as a result of the imaginary part of the refractive index of the Si substrate, effects due to window birefringence or as a result of the existence of a modified toplayer of SiO_2. However, a simulation of the actual shape of the asymmetry, which can well be demonstrated in the $a-b$ plane (see figure 5.5, where a and b are the Fourier coefficients of the ellipsometer signal), shows that of these possibilities only the existence of a modified top layer explains the actual shape of the
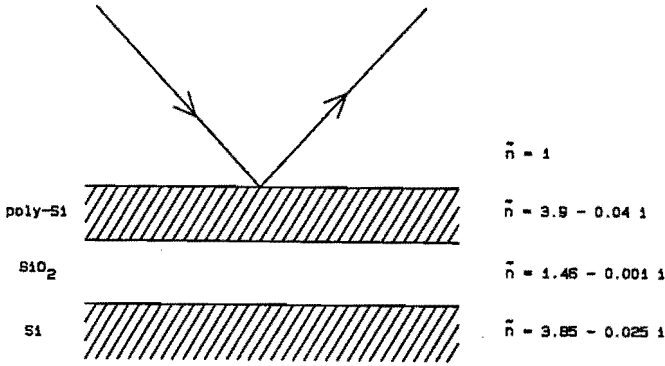
poly-Si

SiO₂

Si

$\tilde{n} = 1$

$\tilde{n} = 3.9 - 0.04\,i$

$\tilde{n} = 1.46 - 0.001\,i$

$\tilde{n} = 3.85 - 0.025\,i$

Fig. 5.3   Schematic view of the wafer structure that has been used for the measurement of the etch rate of Si.
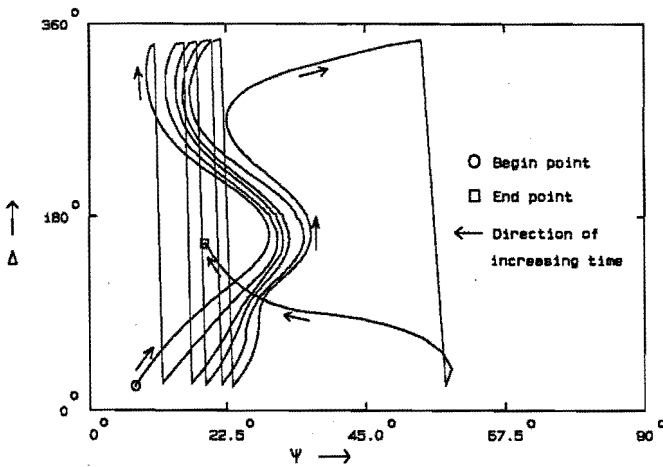

Fig. 5.4   Example of a measured $\Delta - \Psi$ contour for the sandwich−like structure depicted in figure 5.3. As a result of the imaginary part of the refractive index of the poly−Si layer the contour systematically shifts to higher values of Ψ with decreasing thickness. In the last part of the etching process the SiO₂ layer is reached and the shape of the curve becomes similar to that in figure 5.2.

curve in the a–b plane, in which the part of the curve in which a increases crosses the part in which a decreases (see curve I and IV). Without a top layer both parts of the curve do not cross. A similar asymmetry is observed in the case of the Si-SiO$_2$-Si sandwich wafer. In both cases a roughened layer with an effective thickness of about 15–20 nm can explain the observed phenomena. The roughening may be the result of the redeposition of sputtered Al or Cu—impurities from the walls during etching[13-15] which can locally and temporarily inhibit the etch reaction.

The etch rate of Si and SiO$_2$ has been determined in the open configuration for plasmas in both CF$_4$ and CHF$_3$. To avoid loading effects, only a small part of a wafer with an area of 25x25 mm was used in the experiments. Measurements were performed in two situations, one in which the powered electrode was preconditioned by a 120 mTorr, 80 W CF$_4$ plasma to remove possible deposited material from previous runs, and
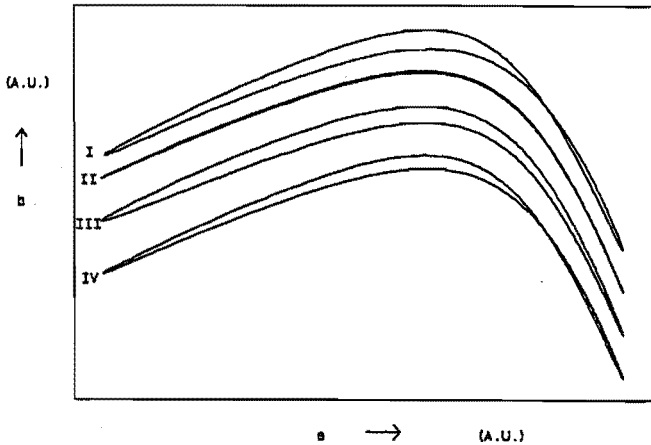

Fig. 5.5   *Demonstration of the ellipsometric effects in the a–b plane of a toplayer and of window birefringence on the shape of the a–b curve during the removal of a SiO$_2$ layer on a Si substrate. For comparison, a measured a–b curve is shown (I). The curves are offset along the b–axis for clarity. Curve II shows a simulated contour without toplayer and without window effects. Curve III shows the effect of window birefringence. Curve IV shows the effect of both window birefringence and a toplayer. Since both parts of the curve only cross when a top layer is taken into account, this suggests that a modified top layer is present on top of the SiO$_2$ during the etching process.*

one in which the powered electrode was covered by a 500 nm thick $[CF_x]_n$ layer using a 300 mTorr, 80 W CHF_3 plasma prior to the mounting of the wafer. The deposition process was monitored also with the ellipsometer using a small silicon sample on the electrode, yielding curves similar to the ones shown in figure 5.2. Measurements of the etch rate were performed as a function of gas pressure and RF power. The results are depicted in figures 5.6 – 5.10. It can be seen in figure 5.6 that the etch rate of Si in CF_4 has a maximum at around 100 mTorr, whereas the maximum in a CHF_3 plasma is found at a lower pressure, around 30 mTorr. The etch rate of Si is systematically lower in CHF_3 plasmas than in CF_4 plasmas. Furthermore the etch rate is suppressed by the presence of a $[CF_x]_n$ coated electrode.

Figure 5.7 shows the pressure dependence of the etch rate of SiO_2. In the case of SiO_2 etching also a maximum is observed in the etch rate. However, the position of this maximum is the same for both CF_4 and CHF_3 plasmas. Furthermore the etch rate is only slightly influenced by the presence of a $[CF_x]_n$ coated electrode. In figure 5.8 the etch rate of Si is given as a function of the RF power applied. It shows that the etch rate is directly proportional to the RF power at low pressures in both CF_4 and CHF_3 plasmas, whereas at high pressures the etch rate increases slightly faster than linear. This non–linearity of the etch rate with respect to RF power is also observed in SiO_2 etching, as can be seen in figure 5.9. Figure 5.10 shows that the etch rate of SiO_2 decreases fast as a function of pressure for both CF_4 and CHF_3 at low power levels. At 20 W RF power and pressures above 110 mTorr in CHF_3 plasmas, the etching of SiO_2 is even totally suppressed.

In figure 5.6 it can be seen that the etch rate of Si is strongly influenced by the electrode material. There are three phenomena that contribute to this behavior.

Firstly, in the case of the $[CF_x]_n$ electrode extra amounts of CF_x radicals are produced by sputtering of the electrode material. This leads to an increase of the CF_x radical densities in the gas phase. This again gives rise to an increased loss of atomic fluorine by recombination with (mainly) CF_3. Moreover, the increase of the CF_x density gives rise to an increased flux of CF_x radicals to the Si surface being etched, which causes an increase in the deposition rate of $[CF_x]_n$ on that surface. Therefore the thickness of the fluorocarbon film increases, inhibiting the etching of Si by fluorine radicals[6]. Finally etching of the $[CF_x]_n$ layer on the electrode by fluorine radicals leads to loss of F.

Secondly, catalytic decomposition of CF_x radicals may occur at the Al surface as has been suggested for CF_4/O_2 plasmas[16], hence increasing the removal of CF_x radicals from the plasma and production of F at the surface. This explanation is however not very likely in the case of a pure CF_4 discharge, since in that case the carbon–rich layer
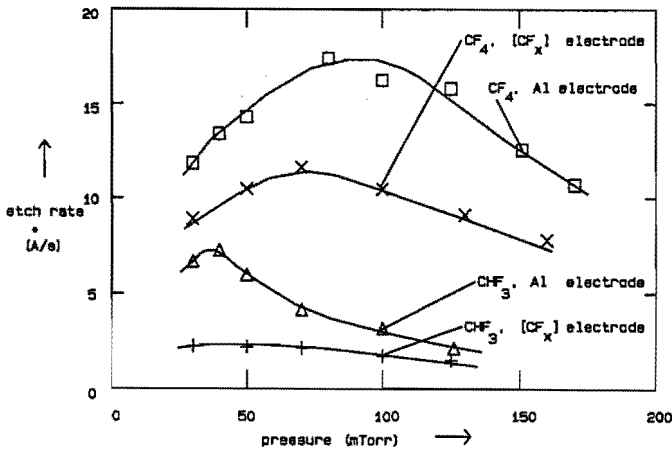
Fig. 5.6   The etch rate of (poly−) Si as a function of the gas pressure in RF plasmas
in CF_4 and CHF_3. The RF power was 80 watt and the gas flow 20 sccm.
Measurements were performed both with a clean Al driven electrode and
with a $[CF_x]_n$ predeposited driven electrode.

Fig. 5.7   The etch rate of SiO_2 as a function of the gas pressure in RF plasmas of
CF_4 and CHF_3. The RF power was 80 watt and the gas flow 20 sccm.
Measurements were performed both with a clean Al driven electrode and
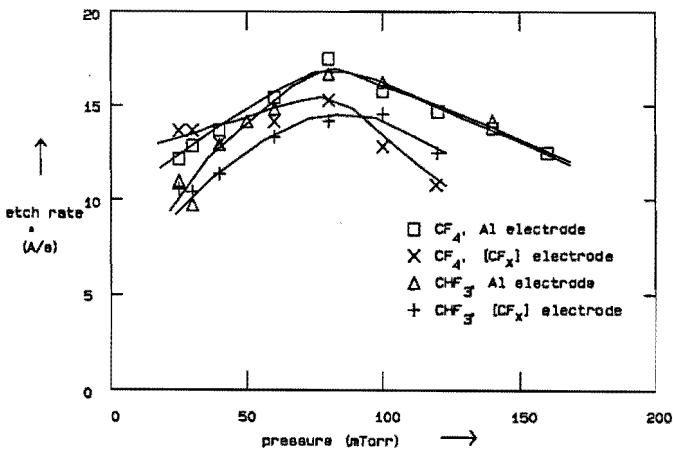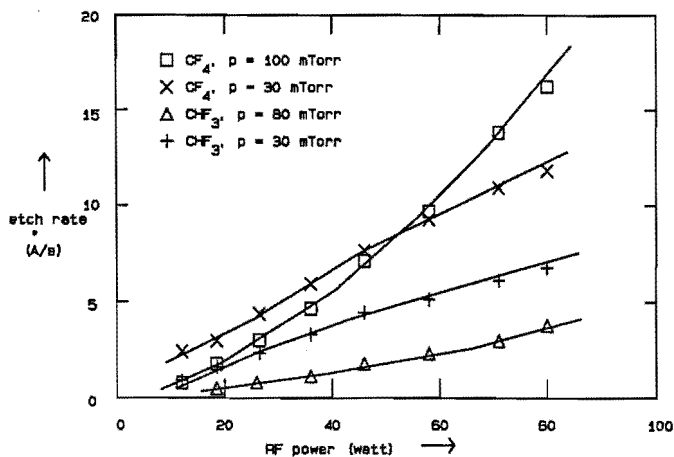with a $[CF_x]_n$ predeposited driven electrode.

Fig. 5.8   The etch rate of (poly−) Si as a function of the RF power in RF plasmas
of CF_4 and CHF_3. Parameter is the gas pressure. The gas flow was 20
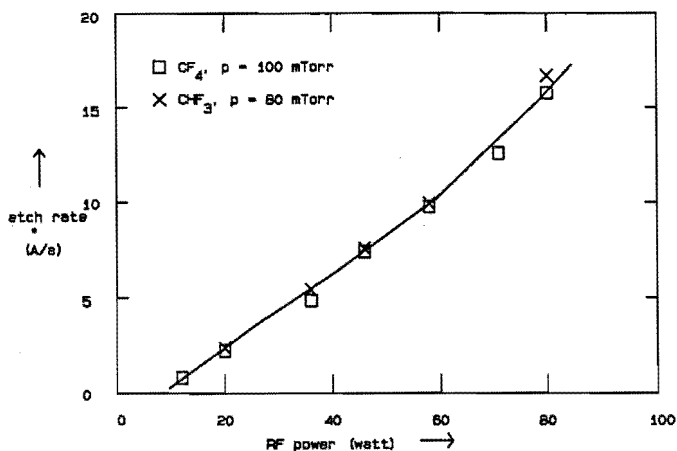sccm. The measurements were performed using a clean Al electrode.

Fig. 5.9   The etch rate of SiO_2 as a function of the RF power in RF plasmas of CF_4
and CHF_3. The gas flow was 20 sccm. The measurements were performed
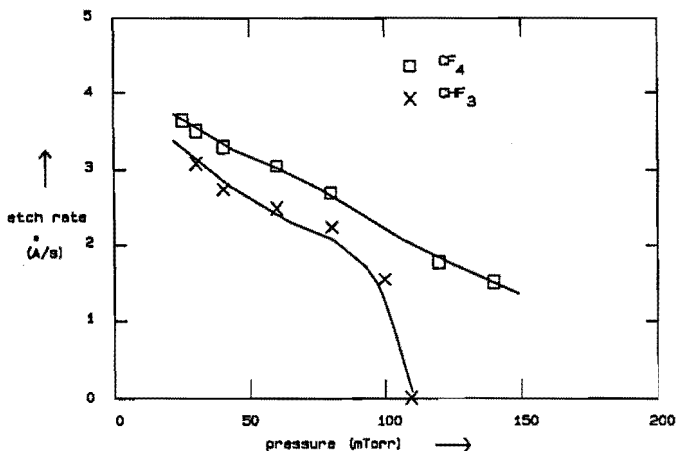using a clean Al driven electrode.

Fig. 5.10   The etch rate of SiO_2 as a function of the gas pressure in RF plasmas of
                CF_4 and CHF_3. The RF power was 20 watt and the gas flow 20 sccm. The
                measurements were performed on a clean Al driven electrode.

formed by the decomposition on the electrodes is not removed by oxygen. After a while
the aluminum is therefore covered with a thin layer that blocks the catalytic effect.

        Thirdly, changes in the charged particles balance due to the change in the neutral
gas chemistry, such as detachment of negative ions induced by collisions with neutral
CF_x radicals (see section 5.3), might give rise to a lowering of the ion densities. This is
due to the fact that the negative ion density is much higher than the electron density
(see section 5.3). A decrease of the negative ion density therefore means that the
positive ion density must decrease too, to preserve the quasineutrality in the plasma. As
a result, the ion flux to the surface might be lowered, causing a lowering of the removal
rate of the polymer layer, and therefore a reduction of the etch rate. To investigate the
effect of extra detachment of negative ions, the simulation described in section 3.3.2 was
run in two situations, one in which the detachment rate was used that was obtained
from afterglow experiments (see section 5.3) and one in which the detachment rate was
taken to be 5 times higher. The results are given in table 5.1. In can be seen in this table
that the ion densities in the center of the plasma are lowered due to the increase in
detachment rate, but the ion fluxes on the surface are almost the same. The simulation
therefore suggests that the effect of extra collisional detachment with neutral radicals
that are sputtered from the electrodes on the ion flux is small.

Table 5.1   *Simulation of the effect of an increase in the detachment of negative ions on the ion flux impinging on the surface. The simulation was run at a pressure of 200 mTorr and an RF power of 20 watt.*

detachment rate (s^{-1})	n^+ (m^{-3})	ion flux $(m^{-2}s^{-1})$
6000	$2.07 \cdot 10^{16}$	$1.96 \cdot 10^{19}$
30000	$1.03 \cdot 10^{16}$	$1.91 \cdot 10^{19}$

In the case of SiO_2 etching the etch rate is also reduced in the case of a $[CF_x]_n$ coated electrode, but the effect is smaller than in the case of Si (see figure 5.7). This can be understood since the etch rate of SiO_2 is primarily limited by the flux of positive ions. These ions are necessary for the etch reaction since the CF_x radicals do not spontaneously etch SiO_2[17] and F radicals etch SiO_2 only very slowly[5]. In SiO_2 etching the role of the ions is to perform or enhance the etching reaction rather than to remove the inhibitor layer. This is suggested by the experimental observation that during SiO_2 etching only a thin polymer layer forms on top of the surface[18]. The effect of a change in the thickness of this inhibitor layer is therefore smaller than in the case of Si.

In figure 5.6 it can be seen that the etch rate of Si as a function of pressure in CHF_3 shows a distinct maximum at around 30 mTorr. This clearly demonstrates the importance of the fluorocarbon film inhibiting the etch reaction in this case. Around the optimum point the thickness of the fluorocarbon film will be small since the high positive ion flux at low pressure[19] constantly removes the film that builds up on the surface. In this region the etch rate reflects the fluorine density which increases with pressure, as is known from actinometry measurements[19]. At higher pressures the ion flux decreases[19] and the fluorocarbon film thickness increases, thus lowering the etch rate.

In the case of Si etching in CF_4 plasmas the dependence on the pressure reaches a less distinct maximum at a pressure of 100 mTorr. In this case the role of the fluorocarbon film is less important since the C/F ratio is in CF_4 smaller than in CHF_3. Therefore less CF_x radicals that can act as building blocks for polymerization are formed, whereas more fluorine radicals are formed that can remove adsorbed CF_x radicals from the surface. The fact that the etch rate of Si decreases at higher pressure in CF_4, despite the increasing fluorine density and the absence of an inhibiting fluorocarbon layer (see next section), suggests that at intermediate pressure the etching process is at least in part ion–activated.

The effects of the deposition of a fluorocarbon film during SiO_2 etching are also

demonstrated in figure 5.10. In this measurement the pressure dependence of the etch rate is shown at low RF power. In this condition the SiO_2 etch rate maximum in CF_4 is found at a lower pressure than in the high RF power case, probably because the ion flux and ion energy are now much smaller. In a CHF_3 plasma at high pressure the overall reaction can even change from etching to deposition (above $\approx$ 100 mTorr at 20 W RF power). In that case a thick fluorocarbon film starts to be deposited[8], and the ellipsometric contour reverses its direction with respect to time. From the shape of this contour we derived a value for the refractive index of the film, similar as in the case of an etching SiO_2 layer. We estimated that $n_{film} = 1.50$, which is close to the value of 1.48 found by Oehrlein et al.[8] in a CF_4/H_2 plasma. XPS analysis of the surface with a thick film deposited revealed that the film is teflon–like, with mostly CF_2 groups present. In figure 5.10 it can be seen that at very low RF power levels the etch rate is suppressed very much, in agreement with the literature[20]. This is probably due to a steep reduction in both the ion flux and the ion energy at low power levels[19,20], combined with a thicker surface reaction layer.

5.1.3 Modification of the surface during Si etching

During etching of silicon the surface is modified as a result of the ion bombardment and $[CF_x]_n$ film deposition. To get some more information on this, experiments were performed on a Si substrate without any layer on top of it, except for a native oxide layer. The start of the etching process was monitored by *in situ* ellipsometry. Since the modification of the surface yields only small effects in Δ and Ψ the sensitivity of the ellipsometer was improved by applying a compensator and using the ellipsometer in the PCSA configuration. Since the ellipsometric effects are small and a small tilt of the wafer due to temperature effects on the electrode after plasma switch–on can give rise to significant changes[10] in Δ and (mostly) Ψ, the samples were "glued" to the electrode using Torr–seal vacuum grease and heat treatment of the electrode at 200 ^{0}C for about 5 minutes. Measurements of the changes in Δ and Ψ were carried out as a function of time in plasmas of CF_4 and CHF_3, starting the measurement just before the plasma was ignited. Examples of measured contours are given in figures 5.11 and 5.12. The values of Δ and Ψ change after ignition of the plasma due to the removal of the native oxide, the formation of a fluorocarbon film and the damaging of the upper layer of the silicon. To interpret the shape of the contours, estimates of the refractive indices of the native oxide, the fluorocarbon film and the damaged Si are needed. For the native oxide layer we have used the value from the SiO_2 etching contours (i.e. 1.46). The refractive index for damaged Si was taken from ion beam
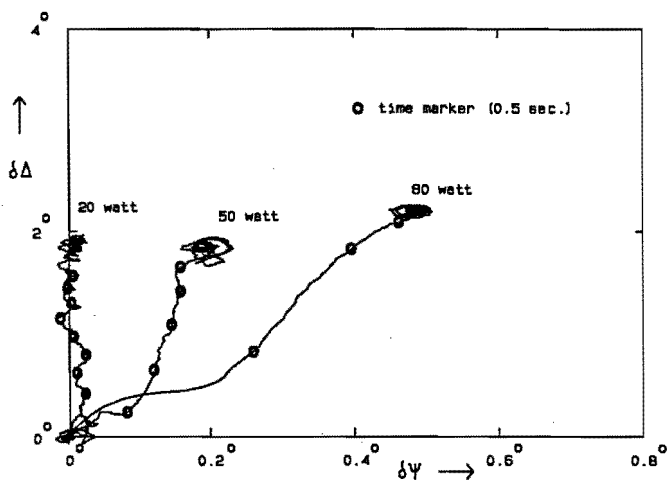
Fig. 5.11 Measurement of the $\Delta - \Psi$ contour in the beginning stage of the etching process in a plasma of CF_4 at 120 mTorr. Parameter is the RF power applied. Since the shift in Δ is mainly due to the removal of the native oxide and formation of a fluorocarbon layer (see text), it can be seen that the fluorocarbon film thickness during etching is smaller than the native oxide present before the beginning of the etching process.
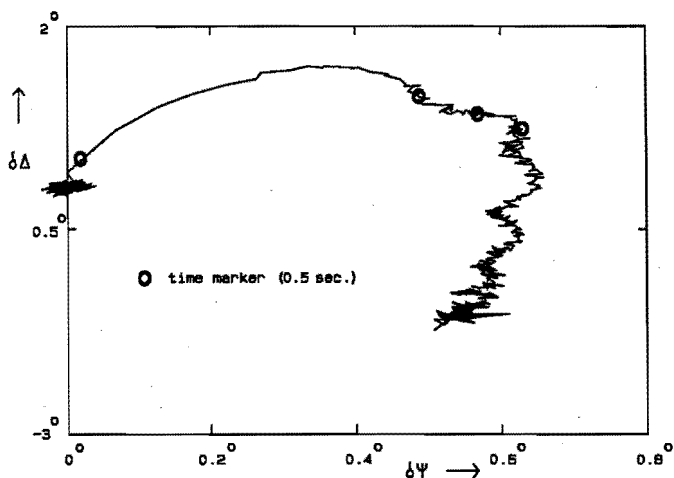

Fig. 5.12 Measurement of the $\Delta - \Psi$ contour in the beginning stage of the etching process in an 80 W plasma of CHF_3. It can be seen that the fluorocarbon film thickness in this case is much larger than in the case of CF_4, whereas the damaging is comparable. The oscillation that is visible in the later part of the curve is caused by a 50 Hz distortion in the measurement signal.

damaging experiments[7] (i.e. $4.76 - 0.76$ i). The value for the refractive index of the
fluorocarbon is relatively difficult to estimate since the composition of the layer depends
on the thickness of the layer[8]. For thick layers the value for the teflon–like layers (i.e.
1.50) can be taken. For thin layers the C/F ratio in the layer is higher than for thick
layers due to graphitization of the upper part of the layer by the ion bombardment[21].
We can therefore assume that the refractive index of these layers tends towards that of
carbon–like films (i.e. $1.5 - 2.0$, see ref. 9). If we use an optical model in which the
effects of the fluorocarbon film and the damaged layer are treated separately (see figure
5.13), the ellipsometric effects are also separated (see figure 5.14). The damaged layer
mostly gives rise to a change in Ψ, whereas the fluorocarbon layer mostly induces a
change in Δ. Since the refractive index of the native oxide layer is comparable to that of
the fluorocarbon layer, the ellipsometric effect of such a layer is also comparable to that
of the fluorocarbon layer. In figure 5.11 it can be seen that after switch–on of a CF_4
plasma Δ increases in all cases. The stationary situation that results after a few seconds
is also characterized by a Δ that is higher than in the starting situation of the
experiment. This implies that the fluorocarbon layer that is present on top of the Si
during etching in CF_4 is thinner than the native oxide layer that was present before
etching. The thickness of the native oxide is in most cases[22] 0.6–1.0 nm. Therefore the
thickness of the fluorocarbon layer, being equal to or smaller than 0.6–1.0 nm, is in the
investigated cases too small to inhibit the etching of Si significantly[6]. In the case of
CHF_3 (see figure 5.12) the overall Δ change is negative, which implies that in CHF_3 the
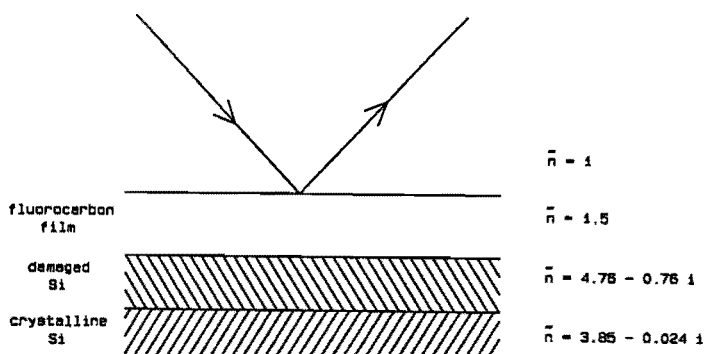

Fig. 5.13   Optical model of the top layer of silicon during etching. The effects of
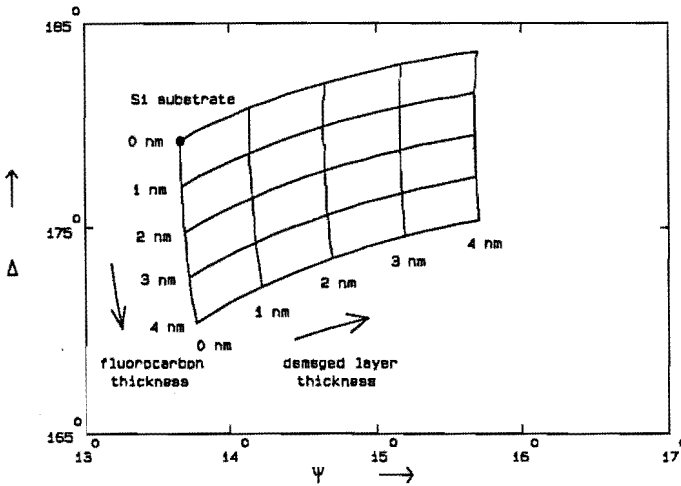   damaging and fluorocarbon film deposition are treated as separate layers.

Fig. 5.14   *Simulation of the ellipsometric effects of damaging and fluorocarbon film deposition during etching. It can be seen that the change in Ψ is mostly caused by damaging, whereas the change in Δ is mostly caused by the fluorocarbon film.*

thickness of the $[CF_x]_n$ film is larger than the native oxide layer thickness. In both CF_4 and CHF_3 we can see that the etching process starts with the removal of the native oxide and damaging of the surface, after which the fluorocarbon film starts to buildup on the surface. In the measurement in CHF_3 the changes in Δ that are found are much smaller than have been reported by Cardinaud et al.[11], who found changes in Δ of up to 22^0 (corresponding to ≈ 9 nm). However, Cardinaud et al. measured *ex situ*, which may lead to some oxidation of their samples in the open air after the etching process. They did not report values for Ψ, which makes it more difficult to distinguish between effects due to damaging and effects due to the formation of a fluorocarbon film.

The dependence of the thickness of the damaged layer and of the fluorocarbon layer on macroscopic plasma parameters was measured in the stationary situation on a single Si wafer. Since the thickness of the native oxide layer before etching was not known accurately, the changes of Δ and Ψ were determined with respect to reference values. The reference value for Δ was obtained at a high power, high pressure plasma in CF_4. Since we cannot be absolutely sure that in this situation the fluorocarbon film is completely absent, a systematic error in the determined fluorocarbon thickness of about 0.5 nm cannot be ruled out. The reference value for Ψ was obtained at a low power, high
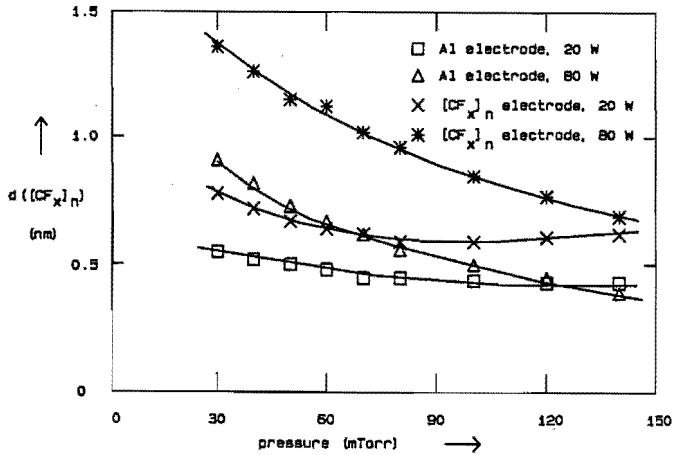
Fig. 5.15   *The fluorocarbon film thickness in a CF_4 plasma as a function of pressure. Parameters are the RF power applied and the electrode material. The fluorocarbon layer thickness is relatively small in the case of CF_4. As a result of the measurement procedure used, a systematic error of about 0.5 nm cannot be ruled out.*
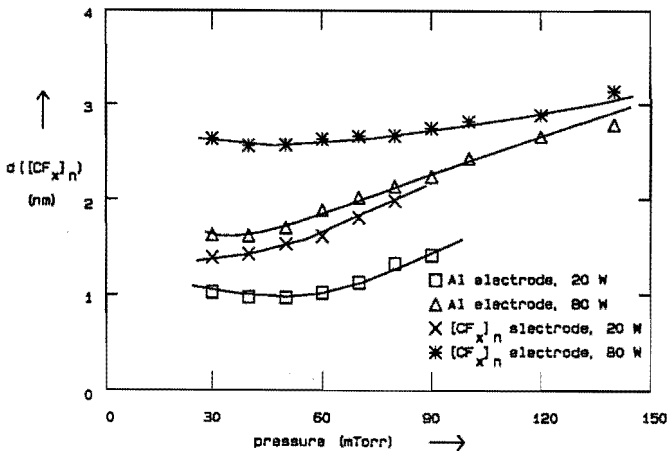

Fig. 5.16   *Fluorocarbon film thickness in a CHF_3 plasma as a function of pressure. Parameters are the RF power applied and the electrode material. The fluorocarbon layer thickness is greater than in the case of CF_4.*

Fig. 5.17 *The damaged layer thickness in a CF_4 plasma as a function of pressure. Parameters are the RF power applied and the electrode material. The damaging increases with the RF power and decreases with pressure.*
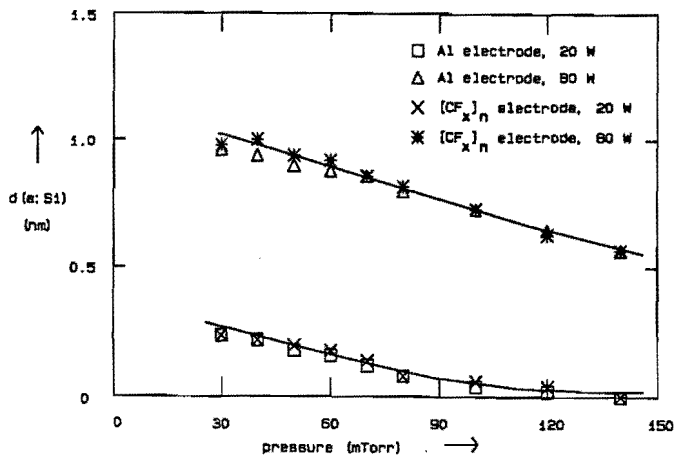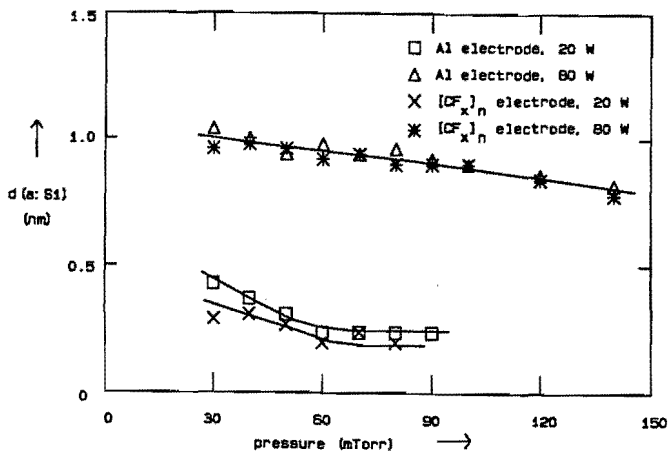

Fig. 5.18 *The damaged layer thickness in a CHF_3 plasma as a function of pressure. Parameters are the RF power applied and the electrode material. The behavior is comparable to that in a CF_4 plasma.*

pressure plasma in CF_4. Under these conditions the thickness of the damaged layer is expected to be minimal. The thicknesses of the fluorocarbon film and of the damaged layer, as calculated from the changes in Δ and Ψ and as a function of pressure, electrode material and RF power in plasmas of CF_4 and CHF_3 are given in figures 5.15 − 5.18. In figure 5.15 it can be seen that in pure CF_4 plasmas the fluorocarbon layer thickness is somewhat thicker in the case of a $[CF_x]_n$–coated electrode than in the case of an Al electrode. However, in both electrode circumstances the layer is too thin to have a large effect on the etch rate of Si. Therefore it is more likely that the change in C/F ratio in the plasma is responsible for the lower etch rate with a $[CF_x]_n$–coated electrode. At higher pressures and high RF power in CF_4 the film thickness is at its minimum value. In this situation CF_x radicals are removed fast by fluorine. Since in CHF_3 plasmas the fluorine density is lower (see section 5.2) this removal mechanism is much less effective in CHF_3, as can be seen in figure 5.16. The layer thickness increases with pressure in CHF_3 above 30 mTorr, which corresponds to the maximum in the etch rate at low pressure that can be seen in figure 5.6. Figures 5.17 and 5.18 show that damaging is proportional to the RF power level, as can be expected since both ion energy and ion fluxes increase with the RF power[19].

Both contamination of the surface and damaging are undesired in device fabrication. Both effects can be reduced without loss of wafer throughput, by applying a pure CF_4 plasma at low pressure (e.g. 30 mTorr) and low RF power in the last stage of the etching process. This may then reduce the necessity of post–etching O_2 plasma treatment and HF dip[23]. A good pre–endpoint detection system is then however necessary. *In situ* ellipsometry may be very suitable for this purpose.

5.1.4 Conclusions

It has been shown that *in situ* ellipsometry can provide for an excellent monitor of the process. Not only an accurate determination of the etch rate is possible but also information can be obtained on the optical properties of the layer being etched or deposited. The observed trends in the etch rate as a function of the macroscopic plasma parameters suggest that in the case of Si etching in fluorocarbon RF plasmas both ion–enhanced processes as well as the formation of an inhibitor layer take place. The etching of SiO_2 is likely to be ion–enhanced. Furthermore the electrode material has an influence on the selectivity of the process, since Si etching is reduced in the presence of a $[CF_x]_n$ coated electrode whereas the etching of SiO_2 is hardly influenced.

It was furthermore established that during etching in CF_4 a thin fluorocarbon layer is present on the surface, that hardly inhibits the etching reaction, whereas during

etching in CHF_3 this layer is thicker. The influence of the inhibitor is therefore larger in CHF_3 than CF_4 plasmas. Damaging due to the ion bombardment during the process increases with the RF power and decreases with the pressure in agreement with the trends of the ion fluxes and ion energies that are known.

5.2 Neutral particles in the plasma

5.2.1 Introduction

In chemically active plasmas several types of particles, such as free radicals and negative and positive ions are produced by dissociation, attachment and ionization induced by impact of fast electrons in the plasma. Therefore much of the physics and chemistry of the plasma is determined by the electron energy distribution function (EEDF), and many authors have studied the EEDF theoretically[24-25]. A factor which can strongly affect the EEDF is the amount of vibrationally excited molecules, since the electrons can gain energy through superelastic collisions[26] with these molecules. Moreover, the production of negative ions by resonant dissociative attachment can be affected by a high population of vibrationally excited molecules as has been demonstrated for the cases of H_2 [27] and HCl [28]. The rotational excitation is in most cases closely coupled with the gas temperature which determines in many cases the rate coefficients for chemical reactions between unexcited heavy particles[29].

Experimental data on the vibrational and rotational excitation mostly come from emission spectroscopy of electronic transitions. For instance, the vibrational and rotational excitation of N_2 impurities in an inductively coupled CF_4 plasma has been measured by van Veldhuizen et al.[30] who found a value of 3000 K for the vibrational temperature T_{vib} and 550 K for the rotational temperature T_{rot}. However, since during the population of the emitting state in a plasma the vibrational and rotational distribution may be changed, this need not be an accurate reflection of the vibrational excitation of the ground state molecules of N_2, let alone of the vibrational excitation of CF_4 itself, which is the dominant species in the plasma described. However, CF_4 does have infrared absorption bands of vibrational transitions which can also be used to measure T_{vib} and T_{rot}. A method to do this is explained in section 5.2.2, where also some results obtained in a CF_4 plasma are given.

It is shown in section 5.3 that the radical chemistry can have a strong influence on the charged particles kinetics through detachment reactions with negative ions. Moreover the etching characteristics of the discharge are strongly influenced by the flux of neutral radicals towards the surface being etched, as has been demonstrated in section 5.1. Measurements of the densities of CF_2 and C_2F_6 in a CF_4 plasma will be given in section 5.2.3. Using the model of the neutral radical kinetics described in section 3.2, and taking into account all measured data on the charged and neutral particle densities, in section 5.2.3 also an estimate will be given of the density of CF_3 radicals.

5.2.2 Vibrational excitation in a CF$_4$ plasma

a) Introduction

CF$_4$ shows its four fundamental vibrational transitions in the infrared region between 400 − 1300 cm^{-1}. The frequencies for the ν_1, ν_2, ν_3 and ν_4 transitions are given in Table 5.2. For symmetry reasons, only the ν_3 and ν_4 transitions show an infrared absorption spectrum. We can see that the ν_2 transition requires the least energy for excitation, i.e. 435 cm^{-1} (or 53.8 meV). This value is not far from the average energy of the molecules (which is about 26 meV at 300 K). Therefore even at room temperature some of the lower vibrational levels of the ν_2 transition will be significantly populated. This has an effect on the band shape of the ν_3 peak. Besides the normal transition of ν_3 which starts from the ground state, transitions are also possible from vibrationally excited states, such as ν_2, $2\nu_2$, $3\nu_2$, etc. (see figure 5.19). The Q branches[31,32] (with $\Delta J=0$, see section 4.2.2) of the transitions from these states will in the rest of this study be denominated as Q$_1$, Q$_2$, Q$_3$, ... Transitions from excited states are usually known as 'hot bands' [31,32]. If the potential curve of CF$_4$ is harmonic, the energy difference between the upper level $\nu_3 + n\nu_2$ and the lower level $n\nu_2$ is constant. In this case all hot bands coincide. In reality however the potential curve of the CF$_4$ molecule is slightly
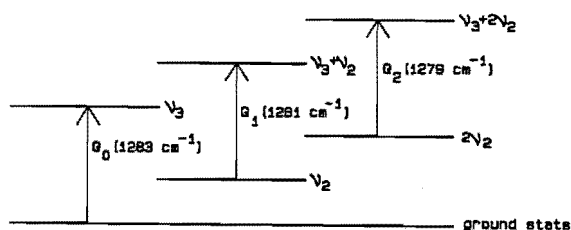

Fig. 5.19   *Schematic representation of the vibrational transitions of CF$_4$ which are of importance in the context of this study. The intensities of the hot−band transitions are a measure of the population of the ν_2 levels from which they start.*
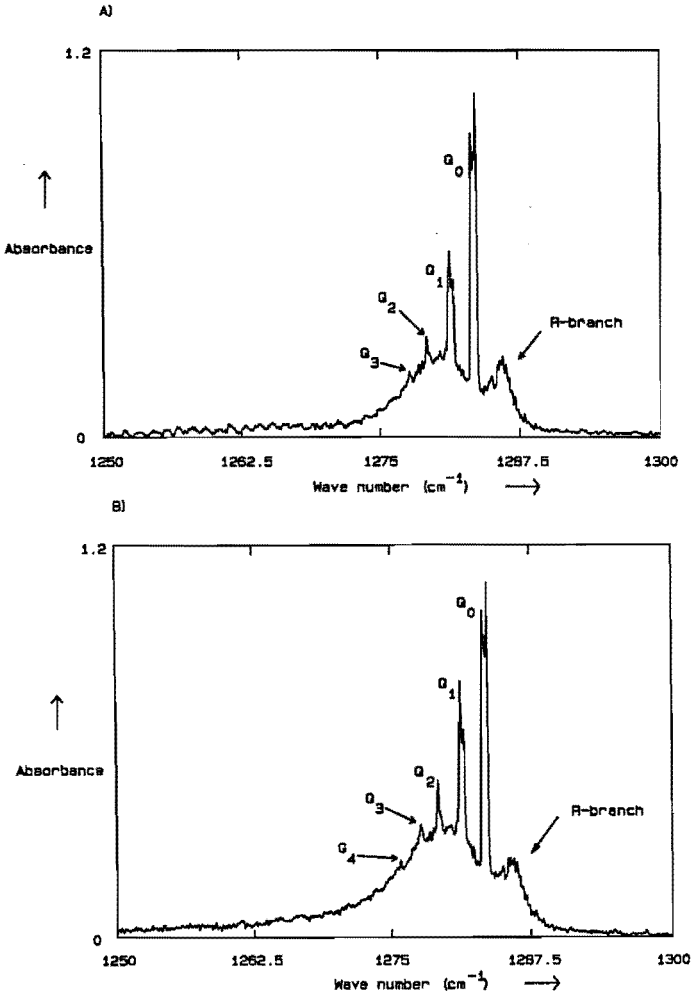
Fig. 5.20   *High−resolution absorption spectrum of the* CF_4 ν_3*−peak around 1283*
             cm^{-1} *at 0.12 cm*$^{-1}$ *apodized resolution. The broad continuum superimposed*
             on the Q−band structure is due to the P− and R−branches of the ν_3 *band.*

             a)   *without plasma, T = 300 K, p = 50 mTorr. At 1281 and 1279 cm*$^{-1}$
                  the hot Q branch transitions can be seen. The intensity ratio
                  between Q_0 *and* Q_1 *is about 3.27.*

             b)   *with plasma, p = 100 mTorr. It can be clearly seen that the*
                  intensity of the hot Q branches has increased relative to the
                  ground state Q branch. The intensity ratio between Q_0 *and* Q_1 *is*
                  now 2.35. From this it follows that the vibrational temperature is
                  higher in the plasma (i.e $T_v \approx 400$ *K in the plasma).*

anharmonic, which causes the frequency corresponding to the hot band transitions to be shifted downwards a small amount. This results in a ν_3 band shape as depicted in figure 5.20a for a measurement without plasma. This band shape is identical to the one obtained by Jones et al.[31]. Besides the 'normal' ν_3 band located around 1283 cm^{-1}, additional bands occur around 1281 and 1279 cm^{-1}. The Q–branch is the sharpest feature in the ν_3 spectrum. Therefore the effect of hot bands is shown very clearly by the occurrence of extra Q bands.

Table 5.2 *Fundamental vibrational transitions of CF_4. The values for the frequencies are taken from ref. 31. The ν_1 and ν_2 modes are infrared inactive on grounds of symmetry.*

Mode	Frequency (cm^{-1})	Degeneracy
ν_1	908.5	1
ν_2	435.0	2
ν_3	1283.2	3
ν_4	631.2	3

b) Method

The relative intensity of the Q branches is a direct measure for the population of the ν_2 levels which are the lower level of the several Q branches of the ν_3 transition. If we assume a Boltzmann distribution for the ν_2 levels, the intensity ratio of $\nu_3 + \nu_2 - \nu_2$ over ν_3 (or $I(Q_1)/I(Q_0)$) is proportional to a Boltzmann factor $g_0/g_1 \cdot \exp(-hc\nu_2/kT_{\mathrm{vib}})$, where g_1 is the statistical weight of the first level, h Planck's constant, c the speed of light, and k Boltzmann's constant. As a result of coupling of the two vibrations, the intensity of the hot band transitions can however be slightly different from the intensity of the ground state transition[31,32]. Furthermore the resolution of the measurements is not high enough to resolve the individual rotations in the Q bands, which may cause some errors in the determination of the band intensity. If this is taken into account the intensity ratio for the Q bands can be written as

$$I(Q_0)/I(Q_n) = C_n \cdot g_0/g_n \cdot \exp(nhc\nu_2/kT_{\mathrm{vib}}), \qquad (5.1)$$

where Q_n is the Q branch of ν_3 starting from the n$^{\mathrm{th}}$ level of ν_2 (see figure 5.19), and C_n

a correction factor that accounts for the coupling of the two vibrations and the effect of the limited resolution. Since the ν_2 transition is doubly degenerated, the statistical weights g_n follow the series[32]

$$g_n = (\ 1,2,3,...).\qquad\qquad (5.2)$$

c) Results

The factor C_1 was calibrated by measuring $I(Q_0)$ and $I(Q_1)$ without plasma as a function of pressure at room temperature (see figure 5.21). Using the known statistical weights g_0 and g_1 and assuming that in the absence of a plasma $T_{vib} = 300$ K at room temperature, (5.1) can be used to calculate C_1. C_1 appears to be 1.22, which means that the intensity is indeed only slightly influenced by the coupling of the vibrations. If we assume that this factor does not change when the plasma is created, we can calculate T_{vib} in the situation with plasma on from
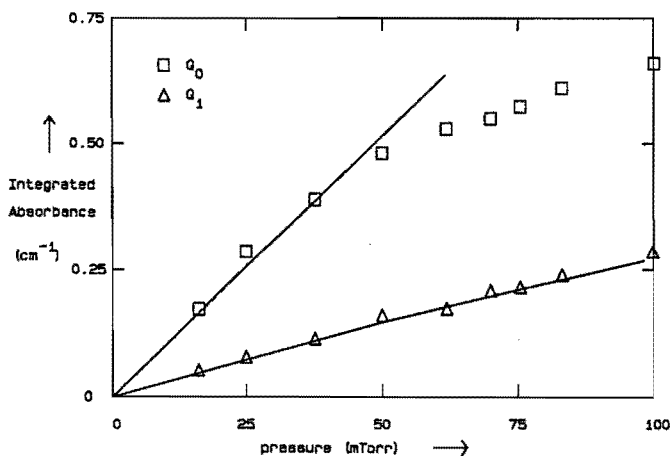

Fig. 5.21   *Calibration curve for relative intensities of the ground state Q branch (Q_0) and the first hot Q branch (Q_1). It follows that the Q_0–intensities are more or less linear with pressure up to $I(Q_0) = 0.5$, whereas $I(Q_1)$ is linear in the whole region investigated.*

$$T_{\mathrm{vib}} = \left[\ln\left[\frac{I(Q_0)/I(Q_1)|_{\mathrm{plasma\ on}}}{I(Q_0)/I(Q_1)|_{\mathrm{plasma\ off}}} \right] \cdot \frac{k}{h\nu_2} + \frac{1}{300} \right]^{-1} \tag{5.3}.$$

To determine the rotational temperature in the plasma, a simulation[33] of the shape of the P and R branches of the ν_3 band (corresponding to transitions with $\Delta J=-1$ and $\Delta J=+1$ respectively) was fitted to the shape of the experimental P and R branches shown in figure 5.20. The position of the rotational lines of the P and R branches of transitions from the ground state is approximately given by[32]

$$\nu(J) \approx \nu_0 - 2B_3(1-\zeta_3) \cdot J , \qquad\qquad \text{for the P branch, and}$$

$$\nu(J) \approx \nu_0 + 2B_3(1-\zeta_3) \cdot (J+1) , \qquad\qquad \text{for the R branch,} \tag{5.4}$$

where ν_0 is the band centre frequency, ζ_3 the Coriolis coupling factor for the ν_3 transition and B_3 the rotational constant given by[32]

$$B_3 = \frac{h}{8\pi^2 c I_{\mathrm{b}}} , \tag{5.5}$$

where h is Planck's constant, c the speed of light and I_{b} the moment of inertia of CF_4. The Coriolis coupling factor ζ_3 was taken from a measurement of the ν_3 band at 0.03 cm^{-1} unapodized resolution and was found to be 0.81 ± 0.02 in good agreement with literature values[31]. The intensities of a rotational line in the R branch with rotational quantum number J can be calculated from[32]

$$I(J) = (2J + 1)^2 \exp(-B_3 J(J+1)hc/kT_{\mathrm{rot}}) . \tag{5.6}$$

In the simulation also the hot bands are taken into account. The rotational temperature can be estimated by taking the best fit to the experimental P and R branches.

The plasma was operated at a pressure of 100 mTorr, 100 watt RF power (which corresponds to about 0.8 W/cm^2) and at several flows between 3 and 30 sccm CF_4. As a result of the presence of the plasma the relative intensities of the various Q branches changed considerably (see figure 5.20b). A more or less systematic value of 2.35 (independent of the flow) was found for the ratio $I(Q_0)/I(Q_1)$, which shows that the vibrational temperature increases after the plasma has been switched on. The value of T_{vib} in the plasma corresponding to this ratio depends on the spatial distribution of

T_{vib} (since the measurement only yields an average value over the line of sight of the infrared beam). To estimate this, a scan was made as a function of the radial position in the plasma. Unfortunately we were not able to measure beyond the edge of the electrodes, as a result of the shape of our vacuum windows. In the electrode region however we found no substantial change of $I(Q_0)/I(Q_1)$ with the lateral position. This means that if we take T_{vib} to have a value higher than without plasma only in the electrode region (about half of the optical path through the vacuum vessel), we can determine an upper limit for T_{vib}. This value appears to be 400 ± 20 K. This is relatively low compared to the value of 3000 K reported from emission data of N_2 in CF_4 obtained by van Veldhuizen et al.[30]. To understand this large difference we have to take into account that the vibrational temperature of the electronically excited level of N_2 need not be equal to the T_{vib} of the ground level of CF_4, since the upper level of N_2 may already be vibrationally excited during the electronic excitation (as a result of the Franck–Condon principle). In our case we measure directly the vibrational temperature of the (electronic) ground state. It seems therefore that the plasma has but a small influence on the vibrational temperature of CF_4. To make this plausible we have to look at the excitation and deexcitation processes involved. Vibrational excitation can result from several processes. The first of these processes is vibrational excitation through inelastic collisions with electrons. The mean frequency τ_{exc}^{-1} of excitation of a CF_4 particle is given by

$$\tau_{exc}^{-1} = \int_{\Delta\epsilon_{thr}}^{\infty} \sigma(\epsilon)\, f(\epsilon)\, \sqrt{\epsilon}\, d\epsilon \approx n_e\, \overline{\sigma}_{ev}\, \overline{v}_e \,, \tag{5.7}$$

where n_e is the electron density, $\overline{\sigma}_{ev}$ is the energy averaged cross–section for vibrational inelastic electron collisions, and $\overline{v}_e$ is the most probable electron velocity given by

$$\overline{v}_e = (\frac{2\ kT_e}{m_e})^{0.5} \,. \tag{5.8}$$

The collision cross–section σ_{ev} has been calculated as a function of the electron energy by Hayashi[34] who gives an energy averaged value of about $7 \cdot 10^{-21}$ m^{-2}. Taking $T_e = 4$ eV and $n_e = 1.3 \cdot 10^{16}$ m^{-3}, we find that $\tau_{exc}^{-1} = 150$ s^{-1}. Since for the calculation of $\overline{v}_e$ the whole EEDF has been taken into account whereas $f(\epsilon)\sigma(\epsilon)$ has a maximum below the maximum of the EEDF, (5.8) may be somewhat overestimated. The calculated excitation frequency can therefore be regarded as an upper limit. A second possibility for

the formation of vibrationally excited molecules is electron–ion recombination. In the case of CF_4 however this process can be neglected since the CF_4^+ ion is not stable and therefore too short lived to be able to recombine with an electron (in contrast to e.g. N_2, where N_2^+ is stable[35] and could possibly give a contribution to the formation of electronically excited and vibrationally hot molecules). Ion–ion recombination is possible in a CF_4 plasma but is dissociative, yielding therefore no excited CF_4 molecules. Finally vibrationally excited CF_4 molecules may be produced by sputtering of surface absorbed CF_4 as has been demonstrated for the case of SiO particles[36] (from a Si surface in an O_2 plasma). In the case of CF_4 however this process is negligible since the total number of ions impinging on the surface of the electrode per second (about $4 \cdot 10^{17}$ s⁻¹, which can be calculated from the etch rate of SiO_2 and the sputter yield[37] of SiO_2 by CF_x^+ ions) is smaller than the number of vibrationally excited CF_4 particles produced per second by electron impact (about $5 \cdot 10^{19}$ s⁻¹). Therefore in CF_4 direct excitation by collision with electrons is believed to be the main excitation mechanism for the creation of vibrationally excited CF_4 molecules.

The main deexcitation processes in this case are volume vibrational relaxation and diffusion of the excited molecules to the wall followed by deexcitation on the wall. The volume vibrational relaxation loss frequency can be estimated by

$$\tau_{\text{volume}}^{-1} = k_{\text{rel}} \, [CF_4] \, . \tag{5.9}$$

Estimating k_{rel} with the value that is known for CCl_4[38], i.e. $k_{\text{rel}} = 5 \cdot 10^{-13}$ m³s⁻¹, we get $\tau_{\text{volume}}^{-1} = 1.5 \cdot 10^3$ s⁻¹, which is an order of magnitude faster than the electron excitation process. The frequency of loss by wall deexcitation τ_{wall}^{-1}, using only the first mode of diffusion in a one–dimensional approximation is given by

$$\tau_{\text{wall}}^{-1} = \frac{\gamma D \pi^2}{d^2} \, , \tag{5.10}$$

where d is the electrode separation, D is the diffusion constant for vibrationally excited CF_4 (which is estimated to be appr. 1000 cm²/s at 100 mTorr) and γ is the deexcitation probability. This gives us a value of $\gamma \cdot 2.5 \cdot 10^3$ sec⁻¹ which is therefore faster than the excitation time constant if $\gamma \geq 0.06$. For high values of γ the wall deexcitation rate becomes comparable to the gas phase deexcitation rate. Since the excitation frequency is much smaller than the deexcitation frequency, no high densities of vibrationally excited molecules can build up and T_{vib} has a value only slightly above room temperature. The vibrational excitation of the ν_2 mode of CF_4 molecules in a capacitively coupled RF

plasma is therefore small.

From the shape of the P and R branch an estimate can be drawn for the rotational temperature T_{rot}. In figure 5.22 the results are shown of a simulation of the band shape of the P and R branches of the ν_3 band of CF_4 for a number of values of T_{vib} and T_{rot}. From the change in spectral distance between the maxima in the P and R branch (about 10 %) we estimate a T_{rot} of 350 ± 20 K for the plasma condition used.

It was found that the vibrational temperature of the ν_2 mode of CF_4 is $\leq$ 400 K in a plasma produced at 100 mTorr, 100 W and 20 sccm. This result may imply that only small effects are to be expected of the vibrational excitation on the EEDF and rate coefficients in a CF_4 plasma, and on the rate of formation of negative ions. It does however not exclude that other plasma species such as the dissociation products of CF_4 still can be vibrationally 'hot'. Furthermore the method used in this study has only yielded information on the vibrational excitation of the ν_2 mode, and it cannot be excluded that the other vibrational modes of CF_4 are vibrationally excited to a larger extent in the plasma than the ν_2 mode. As can be seen in table 5.2, all other modes have energy quanta larger than $h\nu_2$. The excitation cross sections of these modes due to electron impact may be much higher than the ν_2 cross section[38].
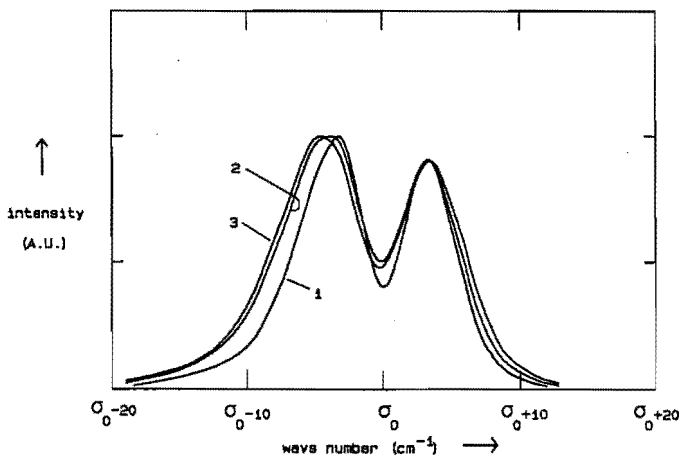

Fig. 5.22   Simulation of the overall shape of the P and R branch of the CF_4 ν_3 absorption band for three situations. Curve 1 shows the situation without plasma where $T_{vib} = T_{rot} = 300$ K. In curve 2, T_{vib} is 400 K and T_{rot} is 350 K. In curve 3, $T_{vib} = T_{rot} = 400$ K. Using the estimated value $T_{vib} = 400$ K in the plasma the 10 % shift in the distance between the P and R branch maxima observed in figure 5.20 is obtained at $T_{rot} = 350$ K.

5.2.3. Densities of neutrals in the plasma

Absorption spectra of CF_2, CF_4 and C_2F_6 in fluorocarbon plasmas were determined at 1 cm^{-1} resolution. This choice was made because for these molecules it was impossible to resolve the individual rotational lines separately with our maximum resolution of 0.015 cm^{-1}. As a result of this it was not possible to determine CF_3 densities since the overall band structure of CF_3 (ν_3, at 1261 cm^{-1}) overlaps with strong absorption bands of both CF_4 (ν_3, at 1283 cm^{-1}) and C_2F_6 (ν_7, at 1250 cm^{-1}). The C_2F_6 density measurement was calibrated by a separate measurement using C_2F_6 gas at a known pressure in the vacuum system and measurement of the integrated absorbance of the 1250 cm^{-1} band. For the measurement of CF_2 radical densities such a calibration is not possible. Therefore we have calculated the absolute density of CF_2 from the integrated absorbance using literature values calculated using the polar tensor method, i.e. 250 ± 50 km·mol^{-1}, for the integrated molar absorption coefficient[39,40].

a) Measurement of the CF_2 density in a CF_4 plasma

To increase the sensitivity for the measurement of CF_2, the absorption length in the plasma was enlarged using the multipass–cell depicted in figure 4.11. To sufficiently lower the detection limit, a large number of interferograms were averaged (1200). Only then the absorbance of the ν_3 band of CF_2 was measurable. A measurement of the absorption spectrum of a CF_4 plasma was performed at 100 mTorr pressure, 50 sccm flow, and 80 watt RF power (see figure 5.23). Since at the low resolution used in the experiment the separate rotational lines are not resolved, we see a combined effect of the absorption of CF_2 (ν_3 = 1114 cm^{-1}), C_2F_6 (ν_5 = 1115 cm^{-1}) and a small amount of CHF_3 impurities (possibly coming from a wall reaction of CF_x radicals with hydrogen, at ν_3 = 1150 cm^{-1}). To remove the effect of these disturbing stable molecules, spectra of C_2F_6 gas and of CHF_3 gas were determined and subtracted (by trial and error) from the original one. This yields a spectrum that more clearly shows the spectral features of CF_2 known from the literature[41,42], e.g. the band center at 1114 cm^{-1} and the maximum of the R branch at 1126 cm^{-1}. The resulting spectrum along with a literature spectrum[41] is depicted in figure 5.24 in which these features can be easily recognized. The density of CF_2 in this situation at 100 mTorr, 50 sccm flow and 80 watt RF power was found to be $(10 \pm 4) \cdot 10^{18}$ m^{-3}. The values of $[C_2F_6]$ and $[CHF_3]$ that were used to correct the spectrum shown in figure 5.23 are $(2.5 \pm 0.5) \cdot 10^{18}$ m^{-3} and $(7 \pm 2) \cdot 10^{18}$ m^{-3} respectively.

In section 3.2.2 a simulation of the neutral particle kinetics was described. The measured value of $[CF_2]$ should be compared with the results of a simulation carried out
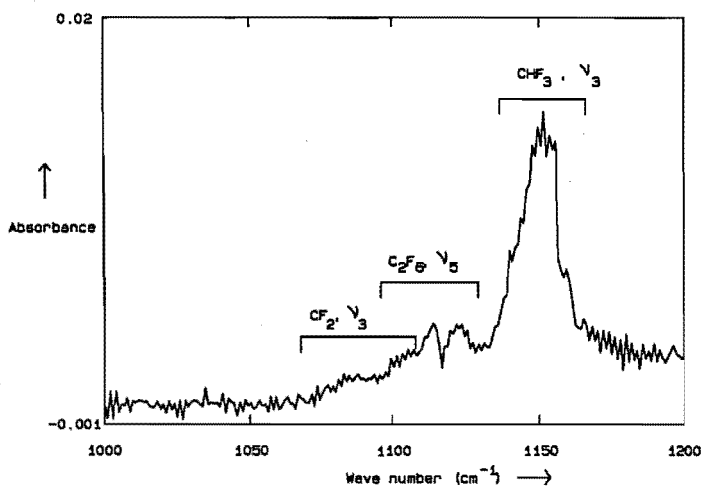
Fig. 5.23   *The absorption spectrum of a CF_4 plasma at 1 cm^{-1} resolution in the region of the CF_2 ν_3 absorption band at 100 mTorr, 50 sccm, 80 watt RF power. The CF_2 band overlaps in part with bands of C_2F_6 and CHF_3 impurities.*
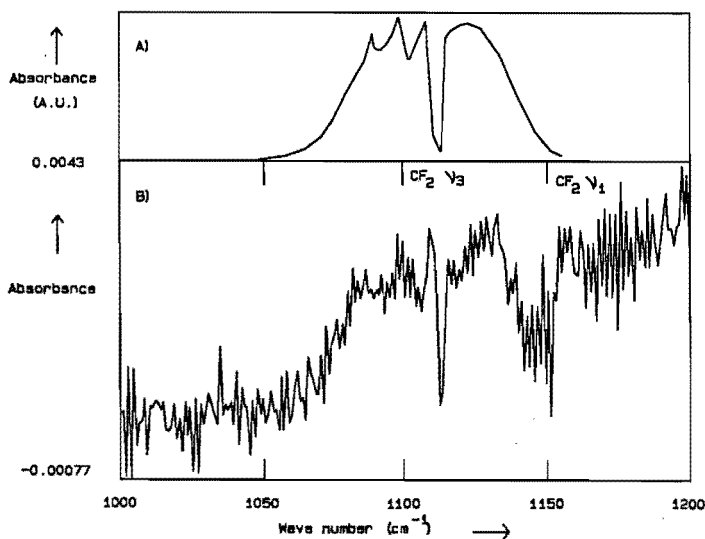

Fig. 5.24   *The absorption spectrum of the CF_4 plasma after correction for the absorption bands of C_2F_6 and CHF_3. The measured band shape (B) is identical to the one reported in the literature[41] (A).*

for 100 mTorr, 50 sccm and 80 watt.

In tables 3.1 and 3.2 it is shown that production of CF_2 is mainly due to direct dissociation of CF_4 by electrons

(2) $CF_4 + e \longrightarrow CF_2 + 2F + e$

whereas the loss is mainly due to heterogeneous losses

(16) $CF_2 \longrightarrow CF_{2(s)}$ $\hspace{4cm}$ $s(CF_2) = 0.06$

Since the electron densities and the sticking coefficient of CF_2 are known[43] the steady–state density from the simulation only depends on the rate coefficient of the production process k_2. For $k_2 = 3.5 \cdot 10^{-16}$ m^3s^{-1}, the simulation yields the same value for the CF_2 density as the experiment. This value of k_2 is 1.5 times the value that was used by Ryan et al.[44]. The agreement with their results is therefore reasonably good, despite the differences in circumstances. Since their value is based on an characteristic electron energy v_e of 5 eV, the difference may indicate that v_e is slightly higher than 5 eV and/or the shape of the EEDF is closer to a Maxwellian than was accounted for by Ryan et
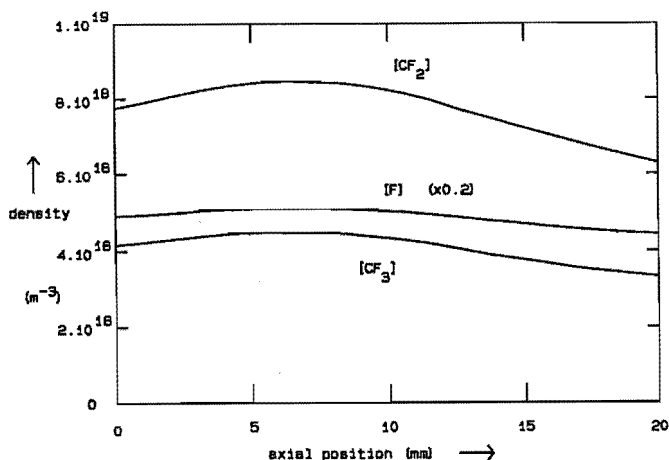
Fig. 5.25   *Simulated densities of CF_2, CF_3 and fluorine as a function of the axial position z in the plasma at 100 mTorr, 50 sccm and 80 watt. The sticking coefficient for CF_3 was taken to be 0.035. The grounded electrode is situated at z=0. It can be seen that the densities decrease at the surfaces due to heterogeneous loss processes.*

al.[44].

The fact that CF_2 is lost on the walls can be seen in figure 5.25 where also the calculated axial distributions of $[CF_3]$ and $[F]$ is shown. To solve the equations for $[CF_3]$ and $[F]$, it has been assumed that $s(F) = 0.002$ and $s(CF_3) = 0.035$. The density profiles are somewhat asymmetric due to the asymmetric electron density distribution. The fact that the fluorine atom density profile also decreases slightly at the wall reflects that fluorine is also lost at the surface due to surface recombination with CF_x radicals.

b) Measurement of the density of C_2F_6 in a CF_4 plasma

Volume production of C_2F_6 in a CF_4 plasma is due to 3–particle recombination of two CF_3 radicals

(5) $CF_3 + CF_3 (+ CF_4) \longrightarrow C_2F_6 (+ CF_4).$ $k_5 = 4 \cdot 10^{-18} \text{ m}^3\text{s}^{-1}$
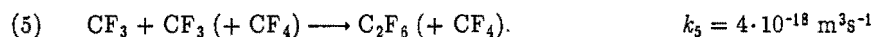
C_2F_6 is lost by gas flow and by electron induced dissociation and attachment

(9) $C_2F_6 + e \longrightarrow X + F + e$ $k_9 = 2 \cdot 10^{-16} \text{ m}^3\text{s}^{-1}$
(11) $C_2F_6 + e \longrightarrow X + F^-$ $k_{11} = 5 \cdot 10^{-16} \text{ m}^3\text{s}^{-1}$
(12) $C_2F_6 + e \longrightarrow CF_3 + CF_3 + e$ $k_{12} = 2 \cdot 10^{-16} \text{ m}^3\text{s}^{-1}$

The nature of the products X determines whether (9) and (11) are effective loss processes for C_2F_6. If X = C_2F_5, most of it will recombine with fluorine to form C_2F_6 again. If X = $CF_2 + CF_3$, reactions (9) and (11) are effective loss processes.

Since C_2F_6 is formed by recombination of CF_3 radicals, it is an indirect measure of the CF_3 density. CF_3 is mainly produced by electron induced dissociation of CF_4 and attachment to CF_4 and by dissociative ion–ion recombination

(1) $CF_4 + e \longrightarrow CF_3 + F + e$ $k_1 = 1.5 \cdot 10^{-16} \text{ m}^3\text{s}^{-1}$
(3) $CF_4 + e \longrightarrow CF_3 + F^-$ $k_3 = 4 \cdot 10^{-17} \text{ m}^3\text{s}^{-1}$
(10) $CF_3^+ + F^- \longrightarrow CF_3 + F$ $k_{10} = 5 \cdot 10^{-13} \text{ m}^3\text{s}^{-1}$

Of these three reactions, (1) is most important, and (10) contributes about 25 % at 100 mTorr and 80 Watt. CF_3 is lost mainly by gas phase recombination with itself and (mainly) with fluorine and heterogeneous loss

(15) CF$_3$ $\longrightarrow$ CF$_{3(s)}$ $\qquad$ $s(\mathrm{CF}_3) = ?$

Since the sticking probability $s(\mathrm{CF}_3)$ of CF$_3$ is less known than the other parameters in the simulation, the density of C$_2$F$_6$ was tuned using this coefficient (see section 3.2). This has no significant influence on the previously mentioned fit of the CF$_2$ density since the density of CF$_3$ (and therefore the density of C$_2$F$_6$) is only weakly coupled to the density of CF$_2$, as can be seen in table 5.3. The same procedure was also used by Edelson et al.[29] but they used the electron density to fit the simulation to the experiment. In our case we know the electron density and can get therefore use an other parameter. Some results of the simulation as a function of $s(\mathrm{CF}_3)$ are also given in table 5.3. Only a small sticking probability of CF$_3$ is needed to explain the observed density of C$_2$F$_6$ if we use the rate coefficients given in table 3.1, and therefore in this case it can be concluded that the main loss process for CF$_3$ is recombination with F in the gas phase. In this situation we can see from table 5.3 that the simulation yields the same value for [C$_2$F$_6$] as the experiment if we take $s(\mathrm{CF}_3)$ to be 0.035.

$\qquad$ Measurements of the C$_2$F$_6$ density as a function of gas flow and pressure are shown in figures 5.26 and 5.27. The results indicate that the C$_2$F$_6$ density is inversely proportional to the flow and proportional to the pressure. In figure 5.26 are also included two simulated dependencies of the C$_2$F$_6$ density as a function of flow, one in which the product X of reactions (9) and (11) is taken to C$_2$F$_5$ and one in which the product is taken to be CF$_2$ + CF$_3$. It appears from figure 5.26 that a good fit between the experimental and simulated flow dependence can be obtained when X is expected to be C$_2$F$_5$, which almost totally recombines with a fluorine radical to form C$_2$F$_6$. Therefore

Table 5.3 *Radially averaged C$_2$F$_6$ and CF$_2$ densities as a function of the sticking coefficient of CF$_3$ in a 100 mTorr ,50 sccm and 80 W CF$_4$ plasma obtained by simulation.*

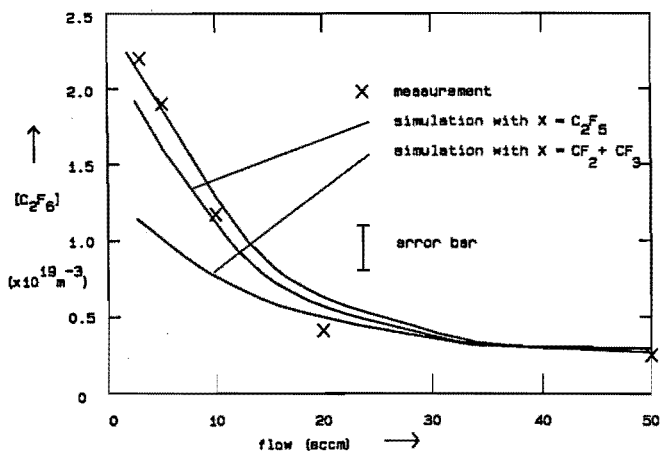| Setting	[C$_2$F$_6$] (m^{-3})	[CF$_2$] (m^{-3})	[CF$_3$] (m^{-3})
Experiment	$(2.5\pm0.5)\cdot10^{18}$	$(10\pm4)\cdot10^{18}$	?
$s(\mathrm{CF}_3) = 0.002$	$4.1\cdot10^{18}$	$9.6\cdot10^{18}$	$6.1\cdot10^{18}$
$s(\mathrm{CF}_3) = 0.02$	$3.1\cdot10^{18}$	$9.6\cdot10^{18}$	$5.4\cdot10^{18}$
$s(\mathrm{CF}_3) = 0.035$	$2.5\cdot10^{18}$	$9.6\cdot10^{18}$	$4.9\cdot10^{18}$
$s(\mathrm{CF}_3) = 0.05$	$2.1\cdot10^{18}$	$9.6\cdot10^{18}$	$4.5\cdot10^{18}$

Fig. 5.26   The measured density of C_2F_6 as a function of the gas flow at 100 mTorr
             and 80 W RF power. Also included are two simulated dependencies, one in
             which the product X of dissociation and attachment of C_2F_6 (see text) is
             C_2F_5 and one in which the products are CF_2 and CF_3. It follows from these
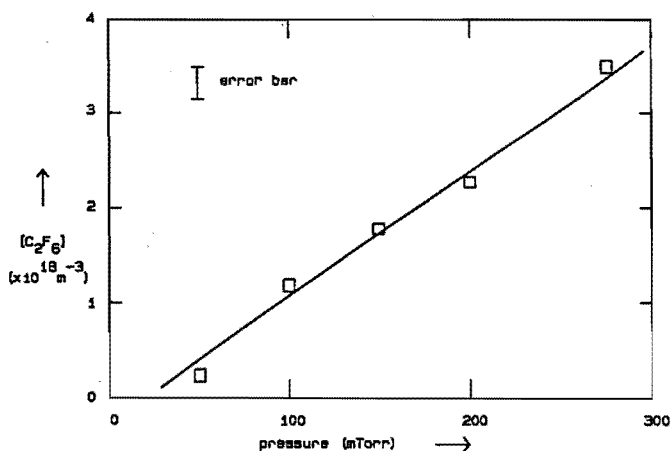   curves that gas flow is the major loss process for C_2F_6.

Fig. 5.27   The measured density of C_2F_6 as a function of the gas pressure at 10 sccm
             flow and 80 watt RF power. It follows from this curve and from figure 5.26
             that the density of CF_3 radicals must be almost constant with pressure.

the experimentally observed decrease in the C_2F_6 density with increasing flow implies that flow is the major loss mechanism for C_2F_6 in the plasma.

c) Density analysis of CF_3 from the observed densities of C_2F_6 in a CF_4 plasma.

Since the gas flow loss of C_2F_6 can be calculated accurately and C_2F_6 is produced by recombination of CF_3 radicals, the CF_3 radical density can be directly related to the C_2F_6 density. The pressure dependence at constant flow suggests that the production rate of C_2F_6 is more or less constant with pressure (at constant flow the residence time of the gas is proportional to the pressure). Since the rate coefficient for 3–particle recombination of CF_3 with itself is constant in this pressure range[45] the CF_3 density must be approximately constant with pressure in the investigated range. To see if it is possible to draw conclusions from this constancy of the CF_3 density with pressure we must take a closer look at the production and loss processes of CF_3 radicals.

CF_3 is mainly produced by the reactions (1) and (3). The production can therefore be described by

$$\left.\frac{\partial [CF_3]}{\partial t}\right|_{prod} = (k_1 + k_3) \cdot [CF_4] \cdot n_e \tag{5.11}$$

Since n_e is known to be roughly inversely proportional to pressure above 100 mTorr (see section 5.3), the product of n_e with $[CF_4]$ is roughly constant with pressure. Hence, the pressure dependence of the production of CF_3 mostly depends on the pressure dependence of k_1 and k_3. Since T_e decreases slightly with pressure, we can expect that the production rate slowly decreases with pressure.

If loss of CF_3 would occur mainly in the gas phase, due to recombination with fluorine, the loss would increase with pressure due to the fact that $[F]$ increases with pressure[19]. The reason for the increase of $[F]$ with pressure is obvious; in a steady state situation the amount of fluorine leaving the plasma region must balance the amounts of C_2F_6, CF_2 and CF_3 that leave that region in such a way that the total C/F ratio is equal to $\frac{1}{4}$. In this situation we would expect a decrease of the CF_3 density with pressure. Since the measurement suggests that $[CF_3]$ is roughly constant with pressure, it is concluded that other loss mechanisms may play a role.

If on the other hand loss of CF_3 at the walls would be the major loss process for CF_3, the loss would at higher pressures be diffusion limited. Therefore the loss rate would decrease with pressure and we would expect a slow increase of the radical density with pressure. For the CF_2 radical in a CF_4 plasma, where surface loss is dominant, this

has e.g. been measured by Booth et al.[43].

The fact that $[CF_3]$ seems to be constant with pressure may therefore indicate that in the investigated pressure range both gas phase recombination and surface loss are important. This then means that the estimate for $s(CF_3)$ (i.e. 0.035) must be too low. However, if $s(CF_3)$ is taken to be higher, the total loss rate becomes higher than is accounted for in the simulation. To still get the same value for $[CF_3]$ and therefore for $[C_2F_6]$, the rate coefficient for production must then be higher than is given in table 3.1.

Since it has up till now only been possible to derive the density of CF_3 indirectly, through the C_2F_6 density, we can get only an estimate of the CF_3 density. It is however difficult to analyze the kinetics of CF_3 quantitatively. *In situ* density measurements (e.g. IR absorption using a diode laser) of CF_3 will be necessary for this purpose.

d) Effects of polymerization on the particle kinetics

In the model the radicals that stick to the surface are assumed to react with fluorine radicals from the gas phase. To demonstrate what happens if on one of the electrodes all CF_x radicals react at the surface and are converted into a polymer layer

$$CF_x + C_yF_{z(s)} \longrightarrow C_{y+1}F_{z+x\ (s)}$$

a simulation was performed in a situation at 100 mTorr, 3 sccm flow and 80 watt RF power. The results are given in table 5.4. It shows that the major loss process for fluorine in the plasma is also a wall process, i.e. surface recombination. The values for

Table 5.4   *Simulated densities of F, CF_3, CF_2 and C_2F_6 (in m^{-3}) in a situation where all CF_x radicals that stick to the surface recombine with fluorine at the surface, and in the situation where on one of the electrodes the CF_x radicals form a $[CF_x]_n$ layer. The CF_4 plasma is produced at 100 mTorr, 3 sccm and 80 W, and the rate coefficients and sticking coefficients of table 3.1 and 3.2 were used. Note the large difference in [F] between the two situations.*

Setting	$[C_2F_6]$	$[CF_2]$	$[CF_3]$	[F]
recombination	$1.8 \cdot 10^{19}$	$9.6 \cdot 10^{18}$	$4.2 \cdot 10^{18}$	$5.8 \cdot 10^{19}$
polymerization	$2.7 \cdot 10^{18}$	$7.4 \cdot 10^{18}$	$1.5 \cdot 10^{18}$	$3.4 \cdot 10^{20}$

[F] obtained in the situation without polymerization agree well with an estimate of $\approx 10^{19}$ m^{-3} at 100 mTorr, 20 watt and 20 sccm from the absolute emission of fluorine as previously measured by Bisschops[19] in the cavity configuration.

e) Measurements of the densities of CF$_4$ and C$_2$F$_6$ in a CHF$_3$ plasma

Measurements of the densities of CF$_4$ and C$_2$F$_6$ as a function of flow and pressure were also performed in plasmas of CHF$_3$. The results are presented in figures 5.28 and 5.29. Using similar arguments as in the case of CF$_4$, we can assume that flow is the major loss process for both C$_2$F$_6$ and CF$_4$. Assuming again that C$_2$F$_6$ is formed by recombination of CF$_3$ radicals, the approximately linear dependence of [C$_2$F$_6$] on pressure then shows that the CF$_3$ density is approximately constant with pressure in the investigated pressure range. The linear dependence of [CF$_4$] on the pressure then indicates that [F] is also roughly constant with pressure. At 100 mTorr, 10 sccm and 80 watt the C$_2$F$_6$ density is roughly 18 times higher than in the case of a CF$_4$ plasma at the same condition. If we assume that the loss processes for C$_2$F$_6$ in a CHF$_3$ plasma are comparable to those in a CF$_4$ plasma (this is justified since the flow is the same and also the electron densities are of the same order of magnitude as in CF$_4$, see section 5.3), we can estimate [CF$_3$] in a CHF$_3$ plasma from a comparison of the C$_2$F$_6$ densities in CF$_4$
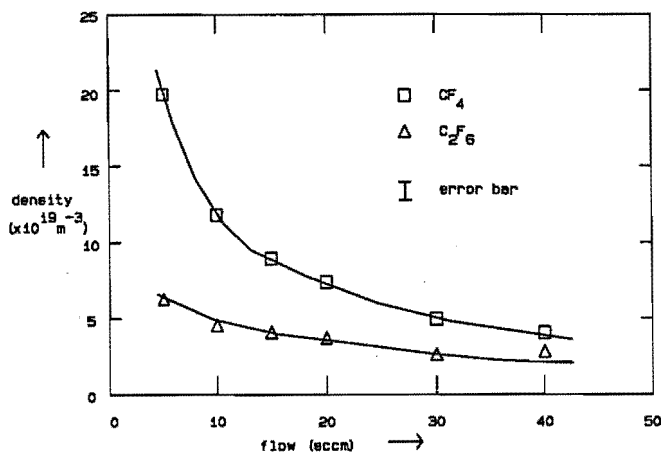

Fig. 5.28   *The measured densities of CF$_4$ and C$_2$F$_6$ in a CHF$_3$ plasma as a function of the gas flow at 100 mTorr pressure and 80 watt RF power. From a comparison between this measurement and the results in CF$_4$ plasmas, it is possible to estimate the densities of F and CF$_3$ in this plasma*
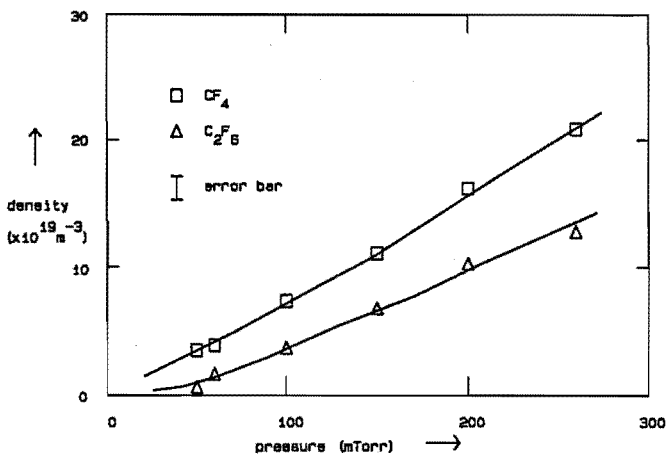
Fig. 5.29   The measured densities of CF_4 and C_2F_6 in a CHF_3 plasma as a function
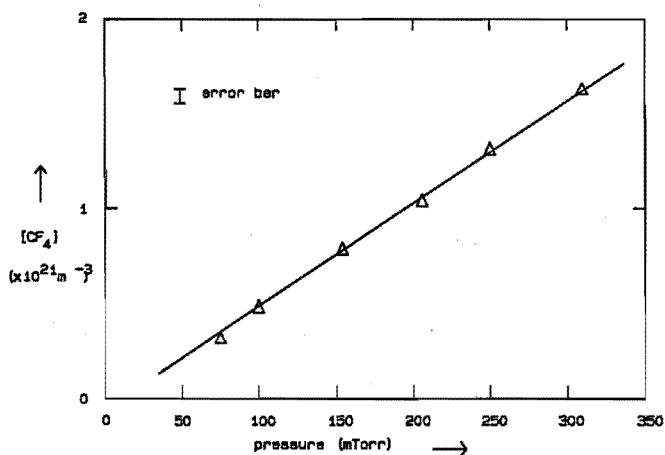of the gas pressure at 80 watt RF power and 20 sccm flow.

Fig. 5.30   The measured density of CF_4 in a C_2F_6 plasma as a function of the gas
pressure at 80 watt RF power and 20 sccm flow. A relatively large
fraction of the feed gas is converted into CF_4.

and CHF_3 plasmas. Since the production rate of C_2F_6 is dependent on the square of the CF_3 density, the CF_3 density is estimated to be about $\sqrt{18}$ times higher than in CF_4 plasmas, i.e. $2.1 \cdot 10^{19}$ m^{-3} at this condition. Using this estimate and the CF_4 density in the plasma at the same condition, and using the rate coefficients in table 3.1, we can in a similar way derive that the fluorine density is in this case about $1.8 \cdot 10^{19}$ m^{-3}. The density of CF_2 is not known in this case. This clearly shows that the density of CF_x radicals in the plasma is higher in the case of CHF_3 than in the case of CF_4, and therefore the CF_x radical fluxes that are responsible for the formation of an inhibiting polymer layer are also higher in CHF_3, whereas the density of fluorine radicals that can etch the polymer is much lower. Higher deposition rates of polymers can therefore be expected, in agreement (see section 5.1) with the observed etching characteristics.

f) Density of CF_4 in a C_2F_6 plasma

In figure 5.30 a measurement of the CF_4 density in a C_2F_6 plasma as a function of the gas pressure is given. Since the reaction of CF_3 with fluorine is much faster than the reaction of CF_3 with itself, high densities of CF_4 up to 10 % of the feed gas density build up in the plasma. However, since CF_4 is formed through a reaction between two different particles (i.e. F and CF_3) it is not possible to estimate radical densities from these values in plasmas of C_2F_6.

5.2.4 Conclusions

It has been shown that infrared absorption spectroscopy can be used to investigate the vibrational excitation of CF_4 in a CF_4 plasma. The excitation of the ν_2 mode of CF_4 was studied and was found to change only slightly when a plasma is created. If the same applies to other vibrational modes this means that in RF CF_4 plasmas vibrational excitation may be an unimportant factor for the production process of negative ions by dissociative attachment in contrast to the case of H_2 and HCl plasmas where this has been reported to be very important[27,28].

Moreover this technique can be successfully applied to measure the absolute densities of neutral species in the plasma. Densities of CF_2 radicals and C_2F_6 molecules in plasmas of CF_4 were measured. Through use of the model presented in section 3.1 it was also possible to make an estimate of the CF_3 density in the plasma from these densities. From a comparison between the simulated and experimentally determined densities of CF_2, it was found that the rate coefficients reported in the literature are close to the values that are needed to explain the observed density of CF_2 in a CF_4

plasma. This means that the electron temperature T_e has a value around 4 eV, in reasonable agreement with the values that are commonly reported. From a comparison of the densities of C_2F_6 in CF_4 and CHF_3 plasmas it was found that the CF_3 density is much higher in CHF_3, in agreement with the observed surface phenomena shown in section 5.1.

5.3 Charged particles in the plasma

5.3.1. Introduction

In the chemically active plasmas studied in this work the reactive particles are created by energetic electrons. Therefore knowledge of the density and energy distribution of these electrons is needed for a fundamental understanding of the processes taking place in the plasma. Quantitative measurements of the electron density have been carried out in a number of fluorocarbon plasmas using the microwave method described in section 4.3. The results are shown in section 5.3.2.

Moreover, to study the densities and composition of negative ions present in the plasma, quantitative measurements of the negative ion densities in these plasmas were performed using the photodetachment effect. Experimental results will be given for RF plasmas of CF_4, C_2F_6, CHF_3 and C_3F_8 as a function of macroscopic plasma parameters and as a function of the position in the plasma. The results are also given in section 5.3.2 and compared with results from the fluid model calculation described in section 3.3. Moreover, from the ratio of the negative ion density and the electron density the behavior of the electron temperature with the macroscopic plasma parameters will be estimated.

Since in the modeling a number of reaction coefficients are not well known, time–resolved density measurements for both electrons and negative ions were carried out in the afterglow of a CF_4 plasma to obtain these coefficients, using the afterglow model described in section 3.3. The results of these experiments are given in section 5.3.3. Furthermore, the importance of some production and loss processes for negative ions in the plasma are investigated and discussed.

5.3.2 Densities of n_e and n^- in the plasma

a) Electron densities

In figure 4.12 an example of the shift of the resonance frequency, due to the presence of a plasma, is given. From these curves, the electron density has been determined in plasmas of CF_4, C_2F_6, C_3F_8 and CHF_3 at several pressures and RF powers (see figures 5.31 and 5.32). It can be clearly seen in figure 5.31 that in a CF_4 plasma the electron density as a function of pressure shows a maximum at around 50 mTorr (using 20 watt RF power). This maximum is relatively sharp in the case of CF_4, in contrast to the curves for C_2F_6 and C_3F_8. The maximum in the CF_4 curve almost
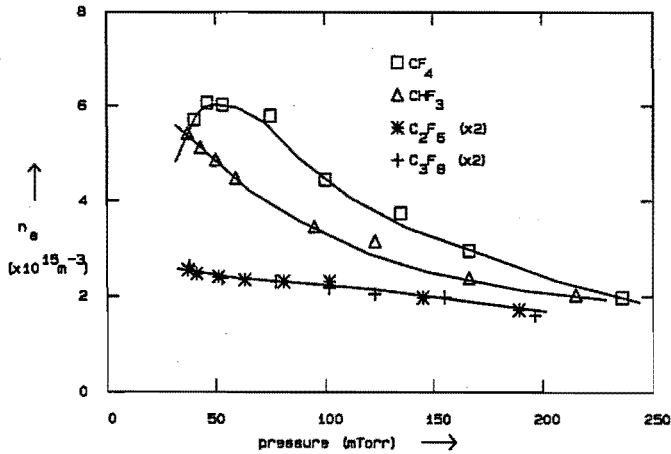
Fig. 5.31   The pressure dependence of the electron density in RF plasmas in CF_4, CHF_3, C_2F_6 and C_3F_8. The RF power is 20 watt and the gas flow is 20 sccm. It is clear from this figure that the electron densities are lower in gases with a high cross section for dissociative attachment.
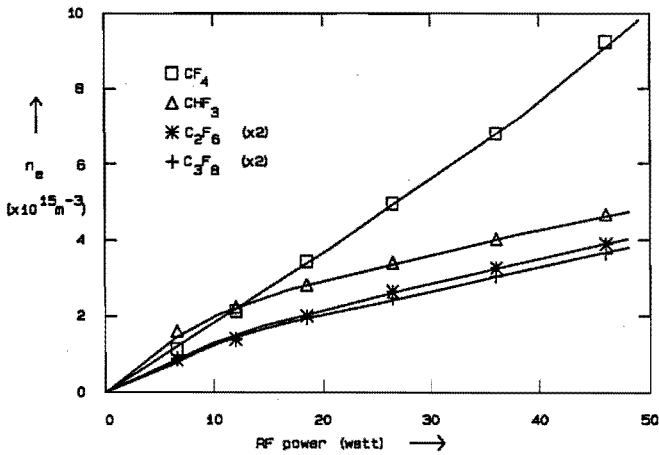

Fig. 5.32   RF power dependence of the electron density in plasmas in CF_4, CHF_3, C_2F_6 and C_3F_8 at a pressure of 120 mTorr and a gas flow of 20 sccm.
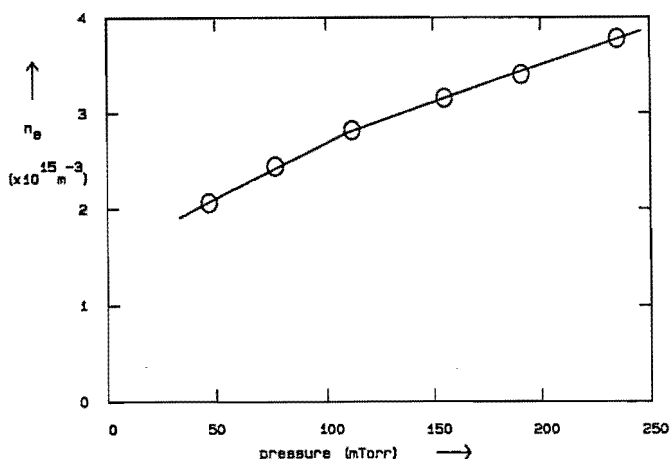
Fig. 5.33   The absolute electron density in an Ar plasma as a function of pressure at
3 watt RF power and 20 sccm flow. In contrast to the measurements in
the plasmas of electronegative gases the electron density does not decrease
at higher pressure. This suggests that negative ion formation may be a
cause for the decrease of n_e in electronegative gases.

coincides with the maximum of the (ion–induced) etch rate of SiO_2 (see section 5.1). If
we compare the previously measured value of the volume averaged electron density by
de Vries et al.[37] with the electron density found in this study as a function of RF power
(at 120 mTorr) we find that they are almost equal.

An interesting feature is that the electron densities in CF_4 and CHF_3 at lower
pressures are up to 6 times higher than the electron densities in C_2F_6 and C_3F_8 at the
same RF power. Moreover the electron densities in CF_4 and CHF_3 decrease dramatically
at higher pressures, whereas the electron densities in C_2F_6 and C_3F_8 drop only slowly.

In order to explain these phenomena we have to take into account that in CF_4
the formation of negative ions through dissociative attachment (which may lower the
electron density) is slower than in C_2F_6. The latter is shown by values of dissociative
attachment rates given by Hunter and Christophorou[46], who found that at the same
electron temperature (assuming an effective average T_e of 3–5 eV) the attachment rate
for C_2F_6 is 10–80 times larger than for CF_4. To investigate this trend of a higher n_e in
gases with a lower cross section for dissociative attachment, the electron density was
also measured in an Ar plasma (without any attachment) as a function of pressure (see
figure 5.33). It shows that in Ar plasmas the electron density is even higher than in CF_4,

Table 5.5   *Simulation of the effect of the attachment coefficient on the electron and*
                 ion densities in the in the center of the plasma. The simulation was run at
                 a pressure of 200 mTorr and an RF power of 20 watt.

attachment coefficient	n_e (m^{-3})	n^+ (m^{-3})	n^- (m^{-3})
k_a	$1.29 \cdot 10^{15}$	$2.07 \cdot 10^{16}$	$1.94 \cdot 10^{16}$
$\frac{1}{2}k_a$	$1.51 \cdot 10^{15}$	$1.28 \cdot 10^{16}$	$1.13 \cdot 10^{16}$

especially at high pressures. Furthermore no decrease of n_e with pressure is found in Ar. This suggests that negative ion formation is a cause for the decrease of n_e with pressure in the electronegative gases. To investigate the influence of the attachment coefficient on the charged particle densities, the numerical simulation described in section 3.3.2 was performed for two situations, one in which the normal attachment coefficient as given by Hunter et al.[54] was used, and one in which the values of this coefficient as a function of the reduced electric field E/N were divided by 2. The results in these two cases are given in table 5.5. It is clear from this table that the simulation confirms the findings of the experiment, i.e. a lowering of the electron density with increasing attachment coefficient of the feed gas.

Another aspect that may be important is that in C_2F_6 and CHF_3 plasmas CF_4 molecules are formed through recombination of CF_3 and F radicals (see section 5.2). The CF_4 density in these plasmas is more or less linear with pressure and power and decreases with the flow. This density can be up to more than 10% of the main gas. Since the ionization rate is different for CF_4 versus C_2F_6 and CHF_3, this may have some effect on the pressure dependence of n_e in C_2F_6 and CHF_3 plasmas.

Finally, in these molecular gases part of the power input is used for the production of vibrationally excited molecules, which are subsequently deexcited at the walls or relaxated in collisions with other molecules in the gas phase. Therefore at the same power input less power is available for the production of ions and electrons. Hence the densities of charged particles will decrease as the feed molecule gets more complex, since in that case more and more vibrational modes are becoming available to dissipate (part of) the RF power. As an example, excitation of the ν_2 mode has been shown for the case of CF_4 in section 5.2.2.

At the moment it is not possible to indicate which of the given possibilities is most important for the explanation of the phenomena mentioned above. However, both the experimental and theoretical results suggest that in plasmas of gases that have a

high attachment rate coefficient the electron densities are lower than in gases with a low attachment coefficient.

b) Attribution of the photo–induced production of electrons to photodetachment

In figure 4.17 an example was given of the photon–induced production of extra electrons in a CF_4 discharge. To be sure that these extra electrons can be attributed exclusively to photodetachment of negative ions, other photon–induced effect must be excluded. Possible other processes for photo–induced production of extra electrons are photo–electric effects and photo–ionization from long lived excited states.

To exclude these other photon–induced effects, first of all some test experiments have been performed.

Firstly, an experiment was performed in an argon plasma at 100 mTorr, 20 sccm and 20 watt. In this situation, in the absence of an electronegative feed gas, only a very weak signal close to the noise limit was detected. This suggests that photoionization of long lived excited states, which will certainly be present in an argon plasma[47], do not contribute significantly to the production of extra electrons by the laser pulse.

Secondly, the axial profile of the extra electron density was determined using a 1 mm diaphragm to restrict the laserbeam. Therefore it was possible to make an axial scan of the distribution of the species that produce the extra electrons. The results are depicted in figure 5.34. The extra electron density is observed to drop sharply in the sheath region of the plasma. This can be understood only when the extra electrons are generated either by a neutral species generated in the glow that has a very short lifetime, or by a species that is strongly confined in the glow region of the plasma. Concerning the first possibility, any neutral species which has a density high enough to release a detectable amount of photo–electrons should have a long lifetime, and such a neutral species would live long enough to diffuse into the sheath region. Therefore the second possibility is more probable. Because the glow is charged positively, only negative ions are trapped in the glow. The measured signal must therefore result from the photodetachment of negative ions.

Thirdly, a measurement was performed in the afterglow of a CF_4 plasma at 110 mTorr. The evolution of the electron density jump was measured as a function of the time between plasma switch–off and the start of the laser pulse. The time dependence was measured with a) the beam going through the glow region and with b) the beam going through the sheath region of the plasma. The results are depicted in figure 5.35. It shows that in the glow region the density of the extra electrons decreases with the time
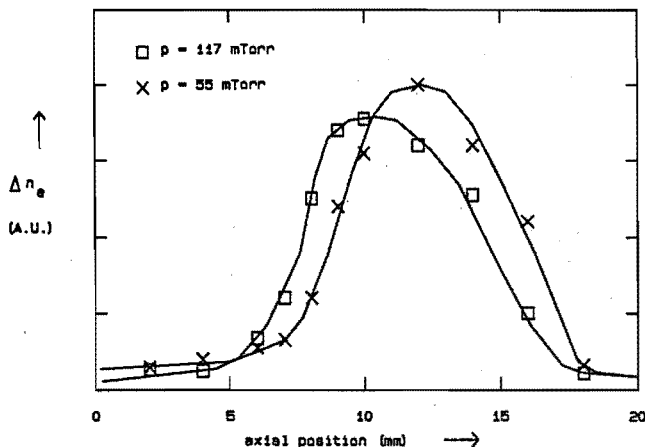
Fig. 5.34   Density of photodetached electrons as a function of the spatial position. It
is evident that the density sharply decreases at the sheath boundary,
indicating that the particles that produce these electrons are either instable
or repelled by the electric field in the sheath.

gap between plasma switch–off and the laser pulse. In the sheath region however we see
temporally a small increase in the extra electron density only after about 50 μs. This
behavior can be expected from negative ions: the sheath potential vanishes after plasma
switch–off and negative ions start to diffuse out towards the electrodes and they reach
the irradiated volume 50 μs after the switch–off of the plasma. If it is assumed that
photo–ionization of long lived excited states is responsible for the observed release of
extra electrons, this behavior cannot be explained.

        Finally, the dependence of the extra electron density on the wavelength of the
light pulse was determined (corrected for the laser pulse energy. Since the intensity of
the dye laser is smaller than that of the Nd–YAG laser alone, the photo–induced effect
does not saturate. This means that the number of extra electrons reflects the total cross
section for the production process of the extra electrons. The results in plasmas of CF_4
and C_2F_6 at 100 mTorr gas pressure and 10 watt RF power are shown in figure 5.36. In
the case of CF_4, at about 365 nm the number of extra electron drops sharply to a value
below the noise limit of the method. This agrees well with the maximum wavelength for
the photodetachment of F^- as measured by Vacquie et al.[48], who in fact found a value of
365 nm. This clearly shows that most of the signal in the case of CF_4 comes from the
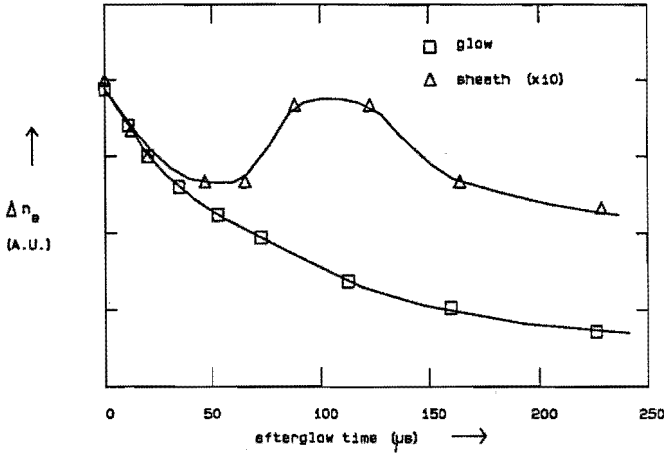
Fig. 5.35   The extra electron density in the afterglow of a CF_4 plasma as a function of the time between plasma switch−off and the firing of the laser in a) the glow of the plasma and in b) the sheath region. The densities have been normalized with respect to the initial density. The increase of the extra electron density in the sheath region indicates that negative ions start to diffuse out of the glow some time after the plasma is switched off.
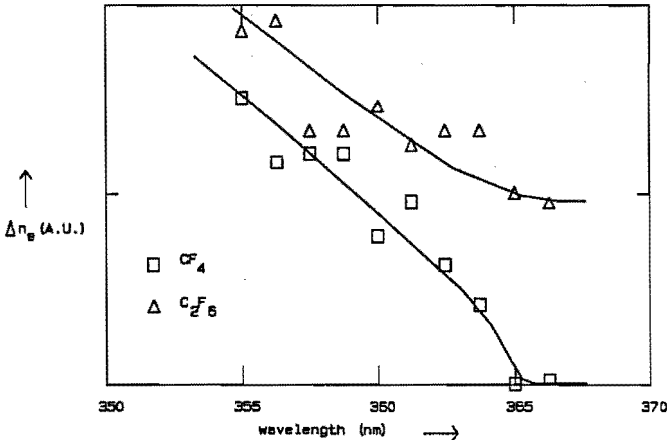

Fig. 5.36   The intensity of the photodetachment signal in plasmas of CF_4 and C_2F_6 as a function of the wavelength in the region where the maximum wavelength for photodetachment of F^- is present. Since the effect is far from saturation, the signal intensity is a measure for the photodetachment cross section in this region. It shows that in CF_4 the F^- ion is the major negative ion, whereas in C_2F_6 other negative ions are also present in significant densities.

photodetachment of F^- ions, in good agreement with mass spectrometry data in a pulsed RF CF_4 plasma[49]. In the case of C_2F_6, above 365 nm still some extra electrons are produced, but the signal is also smaller than for lower wavelengths. The latter suggests that in C_2F_6 plasmas, besides F^- also significant densities of other negative ions (e.g. CF_3^-) are present that can be detached at wavelengths above 365 nm. The CF_3^- ion for instance can be detached[50] at wavelengths up to 465 nm.

The conclusion of these tests is that the detected extra electrons produced by the laser pulse are coming from F^- ions in the laser beam volume.

c) Time dependence of the extra electron density

The density of the extra electrons in the plasma has been measured as a function of time after the laser pulse. This time dependence shows some interesting features. In figure 5.37 an example is shown of the time dependence of the extra electron density in a CF_4 plasma at 100 mTorr and 20 watt RF power. The decay can roughly be divided into two parts. In the first part a relatively fast decay with a time constant of 1.1 μs is observed for about 2 μs. Then the decay slows down. The curve becomes exponential with a time constant of about 18 μs.
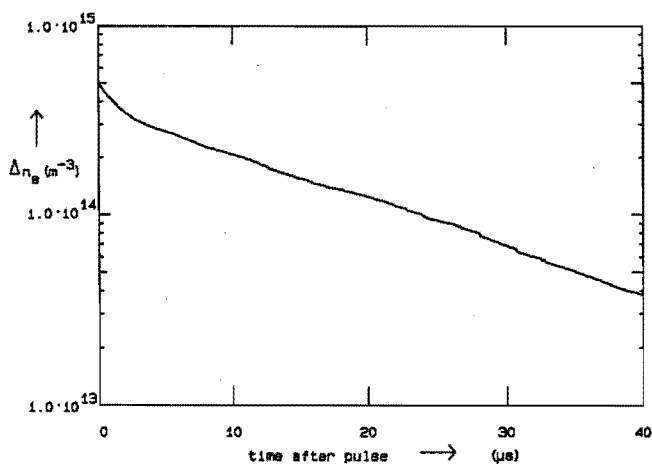

Fig. 5.37   *The density of extra electrons that are produced by the photodetachment*
             process in the plasma. Enhanced loss of electrons is observed in the first
             part of the decay. In the second part the decay can be described by a
             single exponential

The fast decay rate of the first part of the curve in fig. 5.37 may be understood as follows: the extra electrons are produced with an energy ($\approx$ 1 eV) which is lower than the average electron energy and their spatial distribution in the begin is concentrated in the central region of the discharge where the laser beam is fired. This fact and the fact that the same RF power (or even less, since the matching network will be detuned as a result of the changed impedance of the plasma) is now dissipated by more electrons means that the electron temperature T_e in the central region will become slightly lower than before the laser pulse. This will favor attachment with respect to ionization, resulting in a faster decrease electron density. Due to the concentration of the extra electrons in the central region this imbalance will persist until the extra electrons are diffused to the sheath boundary, where they may be heated more efficiently than in the glow region[51]. By using an effective ambipolar diffusion constant based on ref. 52 an estimate can be made of the time required for the extra electron distribution to spread out in the axial direction; the results give a correct magnitude of the duration of the first part of the decay.

An effect which only apparently increases the extra electron decay rate is diffusion in the lateral direction; this brings electrons to the region where the microwave field is weak, resulting in a decrease of the detected frequency shift. An estimated time scale for this effect to occur is however several times longer than the duration of the fast part of the decay. The latter effect is therefore probably mixed up with the second part of the decay.

In the second part of the decay we assume that the extra electrons have the same temperature and the same spatial distribution as the rest of the electrons. However, the total number of electrons is higher than before the laser pulse and will therefore still tend to return to the original value. Since the number of extra electrons is small compared to the total number of electrons already present in the plasma, it is reasonable to assume that the change in T_e will also be small. We can therefore linearize the response of T_e to the electron density perturbation. This can explain the observed exponential decay of the extra electron density to the original equilibrium value. If the decay rate of the second part of the decay is plotted as a function of the squared pressure, we obtain an approximately linear line (increasing decay rate with increasing pressure). However, an attempt to correlate the slope of such a plot with the attachment rate constant, as was done in a preliminary paper[53], is invalidated because the extra electron density decays not by attachment (and axial diffusion) only as was assumed, but by the imbalance between generation (ionization) and loss (attachment and diffusion).

d) Dependence of the negative ion density on macroscopic plasma parameters

Densities of electrons and negative ions were determined as a function of pressure and RF power in plasmas of CF_4, CHF_3, C_2F_6 and C_3F_8. The results of these measurements are depicted in the figures 5.38 − 5.41 together with the ratio of the negative ion density and the electron density. The densities were measured in the center of the cavity.

In CF_4 plasmas the density ratio varies between 4 and 10 depending on the plasma parameters. About the same ratio is found for CHF_3. In C_2F_6 and C_3F_8 even higher values are found, up to 35. Therefore negative ions are the major negatively charged particles in the plasma. The pressure dependencies of n^-/n_e follow the same trend for all gases, i.e. an slow increase with pressure. The dependence of the ratio on the RF power shows some differences between the gases without hydrogen on one hand and CHF_3 on the other hand. For the gases without hydrogen the density ratio increases at lower RF power levels.

To compare the experimental results in CF_4 plasmas with the results of the simulation, we will make an effort to deduce from the experimental densities of electrons
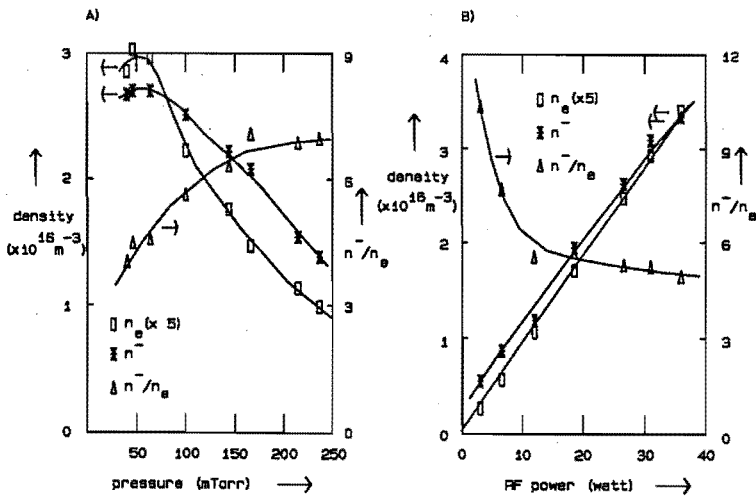

Fig. 5.38   *The electron and negative ion density, and the ratio of the two as a function of A) pressure (at 20 W) and B) RF power (at 120 mTorr) in a CF_4 plasma. It shows that the major negatively charged particles in the plasma are negative ions.*
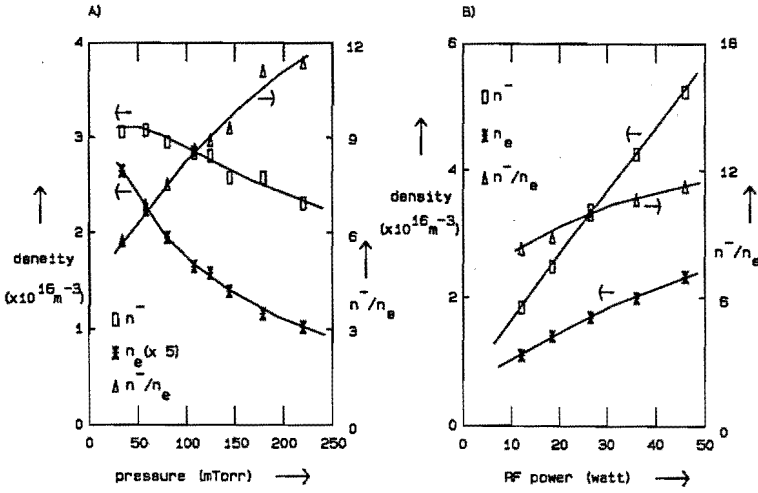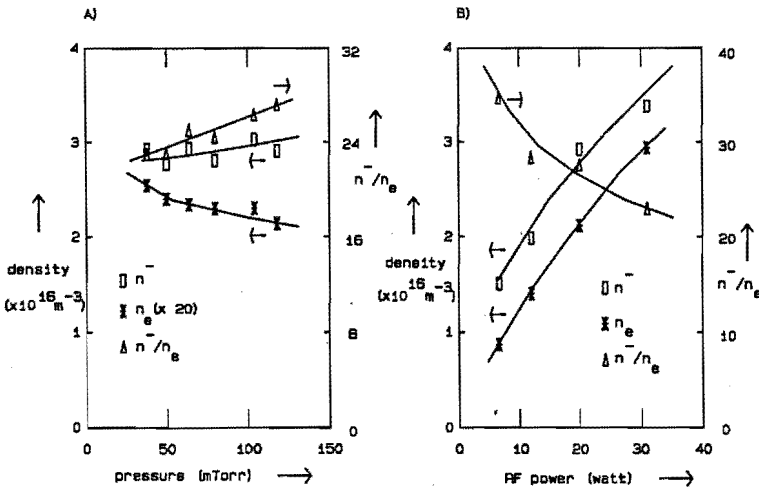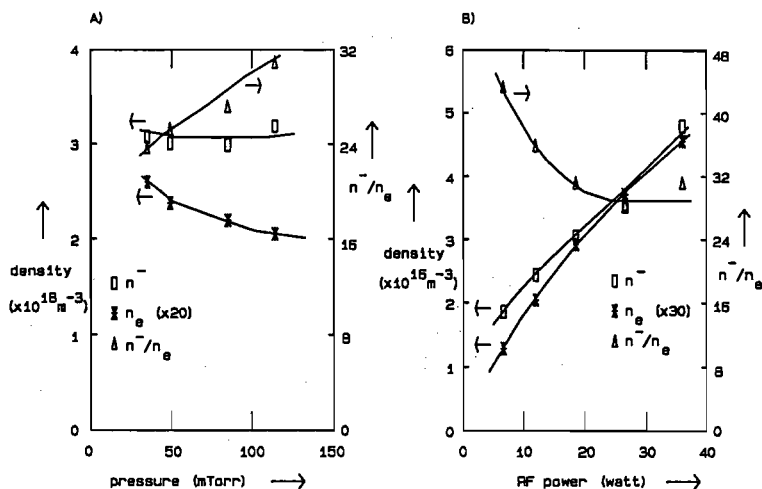
Fig. 5.39 The electron and negative ion density, and the ratio of the two as a function of A) pressure (at 20 watt) and B) RF power (at 120 mTorr) in a CHF_3 plasma. The behavior is similar to that of CF_4, although at higher pressures the ratio is even higher than in CF_4.

Fig. 5.40 The electron and negative ion density, and the ratio of the two as a function of A) pressure (at 20 watt) and B) RF power (at 120 mTorr) in a C_2F_6 plasma. The relative behavior is similar to that of CF_4, but the n^-/n_e ratio can in this case reach values up to 35 at low power levels.

Fig. 5.41   The electron and negative ion density, and the ratio of the two as a
              function of A) pressure (at 20 watt) and B) RF power (at 120 mTorr) in
              a C_3F_8 plasma. The behavior is similar to that of C_2F_6.

and negative ions how the reduced electric field (which can be related to the electron
temperature[54-57]) behaves as a function of pressure. For this it is helpful to solve the
negative ion balance equation. Since the negative ions can not escape from the plasma,
only volume processes need to be considered. For simplicity, the rate coefficients and
electron densities are taken as appropriate averages over the discharge volume. Taking
dissociative attachment, recombination and collisional detachment with neutral radicals
into account we arrive at

$$k_a \cdot [CF_4] \cdot n_e = k_r \cdot n^+ \cdot n^- + k_d \cdot [CF_x] \cdot n^-. \tag{5.12}$$

In this expression n^+ and n^- are the densities of positive and negative ions respectively,
k_r is the rate coefficient for ion–ion recombination, and k_d is the rate coefficient for
collisional detachment with neutrals (in this case mostly CF_2 and CF_3 radicals). Taking
realistic values for k_r ($5 \cdot 10^{-13}$ m³s⁻¹, see section 5.3.3), k_d ($5 \cdot 10^{-16}$ m³s⁻¹, taken from ref.
29), $[CF_x]$ (around 10^{19} m⁻³, see section 5.2), and the concentrations of the negative
ions it follows that the detachment term can have the same order of magnitude as the
recombination term (see also section 5.3.3). Detachment with F radicals[58] is not
considered since at the estimated gas temperature the rate coefficient for collisional

detachment of F⁻ with F is $< 10^{-19}$ m³s⁻¹. Therefore the first two processes mentioned must be taken into account. Using charge quasineutrality it follows that

$$k_a = \frac{N^- \cdot (N^- + n_e) \cdot k_r + N^- \cdot [CF_x] \cdot k_d}{n_e \cdot [CF_4]} .$$ (5.13)

Inserting the measurement data into this expression (where $k_d \cdot [CF_x]$ is taken from the afterglow experiments), we can obtain a set of values for k_a as a function of pressure and of RF power. Since the dependence of k_a on E/N is known[54], we can derive the corresponding values of E/N. The results for the pressure dependence of E/N have been depicted in figure 5.42. Furthermore in figures 5.42 and 5.43 the results of the simulation described in section 3.3.2 are given, i.e. the reduced electric field E/N and the ratio of the negative ion density with respect to the electron density as a function of pressure and RF power. Since the model is in principle only valid for high pressures, the calculation has only been performed at pressures above 200 mTorr and we will only compare the trends. Some interesting conclusions can be drawn from the simulation.

The simulation yields that the ratio n^-/n_e increases as a function of pressure and decreases with RF power, in agreement with the experimental findings for a CF₄ plasma. The simulated values of n^-/n_e agree with the experimental values within a factor of two, the difference being mostly due to the ion densities. The simulated electron density at 200 mTorr agrees with the experimental value within ± 25 %. Furthermore the simulation yields that the reduced electric field E/N tends to decrease as a function of pressure and increases with RF power. This means that the electron temperature T_e must also decrease with pressure and increase with RF power since T_e is a monotonously increasing function[55-57] of E/N. Despite the fact that there is some discrepancy between experiment and theory (probably due to the fact that the assumption of "local equilibrium" in the fluid model is not correct in the pressure range concerned), both the experimental results and the simulation yield that E/N decreases with pressure. The value of E/N in the glow found in the simulation implies that the attachment coefficient k_a is slightly larger than the ionization rate coefficient k_i in the glow. This implies that in most of the volume attachment is faster than ionization and that the ionization must therefore mainly take place at the sheath boundary as has already been indicated by the numerical work of Boeuf[51].

A more quantitative estimate for the electron temperature T_e can be obtained by comparing the value of k_a calculated from the experimental densities with the absolute attachment rate constant as a function of the electron energy $<\epsilon>$, as measured by Hunter et al.[59] in an Ar buffer gas. The corresponding electron energies as a function of
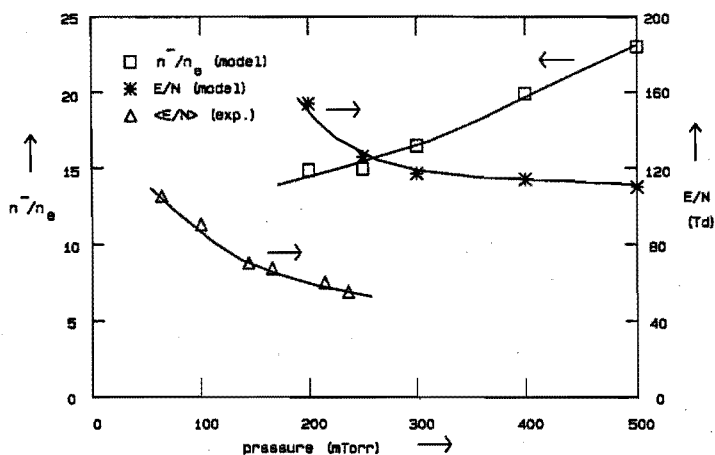
Fig. 5.42   The ratio of the negative ion density and the electron density, and the
              reduced field E/N in the centre of the volume as a function of pressure
              resulting from a fluid model calculation, and the reduced effective field
              as derived from the experimental value of the attachment rate. It indicates
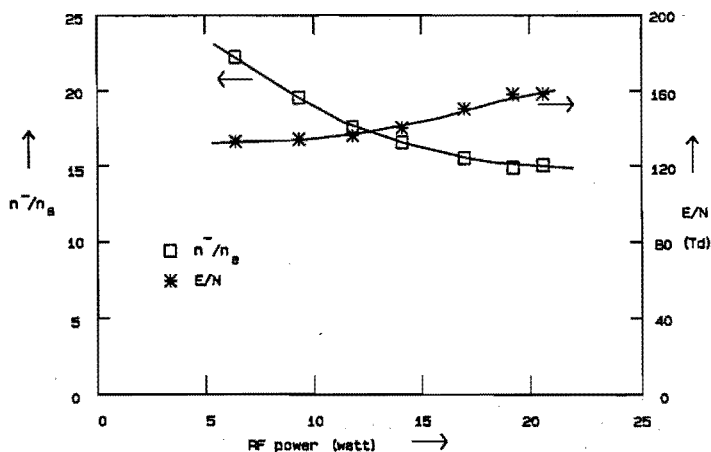   that the electron temperature decreases with pressure.

Fig. 5.43   The ratio of the negative ion density and the electron density and the redu-
              ced field E/N as a function of RF power in the simulation. It indicates that
              the electron temperature slightly increases with increasing RF power.

pressure are then between 3.5 and 4.2 eV and decrease with pressure. Taking $<\epsilon> = kT_e$, this confirms the value of T_e in a CF_4 plasma that was estimated in section 5.2.

The interpretation in the case of CHF_3, C_2F_6 and C_3F_8 may be somewhat different because in these gases CF_x–radical densities may be so high (as a result of the higher C/F ratio and/or the presence of H atoms) that the negative ion loss is mainly due to collisional detachment. As an example of this, it was estimated in section 5.2 that the density of CF_3 in a CHF_3 plasma is roughly 4 times higher than in a CF_4 plasma at the same condition. Therefore we can expect that the rate for collisional detachment of negative ions is also higher. In contrast to this, the results given in figure 5.39 show that in CHF_3 the ion densities are comparable to the ones in CF_4 plasmas. Hence, the recombination rate will also be comparable. As a result, the detachment becomes more important in CHF_3 than in CF_4.

5.3.3 Densities of n_e and n^- in the afterglow

a) Electron densities

In figure 5.44 and 5.45 the decay of the electron and negative ion densities after the termination of the discharge is shown for different conditions. In general, the electron density decay curves show that the relatively rapid decay rate in the early afterglow (t $\leq$ 0.3 ms) slows down in the late afterglow, approaching the negative ion decay rate. Mainly referring to figure 5.44a for convenience, the behavior of the electron density can be understood by looking at the loss and production processes for electrons in the afterglow.

To begin with, electrons are lost by diffusion to the walls. The diffusion loss rate depends on the spatial distribution of the electrons and on the electron diffusion coefficient. Since the higher modes of diffusion decay faster than the first mode of diffusion, after some time only the first mode is left, as can be seen from figure 5.46 where the relative spatial distribution of the negative ions is shown after 0.48 ms. Shortly after the plasma switch–off the electron temperature decreases. On the basis of reported cross sections for vibrational excitation of CF_4 by electron impact[34], the time required for a 4 eV electron to cool down to close–to–thermal values is estimated to be in the order a few μs at the CF_4 pressure of 100 mTorr. Using equation (3.19) we can therefore expect that after a few microseconds the decay due to diffusion slows down due to a decrease in T_e. As β $(= n^-/n_e$) increases, the electron diffusion coefficient and therefore the electron decay rate subsequently increase again. In figure 5.47, where the
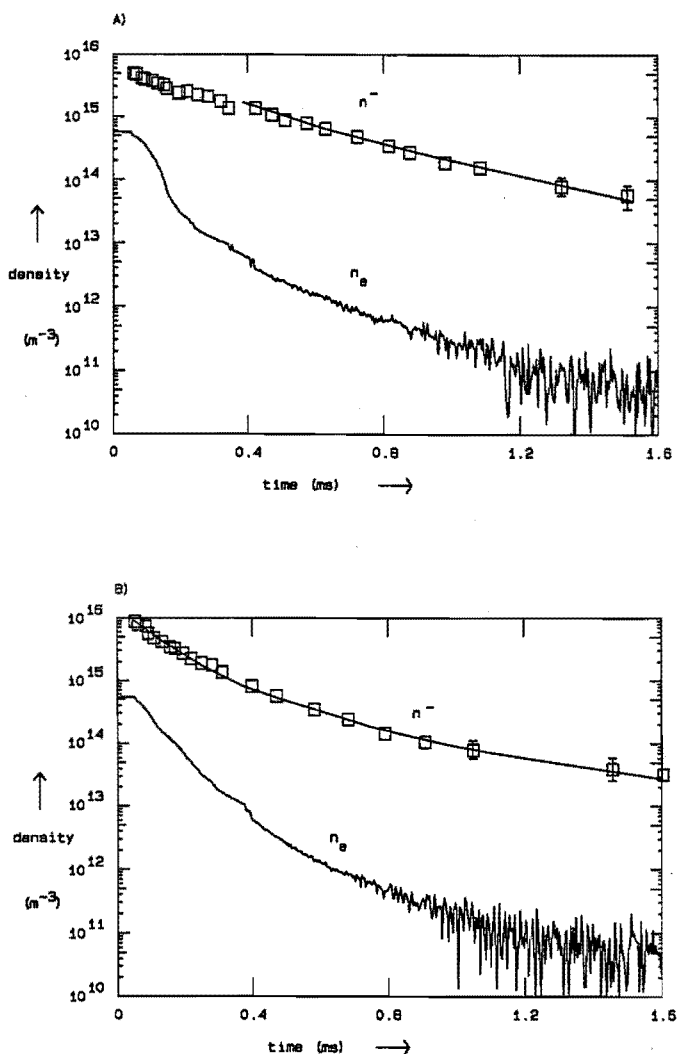
Fig. 5.44   The decay of the electron and negative ion densities in the afterglow of a CF_4 plasma generated at an RF power of 3.5 W and pressures of A) 100 mTorr and B) 300 mTorr. The measurements were made by using the short–circuit. The solid lines connecting the measured negative ion densities are the result of the simulation described in section 3.3.3.
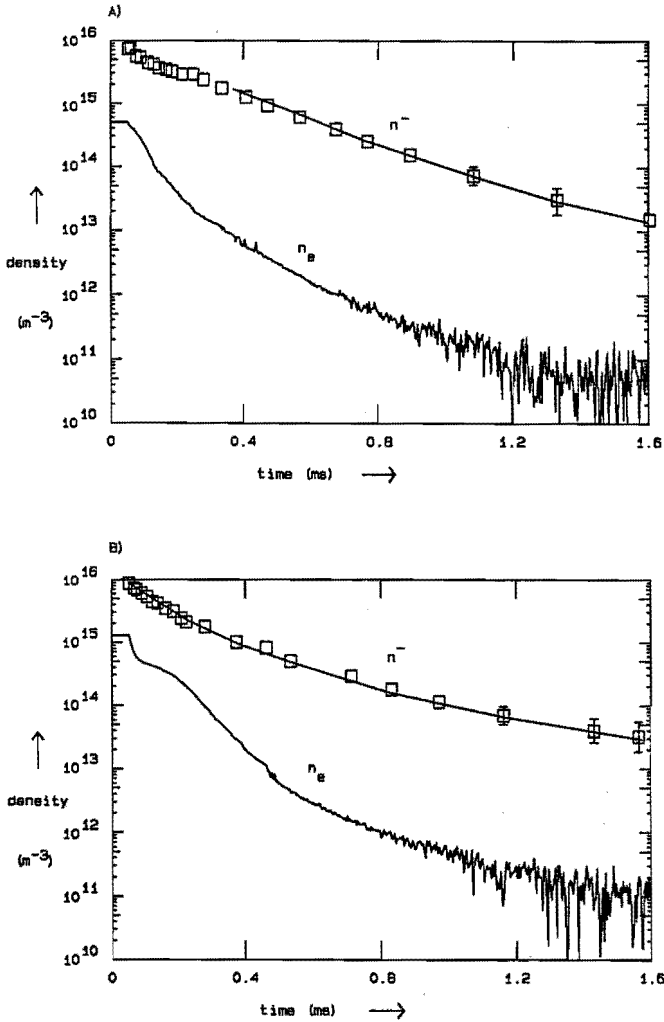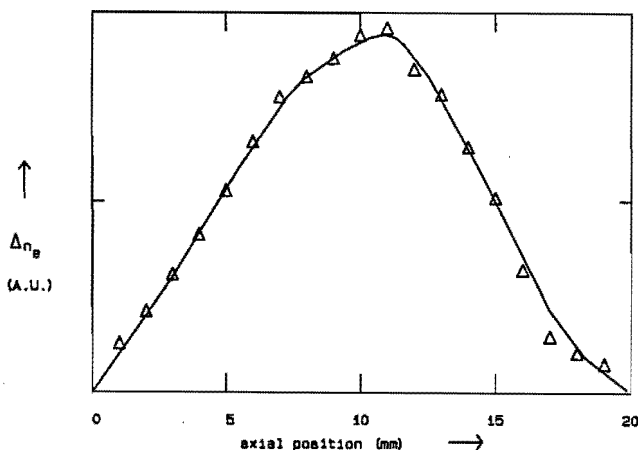
Fig. 5.45   The decay of the electron and negative ion densities in the afterglow of a
CF$_4$ plasma generated at a pressure of 200 mTorr and RF powers of
A) 3.5 W and B) 9 W. The measurements were made by using the
short-circuit. The solid lines connecting the measured negative ion
densities are the result of the simulation described in section 3.3.3.

Fig. 5.46   The measured spatial distribution of negative ions in the afterglow, 480 μs
            after the switch−off of the plasma. The plasma was produced at 200
            mTorr and 5 watt.It can be seen that after sufficient time in the afterglow
            only the first mode of diffusion is left.

decay in the early part of the afterglow is shown, this behavior can be recognized. The
early part of the afterglow can thus be explained as an ambipolar diffusion phenomenon
with the diffusivity enhanced by the presence of negative ions. The loss rate after a few
microseconds in the beginning of the decay can be estimated, using (3.19) and assuming
that $T_e \approx T_i$, from the values of β, D^+, D^-, μ^+ and μ^- to be $\approx 10^4$ s^{-1} for $\beta \approx 10$.

Some volume loss processes of electrons may also contribute significantly to the
decay of the electron density in the early afterglow. Recombination of thermalized
electrons with molecular ions (followed by dissociation) can take place with a rate
constant[60] as large as 10^{-12} m^{3}s^{-1}. With a positive ion density around 10^{16} m^{-3} the rate
becomes also $\approx 10^4$ s^{-1}. Therefore this process may in the initial part of the afterglow
contribute significantly to the decay of electrons. Non−dissociative attachment processes
can be neglected in view of the rate constants for these processes that are known[61].
Dissociative attachment to CF_4, C_2F_6 or CF_x radicals is energetically not possible.
However, dissociative attachment to F_2 has a large rate constant[62] ($\approx 10^{-14}$ m^{3}s^{-1}), and
may well be a significant electron loss process, depending on the F_2 density in the
plasma. To give a comparable contribution as the diffusion, we need a F_2 density of 10^{18}
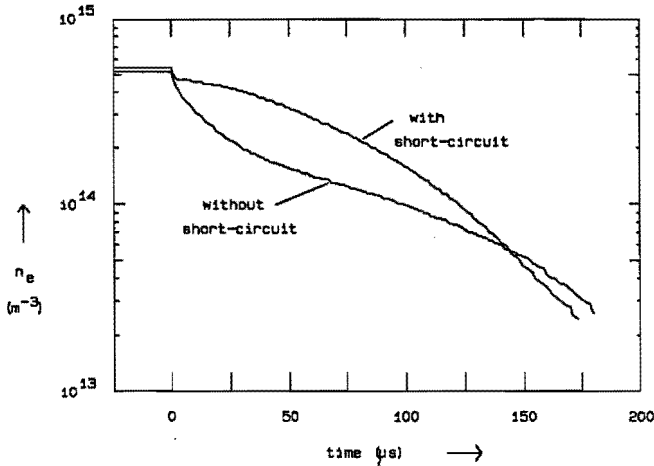m^{-3}. This can therefore be regarded as an upper limit of the F_2 density in the plasma.

Fig. 5.47   The early part of the afterglow in two situations, one in which the
electrodes of the reactor were connected to the short—circuit and one in
which the short—circuit was not employed.

The importance of all these processes with respect to diffusion however becomes less
important with time as β increases.

It is clear from the above discussion that the observed persistence of the electron
density in the late afterglow should be ascribed to some electron generation process,
likely to be collisional detachment of negative ions with neutral radicals. Thus the
apparent slow electron density decay rate in the late afterglow should be due to the slow
negative ion decay rate. The actual electron loss rate in the late afterglow is much
faster. This is demonstrated by the fact that the decay rate of produced photo—electrons
increases at later times in the afterglow, as was observed in the experiment.

In figure 5.47 the effect of the short—circuit can be observed. It shows that the
initial rapid decrease is more prolonged in the case without short—circuit than in the
case where the short—circuit was applied. The time interval in which the decay is fast
more or less corresponds to the duration of the DC bias over the electrodes in the
afterglow without short—circuit. Therefore acceleration of the electrons by the DC
electric field may be responsible for this phenomenon.

b) Negative ion densities in the afterglow

The temporal variation of the negative ion density was measured up to about $t=3$ ms after the termination of the discharge. However, the detected extra electron signals for measurements with $t > 2$ ms were almost constant and showed no spatial dependence when the laser beam was scanned in the axial direction of the cylindrical cavity. This is in contrast with the measurement at $t = 480$ μs (see figure 5.46), in which the negative ion density showed a sine–like distribution between the electrodes. Moreover, a very small signal was also detected without igniting the plasma. Therefore we have judged that the signals in the very late afterglow in part come from photo-electrons that do not originate from negative ions. Possibly a photo–electric effect from scattered laser radiation is responsible for this. In the results shown in figures 5.44 and 5.45, the nominal density obtained from the largest–t measurement has been subtracted from all the data points. This correction is only a few percent in the early afterglow, but becomes large in the late afterglow. The major uncertainty of the late–afterglow data comes from this compensation procedure. The negative ion density in figures 5.44 and 5.45 show a decrease of more than two orders of magnitude in the displayed 1.6 ms time interval. If we assume that the decay rate is caused entirely by ion–ion recombination, we reach the conclusion that the density decrease should be only about one order of magnitude because of the rapidly decreasing recombination loss rate due to the decreasing ion density. From a fluid model simulation[53] of the afterglow similar to that described in section 3.3.2, it is concluded that diffusion can be neglected in the decay of negative ions in the afterglow. Therefore we reach the conclusion that negative ions are significantly lost by collisional detachment, confirming the conclusion in the previous section. Assuming charge quasineutrality, using a numerical solution of (3.15) and systematically changing the parameters k_r, k_d' and τ, solutions were fitted to the experimental results. For the data in figures 5.44b and 5.45b, a good fit was obtained in the entire time span as shown in the figures. In the other cases it was found that the experimental decay rate began to become too slow at around $t \approx 150$ μs if we try to get a good fit for data points in the very beginning of the decay and in the very late afterglow. Therefore the fit was only made for data points later than 300 μs. The best fits were obtained when we set k_r to $(5 \pm 2) \cdot 10^{-13}$ m^{3}s^{-1}. This is an acceptable value for dissociative two–body ion–ion recombination[64]. In table 5.6 the optimized values of k_d' and τ are given, when k_r is fixed at $5 \cdot 10^{-13}$ m^{3}s^{-1}. The results in this table show that in the active CF$_4$ plasma collisional detachment and ion–ion recombination are comparable negative ion loss processes under the low power conditions applied. Since k_d' appears to be relatively insensitive to the RF power, so does the density of the species that is

Table 5.6   *The collisional detachment rate k_d' and its decreasing rate $1/\tau$ deduced from the fit of the solution of equation (3.19) to the experimental results. Estimated errors in k_d' and $1/\tau$ are $\pm$ 20 %.*

Pressure (mTorr)	Power (watt)	k_d' ($10^3 s^{-1}$)	$1/\tau$ ($10^3 s^{-1}$)
100	3.5	4.0	0.42
200	3.5	5.5	0.46
300	3.5	6.6	1.1
200	9	5.8	0.86

responsible for the detachment process. Furthermore the rate for the loss of the detaching species $1/\tau$ increases with increasing RF power. As was discussed in section 5.2 and has been experimentally investigated by Booth et al.[43], the major loss process for CF_2 (and also for CF) radicals is wall loss, which decreases with increasing pressure since the loss becomes diffusion limited. If CF_2 is an important species in the detachment of negative ions we would therefore expect that the rate $1/\tau$ decreases with increasing pressure. The behavior of τ with pressure shown in table 5.6 suggests quite the opposite, i.e. an increase in the rate with increasing pressure. This suggests that the dominant species that performs the collisional detachment is neither CF_2 nor CF, but likely to be CF_3 since CF_3 is also lost by gas phase recombination with fluorine radicals. If we use the value for k_d as given by Edelson et al.[29], i.e. $k_d = 5 \cdot 10^{-16}$ $m^3 s^{-1}$, the density needed to explain the detachment rates in table 5.6 is around 10^{19} m^{-3} which is in the correct order of magnitude as compared to the results obtained in section 5.2 for the density of CF_3.

     For plasmas in other feed gases than CF_4 the importance of collisional detachment as a loss process for negative ions may be higher since it was shown in section 5.2 for CHF_3 plasmas that higher densities of CF_3 are found, whereas in that section it was shown that the ion densities in CF_4 and CHF_3 are comparable.

c) Particle densities in the plasma initiation phase

     To get some information on the production process of the negative ions and to obtain information on the nature of the species that is responsible for the collisional detachment of negative ions some experiments were performed in the initiation phase of

a CF_4 plasma.

In figure 5.48 the variation of the electron density is shown for the initiation phase of a 100 mTorr, 12 W discharge which was modulated with a duty cycle of 15%. After a transient overshoot for a period of a few hundred microseconds, the electron density only shows a slow and small increase toward a steady–state value. The negative ion density that was measured 3 ms after the plasma initiation, was slightly ($\approx 10\%$) larger than the steady–state value. The C_2F_6 molecules are expected to build up in the plasma with a time scale much longer than 3 ms since flow is a major loss process for C_2F_6 (see section 5.2). Thus, if attachment of electrons to C_2F_6 produces a significant amount of negative ions in the discharge, the steady–state negative ion density should be significantly larger than the density measured 3 ms after the initiation of the discharge, contrary to the observed fact. We may therefore conclude that attachment to CF_4 is by far the dominant process that produces negative ions. Similar measurements were carried out for a 300 mTorr, 12 W plasma and led to the same conclusion.

Some information about the building up of the species that are responsible for collisional detachment of the negative ions, can be obtained also by afterglow experiments. Figure 5.49 shows the electron density decay in the early afterglow after a discharge was run for 1, 3, and 50 ms. The total repetition time was in all three situations 100 ms, corresponding to duty cycles of 1, 3, and 50% respectively. Since in this case no short–circuit was employed, the electron density first shows a rapid decay due to the remaining DC bias voltage. Subsequently, the decay rate slows down with the
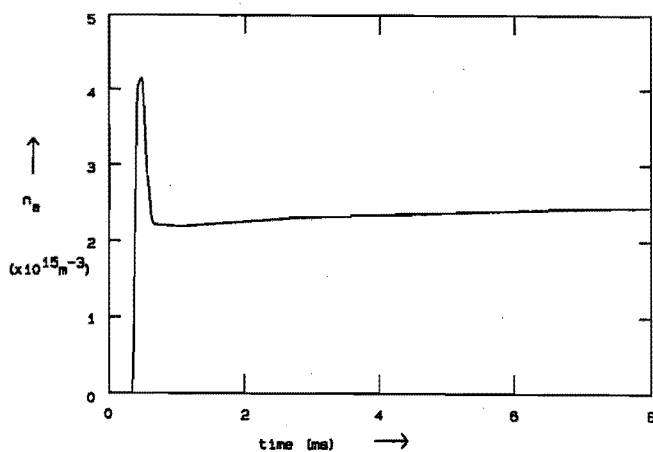

Fig. 5.48   *The variation of the electron density after the initiation of a 100 mTorr, 12 W CF_4 plasma.*

disappearing bias voltage and begins to increase again as β increases, causing a shoulder in the decay curve as can be seen in the figure. Throughout the decay process, electrons are being generated by collisional detachment. Therefore, the more the electrons are generated, the longer it should take for the electron density to decay, that is, the shoulder should become broader as the electron generation rate $k_d'n^-$ increases. Since we expect that n^- in the early afterglow does not depend significantly on the RF pulse width, we may correlate the width of the shoulder with k_d' or the density of the species that are responsible for collisional detachment of the negative ions. In figure 5.49 the width of the shoulder is the largest for curve 2. This means that the density of the detaching species peaks and then decreases toward the steady–state value when the plasma is initiated. In the experiments of Booth et al.[43] the CF and CF_2 densities increased monotonically after plasma initiation. Furthermore in the time–dependence of the neutral particles simulation, only the CF_3 density showed such peaking, due to the relatively slow increase of the fluorine density, as was already found in the simulations of Ryan and Plumb[44]. Therefore the results suggest that CF_3 is mainly responsible for the collisional detachment process.
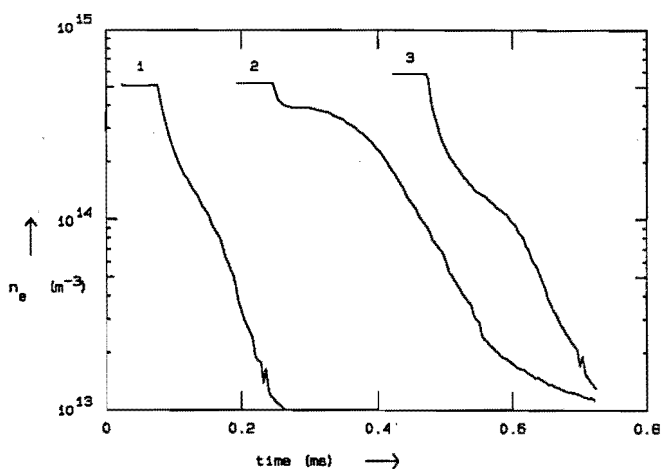

Fig. 5.49   The decay of the electron density in the early afterglow of a CF_4 plasma after the discharge was run for 1 ms (curve 1), 3 ms (curve 2) and 50 ms (curve 3). The pressure was 200 mTorr and the RF power was 3.5 watt. No short–circuit was employed.

5.3.4 Conclusions

It has been shown that the microwave cavity method is a well suited method to *in situ* determine electron densities in RF plasmas. The electron densities in fluorocarbon RF plasmas show a tendency to decrease with the complexity of the feed gas molecule. This may be due to the increase in the attachment coefficient with increasing complexity, but may also be due to increasing dissipation of part of the RF power by vibrational excitation processes.

The same method can in combination with the photodetachment effect be effectively used for the determination of negative ion densities in RF plasmas of halogenated gases. Results have been obtained for plasmas of CF_4, CHF_3, C_2F_6 and C_3F_8. In CF_4 the negative ions consist almost only of F^- whereas in C_2F_6 significant densities of other negative ions may be present. Densities of negative ions have been determined as a function of gas pressure and RF power. The results indicate that, depending on the gas and on the plasma parameters, negative ion densities are a factor 4 to 35 higher than the electron density in the plasma. The behavior of the ratio of the densities of electrons and negative ions indicates that the electron temperature in CF_4 plasmas increases with the RF power and decreases with pressure and has values in the range of 3.5–4.2 eV. This therefore confirms the findings in section 5.2 that T_e is around 4 eV.

The time–dependence of the electron and negative ion densities in the afterglow and initiation phase of a CF_4 plasma indicates that loss of negative ions by collisional detachment with neutral radicals is equally or more important than ion–ion recombination. From an analysis of the time–dependence the ion–ion recombination rate constant was estimated to be $(5 \pm 2) \cdot 10^{-13}$ $m^3 s^{-1}$. It was furthermore established that the density of the neutral species that is responsible for the detachment reaction peaks in the initiation phase of the plasma and then decreases towards the steady–state density. This suggests that CF_3 is mainly responsible for the detachment reaction. From the behavior of the electron and negative ion densities in the plasma initiation phase it is concluded that attachment to CF_4 is the main production process for negative ions in a CF_4 plasma.

References

[1]   R. d'Agostino, P. Capezutto, G. Bruno, F. Cramarossa,
         Pure and Appl. Chem. 57(9), 1287, (1985).
[2]   D.L. Flamm, V.M. Donnelly, J.A. Mucha, *J. Appl. Phys.* 52(5), 3633 (1981).

3   W.J. Moore, *Physical Chemistry*, (Prentice–Hall, London, 1972).

4   J.W. Coburn, H.F. Winters, *J. Appl. Phys.* 51, 2614 (1980).

5   D.L. Flamm, V.M. Donnelly, *Plasma Chem. Plasma Proc.* 1(4), 317 (1981).

6   G.S. Oehrlein, H.L. Williams, *J. Appl. Phys.* 62(2), 662 (1987).

7   J.L. Buckner, D.J. Vitkavage, E.A. Irene, T.M. Mayer,
     J. Electrochem. Soc. 133(8), 1729 (1986).

8   G.S. Oehrlein, I. Reimanis, Y.H. Lee, *Thin Solid Films* 143, 269 (1986).

9   G.M.W. Kroesen, *Plasma deposition, investigations on a new approach*,
     Ph.D. thesis (Eindhoven 1988).

10   G.M.W. Kroesen, G.S. Oehrlein, E. de Fresart, M. Haverlag,
     to be published.

11   Ch. Cardinaud, G. Turban, S. Quillard, *Proc. ISPC IX*,
     Pugnochiuso, Italy 1989, pp 1583.

12   M. Levy, E. Scheid, S. Cristoloveanu, *Thin Solid Films* 148, 127 (1987).

13   J.L. Vossen, *J. Appl. Phys.* 47, 544 (1976).

14   G.S. Oehrlein, *J. Appl. Phys.* 59(9), 3053 (1986).

15   J.W. Coburn, H.F. Winters, *J. Vac. Sc. Techn.* 16, 391 (1979).

16   T.H. Fedynyshyn, G.W. Grynkewich, T.B. Hook, M.D. Liu,
     J. Electrochem. Soc. 134, 206, (1986).

17   R.M. Robertson, M.J. Rossi, D.M. Golden,
     J. Vac. Sci. Techn. A5(6), 3351 (1987).

18   M.A. Jaso, G.S. Oehrlein, *J. Vac. Sci. Techn.* A6, 1397 (1988).

19   T.H.J. Bisschops, *Investigations on an RF plasma related to plasma etching*,
     Ph.D. thesis (Eindhoven 1987).

20   G. Fortuno, *Plasma Chem. Plasma Proc.* 8(1), 19 (1988).

21   J.H. Thomas, X.C. Mu, S.J. Fonash, *J. Electrochem. Soc.* 134(12), 3122 (1987).

22   R.J. Archer, G.W. Gobeli, *J. Chem. Solids* 26, 343 (1965).

23   G.S. Oehrlein, G.J. Scilla, S.J.Jeng, *Appl. Phys. Lett.* 52(11), 907 (1988).

24   M. Capitelli, M. Dilonardo, R. Winkler, J. Wilhelm,
     Contrib. Plasma Phys. 26(6), 443 (1986).

25   P.M. Vallinga, *Modelling of RF plasmas in a parallel plate etch reactor*,
     Ph.D. thesis (Eindhoven 1988).

26   Y. Kaufman, Y.M. Kagan, *J. Appl Phys.* D14, 2215 (1981).

27   L.G. Christophorou, *J. Chem. Phys.* 83(12), 6219 (1985).

28   M. Allen and S.F. Wong, *J. Chem. Phys.* 74, 1687 (1981).

29   D. Edelson, D.L. Flamm, *J. Appl. Phys.* 56(5), 1522 (1984).

30   E.M. van Veldhuizen, T.H.J. Bisschops, E.J.W van Vliembergen,
      H.M.C van Wolput, *J. Vac. Sci. Techn.* A3(6), 2205 (1985).

31   L.H. Jones, C. Kennedy, S. Ekberg, *J. Chem. Phys.* 69(2), 833 (1978).

32   G. Herzberg, *Infrared and Raman spectra of Polyatomic Molecules*,
      12th ed. (Lancaster Press, Lancaster, USA, 1966), pp 40, 267, 454.

33   R.M. van Iersel, Internal report VDF–NT/90–22, (Eindhoven 1990).

34   M. Hayashi, in *Swarm studies and Inelastic Electron–Molecule Collisions*,
      edited by L.C. Pitchford, B.V. McKoy, A. Chutjian and S. Trajmar
      (Springer–Verlag, New York, 1987), pp. 167.

35   W.H. Kasner, M.A. Biondi, *Phys. Rev.* 137, 317 (1965).

36   R. Walkup, Ph. Avouris, R.W. Dreyfus, J.M. Jasinski,
      Appl. Phys. Lett. 45(4),372 (1984).

37   C.A.M. de Vries, A.J. van Roosmalen, G.C.C. Puylaert,
      J. Appl. Phys. 57(9), 4386 (1985).

38   V.D. Rusanov, A.A. Fridman, G.V. Sholin, *Sov. Phys. Uspekhi* 24(6), 447
      (1981).

39   W.B. Person, J.H. Newton, *J. Mol. Struct.* 46, 105, (1978).

40   E.M. van Veldhuizen, T.H.J. Bisschops, E.J.W. van Vliembergen,
      H.M.C. van Wolput, *J. Vac. Sci. Techn.* A3(6), 2205 (1985).

41   J.B. Burkholder, C.J. Howard, *J. Molec. Spectr.* 127, 362 (1988).

42   P.B. Davies, P.A. Hamilton, J.M. Elliot, M.J. Rice,
      J. Molec. Spectr. 102, 193 (1983).

43   J.P. Booth, G. Hancock, N.D. Perry, M.J. Toogood,
      J. Appl. Phys. 66(11), 5251 (1989).

44   K.R. Ryan, I.C. Plumb, *Plasma Chem. Plasma Proc.* 6, 231 (1986).

45   N. Selamoglu, M.J. Rossi, D.M. Golden, *Chem. Phys. Lett.* 124, 68 (1986).

46   S.R. Hunter, L.G. Christophorou, *J. Chem. Phys.* 80(12), 6150 (1984).

47   J.D. Molnar, *Phys. Rev.* 83(5), 940 (1951).

48   S. Vacquie, A. Gleizes, M. Sabsabi, *Phys. Rev.* A35, 1615 (1987).

49   L.J. Overzet, J.H. Beberman, J.T. Verdeyen, *J. Appl. Phys.* 66, 1622 (1989).

50   J.H. Richardson, L.M. Stephenson, J.I. Brannon, *Chem. Phys. Lett.* 30, 17
      (1975).

51   J.P. Boeuf, *Phys. Rev.* A36(6), 2782 (1987).

52   E.J.R. Hollahan, A.T. Bell, *Techniques and Applications of Plasma Chemistry*,
      (John Wiley, New York, 1974).

53   J.L. Jauberteau, G.J. Meeusen, M. Haverlag, G.M.W. Kroesen, F.J. de Hoog,
      J. Phys. D24, 261 (1991).

[54]   S.R. Hunter, J.G. Carter, L.G. Christophorou, *Phys. Rev.* A38(1), 58 (1988).

[55]   K. Masek, L. Laska, R. d'Agostino, F. Cramarossa,
Contrib. Plasma. Phys. 27, 15 (1987).

[56]   M.S. Naidu, A.N. Prasad, *J. Phys.* D5, 983 (1972).

[57]   C.S. Lakshminarasimha, J. Lucas, J. Price, *Proc. IEEE* 120, 1044 (1973).

[58]   A. Mandl, *J. Chem Phys.* 59(6), 3423 (1973).
ed. by L.C. Pitchford, B.V. McKoy, A. Chutjian and S. Trajmar
(Springer—Verlag, New York 1987), p. 167.

[59]   S.R. Hunter, L.G. Christophorou, *J. Chem. Phys.* 80(12), 6150 (1984).

[60]   H.M.W. Massey, H.B. Gilbody, *Electronic Ionic Impact Phenomena*
(Oxford Univ. Press, Oxford, 1974).

[61]   B.M. Smirnov, *Negative ions* (McGraw—Hill, New York, 1982), chapters 4,6.

[62]   D.L. McCorkle, L.G. Christophorou, A.A. Cristodoulides, L. Pichiarella,
J. Chem. Phys. 85, 1966 (1986).

[63]   A. Kono, M. Haverlag, G.M.W. Kroesen, F.J. de Hoog,
submitted for publication to J. Appl. Phys.

[64]   R.E. Olson, *J. Chem. Phys.* 56, 2979 (1972).

6 CONCLUSIONS

a) Surface phenomena

—   *In situ* ellipsometry can provide for an excellent monitor of the etching process. Not only an accurate determination of the etch rate is possible but also information can be obtained on the optical properties and morphology of the layer being etched or deposited.

—   The observed trends in the etch rate as a function of the macroscopic plasma parameters suggest that in the case of Si etching in fluorocarbon RF plasmas both ion–enhanced processes and the formation of an inhibitor layer play a role. The etching of SiO_2 is likely to be ion–enhanced.

—   The electrode material has an influence on the selectivity of Si over SiO_2, since the Si etch rate is reduced in the presence of a $[CF_x]_n$ coated electrode whereas the etch rate of SiO_2 is hardly affected.

—   It was established that during Si etching in CF_4 only a thin fluorocarbon layer is present on the surface, which hardly inhibits the etching reaction, whereas during etching in CHF_3 this layer is thicker. The influence of the inhibitor layer is therefore larger in CHF_3 than CF_4 plasmas.

—   Damaging of the topmost layer of the surface due to the ion bombardment during the etching process increases with the RF power and decreases with the pressure in agreement with the trends of the ion fluxes and ion energies that are known.

b) Neutral particles in the plasma

—   Infrared absorption spectroscopy is well suited to investigate the vibrational excitation of CF_4 in a CF_4 plasma due to the existence of hot band transitions.

—   The excitation of the ν_2 mode of CF_4 changes only slightly when a plasma is created. At a gas pressure of 100 mTorr, a gas flow of 20 sccm and an RF power of 100 watt, the vibrational temperature of this mode was found to be only 400 K. If the same applies to other modes, this implies that in RF CF_4 plasmas vibrational excitation may not be an important factor for the production process

of negative ions by dissociative attachment in contradiction to what has been shown for other gases in the literature.

— The rotational temperature in a CF_4 plasma, which is close to the gas temperature, at 100 mTorr, 20 sccm and 100 watt was found to be 350 ± 20 K.

— Infrared absorption spectroscopy can also be applied successfully to measure the absolute densities of stable as well as unstable neutral species in the plasma.

— Densities of CF_2 radicals and C_2F_6 molecules in plasmas made in CF_4 were measured. At a pressure of 100 mTorr, a gas flow of 50 sccm and a total RF power of 80 watt the CF_2 density was found to be $(10 \pm 4) \cdot 10^{18}$ m^{-3}. The C_2F_6 density at this condition was found to be $(2.5 \pm 0.5) \cdot 10^{18}$ m^{-3}. A numerical simulation of the neutral particle kinetics indicates that the CF_3 density in the plasma at this condition is about $5 \cdot 10^{18}$ m^{-3}.

— From a comparison between the simulated and experimentally determined densities, it has been concluded that the rate coefficients for dissociation of CF_4 by electrons that are reported in the literature are slightly too small to explain the observed densities of CF_2 and C_2F_6 in a CF_4 plasma. The observed values imply that the electron temperature T_e has a value around 4 eV.

— From a comparison of the densities of C_2F_6 in CF_4- and CHF_3-plasmas it was found that the CF_3 density is about 4 times higher in a CHF_3 plasma as compared to a CF_4 plasma. This is in agreement with the observed surface phenomena.

c) Charged particles in the plasma

— It has been demonstrated that the microwave cavity resonance method is well suited to *in situ* determine electron densities in RF plasmas. Moreover, the same method can, in combination with the photodetachment effect, be effectively used for the determination of absolute densities of negative ions in RF plasmas of halogenated gases.

— Negative ion densities in fluorocarbon RF plasmas are a factor 4 to 35 higher than the electron density in the plasma. The ratio n^-/n_e increases with the

attachment coefficient of the feed gas.

— The electron densities in fluorocarbon RF plasmas show a tendency to decrease with the complexity of the feed gas molecule at the same power input. This may be due to the increase in the attachment coefficient with increasing complexity, but may also be due to increasing dissipation of part of the RF power by vibrational excitation processes.

— In CF_4 plasmas the negative ions consist almost only of F^- whereas in C_2F_6 significant densities of other negative ions may be present.

— The behavior of the ratio of the densities of electrons and negative ions indicates that the electron temperature increases with the RF power and decreases with pressure and has values that are in the range of 3.5–4.2 eV. This is in agreement with the conclusions from the infrared absorption experiments.

— The time dependence of the electron and negative ion densities in the afterglow and initiation phase of a CF_4 plasma indicates that loss of negative ions by collisional detachment with neutral radicals plays an important role, as does ion–ion recombination.

— From an analysis of the time–dependence of the electron and negative ion densities in the afterglow of an RF CF_4 plasma the ion–ion recombination rate constant was estimated to be $(5 \pm 2) \cdot 10^{-13}$ m^{3}s^{-1}.

— It was established that the density of the neutral species that is responsible for detachment of negative ions peaks in the initiation phase of a CF_4 plasma and then decreases towards the steady–state density. This behavior suggests that CF_3 is the dominating species that is involved in the detachment reaction with negative ions.

— The behavior of the electron and negative ion densities in the plasma initiation phase indicates that attachment to CF_4 is the main production process for negative ions in a CF_4 plasma.

SUMMARY

In this thesis investigations on capacitively coupled radio frequency (RF) plasmas in fluorocarbon gases excited at 13.56 MHz are described. These plasmas are commonly used for many applications where a substrate must be etched, e.g. in the manufacturing of integrated circuits. For this purpose the substrate to be etched is placed on one of two parallel plate electrodes, to which an RF voltage is applied. The resulting oscillating electric field generates a plasma between the electrodes in which reactive particles such as radicals and ions are produced. Positively charged ions that are created in the plasma are accelerated towards the electrodes, due to the difference in mobility between electrons and ions. As a result of this, etching in RF plasmas has some advantages over etching in chemically active liquids, like the capability to yield anisotropic etching profiles.

Since the characteristics of the etching process are strongly dependent on the densities and energies of the particles in the plasma, knowledge of these quantities is important for a fundamental understanding of the processes taking place in the plasma. Several *in situ* diagnostics have therefore been developed to study the etching performance of the setup and to measure the densities and energies of the various neutral and charged particles present.

The etch rate of the etching station was studied using *in situ* ellipsometry. For this purpose a high–speed rotating–analyzer ellipsometer was constructed for single-wavelength operation. With this ellipsometer the etch rate was determined as a function of the macroscopic plasma parameters. It was found that the etch rate for both Si and SiO_2 decreases at high pressure. For Si etching this is due to the formation of an inhibiting fluorocarbon layer on top of the surface and due to a decrease in the flux of positive ions that enhance the etching reaction. For SiO_2 etching only ion–enhancement occurs. Furthermore, it was found that the etch rate depends on the electrode material. This effect is stronger in Si etching than in SiO_2 etching, indicating that the neutral particle chemistry plays a more dominant role in the case of Si.

Time–dependent ellipsometric measurements at the start of the etching process of Si were used to analyze the damaging and contamination of the top layer of the surface due to the plasma exposure. It was found that the damaging follows the trends of the ion flux and energies. Furthermore the thickness of the fluorocarbon layer in a CHF_3 was found to be large enough to inhibit the etching of Si. In CF_4 plasmas this inhibitor layer is too thin to influence the etch rate significantly.

Densities of neutrals in the plasma have been studied by infrared absorption spectroscopy. For this purpose a Fourier Transform spectrometer has been constructed

that is capable of measuring infrared spectra between 5 and 10 μm with a resolution of 0.015 cm^{-1}. With this apparatus an investigation of the vibrational excitation of the CF_4 molecule in a CF_4 discharge has been carried out. It was found that the ν_2 mode of CF_4 has a vibrational temperature of about 400 K. Therefore the upper levels of the transition are not significantly populated. It can however not been excluded that other vibrational modes may be significantly excited. From the same measurement it was also established that the gas temperature is just above room temperature (350 K).

Furthermore Infrared absorption spectroscopy was utilized to measure the densities of CF_2 radicals and C_2F_6 molecules in a CF_4 plasma. Using a numerical simulation of the neutral particle kinetics, the density of CF_3 radicals was deduced from the measured densities of C_2F_6 as a function of flow and pressure. All densities were found to be a few times 10^{18} m^{-3} for the conditions investigated. From a comparison between the measured and simulated densities it was derived from the observed radical production rates that the electron temperature in the plasma is about 4 eV, which is close to the values estimated in the literature.

Densities of electrons in the discharge were obtained using a microwave resonance technique. It was established that the electron density tends to decrease as the attachment coefficient of the feed gas increases, in agreement with a numerical simulation based on a fluid model. The same microwave method was employed, in combination with saturated laser induced photodetachment of negative ions, to *in situ* determine the absolute densities of negative ions in the plasma. It was found that the negative ion density n^- roughly follows the trends of the electron density n_e, but is between 4 to 35 times larger than the electron density. The ratio n^-/n_e increases slowly with pressure and increases at low power levels. From an analysis of the negative ion balance in the plasma it was derived that the electron temperature is between 3.5 and 4.2 eV, depending on the plasma parameters.

Densities of electrons and negative ions were also measured in the afterglow, to obtain a value for the ion—ion recombination coefficient, i.e. $(5 \pm 2) \cdot 10^{-13}$m^{3}s^{-1}. The evolution with time in the afterglow revealed that in the active plasma the loss of negative ions by collisional detachment is comparable to the loss by ion—ion recombination. Production of negative ions in a CF_4 plasma is governed by dissociative attachment of electrons to CF_4. Most of the negative ions in CF_4 consist of F^-, whereas in C_2F_6 plasmas besides F^- significant densities of other negative ions were detected.

SAMENVATTING

In dit proefschrift wordt een beschrijving gegeven van enkele studies aan capacitief gekoppelde radiofrequente (RF) plasma's in fluor– en koolstofhoudende gassen die worden geëxciteerd met een frequentie van 13.56 MHz. Dergelijke plasma's worden veel gebruikt in toepassingen waar een laag moet worden geëtst, zoals bij de fabricage van geïntegreerde schakelingen. Voor dit doel wordt het te etsen substraat op één van twee parallel gepositioneerde electrodes geplaatst, waaraan een RF spanning wordt toegevoerd. Het resulterende electrische wisselveld genereert een plasma tussen de electrodes waarin reactieve deeltjes zoals radicalen en ionen worden geproduceerd. Positief geladen ionen die in het plasma worden gecreëerd worden versneld naar de electrodes als gevolg van het verschil in beweeglijkheid tussen electronen en ionen. Om deze reden heeft het etsen in RF plasma's enige voordelen t.o.v. het etsen met chemisch actieve vloeistoffen, zoals bijvoorbeeld de mogelijkheid tot het genereren van anisotrope etsprofielen.

Omdat de eigenschappen van het etsproces sterk afhankelijk zijn van de dichtheid en de energie van de verschillende deeltjes in het plasma is kennis van de waarden van deze grootheden belangrijk voor een fundamenteel begrip van de processen die plaatsvinden in het plasma. Een aantal *in situ* diagnostieken zijn daarom ontwikkeld voor het meten van de dichtheid en energie van de verschillende neutrale en geladen deeltjes die aanwezig zijn.

De etssnelheid van de opstelling is bestudeerd m.b.v. *in situ* ellipsometrie. Voor dit doel is een snelle roterende–analysator ellipsometer gebouwd voor metingen op één enkele golflengte. Met deze ellipsometer zijn metingen verricht van de etssnelheid als functie van de macroscopische plasma parameters. Er werd gevonden dat de etssnelheid van zowel Si als SiO_2 afneemt bij hoge drukken. In het geval van Si etsen komt dit zowel door de vorming van een blokkerende bovenlaag bestaande uit koolstof en fluor, als door een verminderde ionenflux die gewoonlijks de etsreacties stimuleert op het oppervlak. In het geval van het etsen van SiO_2 is alleen de stimulering door ionen van belang. Verder werd gevonden dat de etssnelheid afhangt van het materiaal van de electrodes. Dit effect is sterker in Si dan in SiO_2, wat aangeeft dat de chemie van de neutrale deeltjes bij Si een belangrijkere rol speelt.

Tijdsafhankelijke ellipsometrische metingen aan het begin van het etsproces van een Si plak zijn gebruikt om de beschadiging en verontreiniging van de bovenste laag van het oppervlak door het plasma te bestuderen. Er werd gevonden dat de beschadiging globaal de trends van de ionenflux en ionenenergieverdeling volgt. Verder werd gevonden dat de dikte van de fluorkoolstoflaag in een CHF_3 plasma dik genoeg is om de etsreactie

te hinderen. In CF_4 plasma's wordt de etssnelheid niet veel door deze laag beïnvloed.

Dichtheden van neutrale deeltjes in het plasma zijn gemeten met infrarood absorptie spectroscopie. Voor dit doel is een Fourierspectrometer geconstrueerd, die in staat is om infraroodspectra tussen 5 en 10 μm te bepalen met een resolutie van 0.015 cm^{-1}. Met dit apparaat zijn metingen verricht aan de vibrationele excitatie van het CF_4 molecuul in een CF_4 ontlading. Er werd gevonden dat de ν_2 mode van CF_4 een vibratietemperatuur van ongeveer 400 K heeft en dus niet sterk geëxciteerd is. Het kan echter niet worden uitgesloten dat andere modes in een hogere mate zijn aangeslagen. Uit dezelfde meting is afgeleid dat de temperatuur van het gas iets boven kamertemperatuur ligt, met een waarde van ongeveer 350 K. Infrarood absorptie-spectroscopie is verder gebruikt om de dichtheid van CF_2 radicalen en C_2F_6 in een CF_4 plasma te bepalen. Met behulp van een numerieke simulatie van de kinetiek van de neutrale deeltjes kon de dichtheid van CF_3 radicalen worden afgeschat. Alle dichtheden bleken een paar keer 10^{18} m^{-3} te zijn onder de condities die bestudeerd zijn. Uit een vergelijk tussen gemeten en berekende dichtheden is afgeleid dat de waarde van de electronentemperatuur dicht bij de waarde ligt die tot dusver wordt aangenomen in de literatuur, namelijk ongeveer 4 eV.

Dichtheden van electronen in de ontlading zijn verkregen door gebruik te maken van een microgolf resonantie techniek. Er werd gevonden dat de electronendichtheid afneemt met de attachment coefficiënt van het gas, in overeenstemming met een vloeistofmodel van het plasma. Dezelfde microgolfmethode is gebruikt, in combinatie met een door laserstraling geïnduceerde opbreking van negatieve ionen in neutralen en electronen, om *in situ* absolute dichtheden te bepalen van negatieve ionen in het plasma. Het blijkt dat de negatieve ionen dichtheid n^- ruwweg de trends volgt van de electronendichtheid n_e, maar dat de negatieve ionen dichtheid 4 tot 35 keer zo groot is als n_e. De verhouding n^-/n_e stijgt langzaam met de druk en wordt groter bij lage plasmavermogens. Uit een analyse van de n^- balans is afgeleid dat, afhankelijk van de plasma parameters, de electronentemperatuur tussen 3.5 en 4.2 eV varieert.

Dichtheden van electronen en negatieve ionen zijn verder gemeten in de nagloei-fase. Hieruit is een waarde voor de ion–ion recombinatiecoefficiënt afgeleid, $(5 \pm 2) \cdot 10^{-13}$ $m^3 s^{-1}$. Het verloop in de nagloeifase geeft aan dat in het actieve plasma het verlies van negatieve ionen door botsingsdetachment vergelijkbaar is met het verlies door ion–ion recombinatie. Productie van negatieve ionen gebeurt voor het grootste deel door dissociatieve attachment van electronen aan CF_4. Het merendeel van de negatieve ionen in een CF_4 plasma bestaat uit F^-, terwijl in C_2F_6 plasma's naast F^- ook nog significante hoeveelheden van andere negatieve ionen werden gedetecteerd.

DANKWOORD

Curriculum Vitae

23 februari 1964 geboren te Utrecht

mei 1982	Diploma VWO, College Blaucapel, Utrecht
maart 1987	Doctoraal examen Technische Natuurkunde, afdeling
	Technische Natuurkunde, Technische Universiteit Twente
april 1987	In dienst van de Technische Universiteit Eindhoven
—augustus 1991	als Assistent—In—Opleiding.
oktober 1991—	In dienst van IBM Research als postdoc aan het
	T.J. Watson Research Center in Yorktown Heights (NY).

STELLINGEN

behorende bij het proefschrift

PLASMA CHEMISTRY OF FLUOROCARBON RF
DISCHARGES USED FOR DRY ETCHING

M. Haverlag

10 september 1991

De combinatie van microgolfresonantie met door een laserpuls opgewekte foto–onthechting maakt het mogelijk om dichtheden van negatieve ionen in plasma's absoluut en met grote gevoeligheid te meten zonder het plasma te verstoren.
(Dit proefschrift, sectie 5.3)

2

Behalve voor diagnostische toepassingen leent *in situ* ellipsometrie zich ook voor eindpuntdetectie. Hiervan kan gebruik gemaakt worden om door middel van reactief ionenetsen (RIE) hoge etssnelheden te combineren met een lage beschadiging.
(Dit proefschrift, sectie 5.1)

3

Bij het meten van de modificatie van het oppervlak van een geëtst siliciumsubstraat met een *ex situ* monochromatische ellipsometrische meting waarvan alleen de ellipso–metrische hoek Δ wordt gebruikt is het verleidelijk om meer informatie uit de meting te halen dan daarin werkelijk aanwezig is.
(Ch. Cardinaud, G. Turban, S. Quillard, *Proc. IX ISPC*, Bari 1989, pp 1583)

4

Het vermelden van het ingekoppelde radiofrequente vermogen bij gebruik van een plasmareactor met planparallelle electrodes heeft weinig betekenis als de geometrie, in het bijzonder de oppervlakte van de electrodes, niet is vermeld.
(L.M. Buchmann, F. Heinrich, P. Hoffmann, J.Janes, *J. Appl. Phys.* **67**(8), 3635 (1990)

5

Het gebruik van een ellipsometer met een roterende compensator vereenvoudigt de interpretatie van tijdsafhankelijke ellipsometrische metingen aanzienlijk.

Silicium kan met behulp van een met SF_6 geïnjecteerd expanderend cascadeboogplasma worden geëtst met een snelheid van meer dan 1 μm/s : één à twee ordes van grootte sneller dan met de tot nu toe gangbare processen.
(J.J. Beulens, A.T.M. Wilbers, M. Haverlag, G.M.W. Kroesen, G.S. Oehrlein, D.C. Schram, opgestuurd naar *J. Vac. Sci. Techn.*).

Om de continuïteit van langlopend onderzoek te bevorderen, is het raadzaam om de werkperiodes van elkaar opvolgende aio's op hetzelfde project minstens enkele maanden te laten overlappen.

Het onderscheid tussen de beloningsstelsels van respectievelijk aio's en oio's kan leiden tot grote verschillen in de hoogte van secundaire vergoedingen : dit leidt tot ongelijkheid van het netto inkomen.

De mate van discipline die betracht wordt bij het afvoeren van gebruikt bestek, borden en soepkommen na de lunch is hoger bij natuurkundigen dan bij werktuigbouwkundigen.

Het feit dat er in de maatschappij nog vaak vreemd wordt aangekeken tegen vrouwen die na het sluiten van een huwelijk hun eigen naam willen blijven dragen, duidt erop dat de maatschappelijke status van vrouwen nog vaak afgeleid wordt van die van hun echtgenoot.